ASD-TDR-62-1034
Part I

4063310

RESEARCH AND APPLICATION ENGINEERING TO DETERMINE THE EFFECT OF PROCESSING VARIABLES ON CRACK PROPAGATION OF HIGH-STRENGTH STEELS AND TITANIUM

TECHNICAL DOCUMENTARY REPORT NO. ASD-TDR-62-1034, PART I

April 1963

406 310

Directorate of Materials and Processes
Aeronautical Systems Division
Air Force Systems Command
Wright-Patterson Air Force Base, Ohio

Projects 7351 and 7381
Tasks 735105 and 738103

B

Aeronautical Systems Division,
Directorate of Materials and
Processes, Metals and Ceramics
Laboratory, Wright-Patterson Air
Force Base, Ohio.
Report No. ASD-TDR-62-1034, Part I.
RESEARCH AND APPLICATION ENGINEERING
TO DETERMINE THE EFFECT OF PROCESSING
VARIABLES ON CRACK PROPAGATION OF
HIGH-STRENGTH STEELS AND TITANIUM.
Interim report, April 1963, 137pp.
incl. illus., tables 56 refs.
Unclassified Report

1. High-strength
   steels
2. Titanium
3. Crack
   propagation
I. AFSC Projects
   7351, 7381;
   Tasks 735105,
   738103
II. Contract
    AF 33(616)8156
III. Crucible Steel
     Co.of America
     Pittsburgh,Pa
IV. B.R.Banerjee
    J.J.Hauser

V. Aval fr OTS
VI. In ASTIA
    collection

(over)

This report describes in detail the
fine-structural characterizing of
several high-strength steels [AISI
4340, Type H-11 (Crucible 218), Type
422 stainless, work-hardened Type 301
stainless, PH15-7Mo semiaustenitic
stainless, and B-120VCA beta titanium
alloy] and gives the relationship of
these structures to smooth and notch
strength properties. The fine struc-
tures of these materials were char-
acterized and correlated with
strength and fracture properties to
an extent never before achieved.

1. High-strength
   steels
2. Titanium
3. Crack
   propagation
I. AFSC Projects
   7351, 7381;
   Tasks 735105,
   738103
II. Contract
    AF 33(616)8156
III. Crucible Steel
     Co.of America
     Pittsburgh,Pa
IV. B.R.Banerjee
    J.J.Hauser

V. Aval fr OTS
VI. In ASTIA
    collection

Aeronautical Systems Division,
Directorate of Materials and
Processes, Metals and Ceramics
Laboratory, Wright-Patterson Air
Force Base, Ohio.
Report No. ASD-TDR-62-1034, Part I.
RESEARCH AND APPLICATION ENGINEERING
TO DETERMINE THE EFFECT OF PROCESSING
VARIABLES ON CRACK PROPAGATION OF
HIGH-STRENGTH STEELS AND TITANIUM.
Interim report, April 1963, 137pp.
incl. illus., tables 56 refs.
            Unclassified Report

This report describes in detail the
fine-structural characterizing of
several high-strength steels [AISI
4340, Type H-11 (Crucible 218), Type
422 stainless, work-hardened Type 301
stainless, PH15-7Mo semiaustenitic
stainless, and B-120VCA beta titanium
alloy] and gives the relationship of
these structures to smooth and notch
strength properties. The fine struc-
tures of these materials were char-
acterized and correlated with
strength and fracture properties to
an extent never before achieved.

ABSTRACT

This report describes in detail the fine-structural charac-
terizing of several high-strength steels [AISI 4340, Type H-11
(Crucible 218), Type 422 stainless, work-hardened Type 301
stainless, PH15-7Mo semiaustenitic stainless, and B-120VCA beta
titanium alloy] and gives the relationship of these structures
to smooth and notch strength properties. The fine structures
of these materials were characterized and correlated with strength
and fracture properties to an extent never before achieved.

This technical documentary report has been reviewed and is approved.

I. PERLMUTTER
Chief, Physical Metallurgy Branch
Metals and Ceramics Laboratory
Directorate of Materials and Processes

TABLE OF CONTENTS

LIST OF TABLES

PAGE

LIST OF TABLES

PAGE

LIST OF FIGURES

LIST OF FIGURES (continued)

PAGE

I. INTRODUCTION

Metallurgical ingenuity has made available to the metals industry numerous methods and techniques for strengthening metals and alloys. For example, through solid-solution alloy strengthening and precipitation of a second phase, through dispersoid strengthening, and through structural refinement, the metallurgist has sought to gain additional strengthening in new and existing alloy systems. However, despite considerable success in devising high-strength alloys, the mystery of toughness versus brittleness remains unsolved. The only hopes of achieving radical improvements or significant breakthroughs in combining high strength with high ductility lie in further basic understanding of the atomic micromechanics of plastic deformation to fracture.

As the investigation progressed,[1-5] it became increasingly clear that in order to understand the atomic micromechanics of plastic deformation to failure in these structurally complex materials, the initial fine structures must also be understood in detail so that the deformation steps leading to failure can be explained in terms of this basic framework. Thus a two-pronged approach was developed toward structurally characterizing these materials and studying the detailed micromechanics of deformation to failure. These findings were correlated with fracture mechanical analysis of smooth and notch tensile properties.

This report describes the fine structures and strength and toughness properties of five high-strength steels and a titanium alloy. The materials included in this study were AISI 4340 (a low-alloy, high-strength steel), Type 422 stainless, Crucible 218 (a hot-work steel), extra-work-hardened Type 301 stainless, PH15-7Mo semiaustenitic steel, and B-120VCA beta titanium alloy. Each steel is individually treated in subsequent sections of this report.

II. MATERIALS

The chemical compositions of the materials structurally characterized in this program are shown in Table I. Table II gives a detailed outline of the processing used. Billets of melt-variable 4340, Type 422, and Crucible 218 were reduced to 0.120-inch-thick sheets; Type 301, PH15-7Mo, and B-120VCA were received in sheet form and were further processed by cold rolling to dimensions needed in the testing program.

1

Table I

Chemical Compositions of Materials

Material[a]	Sheet No.	C	Mn	P	S	Si	Ni	Cr	V	W	Mo	N	O	H (ppm)
4340	61-323	0.40	0.72	0.02	0.015	0.24	1.80	0.82	--	--	0.29	0.008	0.0024	0.8
4340 VAR	61-222	0.40	0.72	0.008	0.008	0.24	1.80	0.79	--	--	0.27	0.006	0.0006	0.2
4340 VIM	62-10	0.38	0.73	0.003	0.011	0.28	2.02	0.81	--	--	0.27	0.0002	0.0009	0.1
4340 VIR	61-459	0.37	0.54	0.003	0.011	0.28	1.90	0.85	--	--	0.27	0.0008	0.0009	0.3
Crucible 218	61-383	0.41	0.36	0.015	0.012	0.99	0.22	5.01	0.48	--	1.29	0.002	0.0041	0.7
Type 422	61-384	0.20	0.74	0.014	0.018	0.24	0.81	12.22	0.23	1.05	1.01	0.017	0.0072	0.4
Type 301	61-388[b]	0.10	1.34	0.030	0.014	0.48	7.15	17.7	--	--	0.26	0.016	0.0047	0.9
PH15-7Mo	61-389[c]	0.071	0.42	0.014	0.017	0.34	7.17	14.8	--	--	2.14	0.0018	0.0007	1.8
B-120VCA[d]	61-373 61-374	0.02	--	--	--	--	--	11.5	14.0	--	--	0.018	0.11	220

[a] VAR = Vacuum arc remelted.   VIM = Vacuum induction melted.   VIR = Vacuum induction remelted.

[b] Also contains 0.33% Cu.

[c] Also contains 0.09% Al, 0.08% Ti.

[d] A titanium-base alloy that also contains 3.2% Al, 0.004% B, and 0.25% Fe.

2

Table II

Processing Schedule

Material[a]	Heat No.	Quantity	Forging Temperature (°F)	Rolling Temp.[b] (°F)	Processing
4340 VAR	S7497	One sheet (28 x 66 x 0.120 in.) One sheet (28 x 52 x 0.120 in.)	--	--	--
4340 Air	114509	Two 458-lb billets (4-in. sq)	2200 (finish at 1800)	1800	400 lb roll to 0.120-in. thick
4340 VIM	022739	One 60-lb billet (4-in. sq) One 75-lb billet (3-in. sq)	2200 (finish at 1800)	1800	135 lb roll to 0.120-in. thick
4340 VIR	S98372	One 612-lb billet (4-in. sq)	2200 (finish at 1800)	1800	150 lb roll to 0.120-in. thick
Crucible 218 Air	23746	One 538-lb billet (4-in. sq)	2000 (finish at 1650)	1800	300 lb roll to 0.120-in. thick
Type 422 Air	54399	One 475-lb billet (4-in. sq)	2000 (finish at 1600)	1800	300 lb roll to 0.120-in. thick

a VAR = Vacuum arc remelted.
  Air = Air melted.
  VIM = Vacuum induction melted.
  VIR = Vacuum induction remelted.

b Reheat after each pass.

3

Table II (continued)

Processing Schedule

Material	Heat No.	Quantity	Forging Temperature (°F)	Rolling Temp. (°F)	Processing
Type 301	152183	Two sheets (1/4 hard) (36 x 120 x 0.122 in.)	--	--	A portion cold-rolled 67%
PH15-7Mo	800614	One sheet (mill-annealed at 1950 F)	--	--	A portion cold-rolled 60%
B-120VCA	R6787	One sheet (vacuum-annealed) (37 x 99 x 0.186 in.)	--	--	Cold-rolled to different extents
		One sheet (vacuum-annealed) (37 x 98 x 0.194 in.)	--	--	

4

The billets were first forged into 8 by 1-inch slabs and then hot-rolled to 0.120-inch-thick sheets about 5 feet long. They were rolled to a minimum width of 7-1/2 inches so that test specimens could be obtained from both transverse and longitudinal directions (forging and rolling temperatures are also given in Table II). Uniform quality during processing was ensured through detailed inspections involving macro- and microetching, chemistry, and hardness checks at various locations along the billet length.

III. FRACTURE TESTS

Fracture test data were obtained in terms of net fracture stress (σ_n) and fracture toughness (K_c)—either as a function of critical crack length (i.e., K_{c1}) or of percentage shear (i.e., K_{c3}). Smooth tensile data were separately obtained using sheet specimens having dimensions shown in Figure 1.

The heat-treatment schedules used are shown in Table III. The sequence of treatments had to be varied in the Type 301 and PH15-7Mo stainless steels. For AISI 4340, Crucible 218, and Type 422 materials, austenitizing treatments were in an argon atmosphere but tempering treatments were in air; austenitizing, refrigerating, and tempering were done in rapid succession with a minimum of time spent between steps. For the quench-variation treatments and the bainitizing treatments in 4340, neutral salt baths were used. Type 301 stainless specimens were cold-rolled 67% to 0.043-inch thickness, and tested in the worked and aged condition. PH15-7Mo specimens were refrigerated and aged at 0.120-inch thickness, surface ground to 0.049-inch final thickness and tested. For the cold-worked and aged condition, PH15-7Mo material was rolled to 0.049-inch thickness and aged, as shown in Table III, before testing.

All of the heat treatments for the Type 301 and PH15-7Mo steels were performed in an argon atmosphere to prevent decarburization. In the other materials, the fully heat-treated samples were finish machined by equally wet grinding both sides of the 0.120-inch blanks to 0.067-inch final thickness; the edges were also machined to precise dimensions. Thus, freedom from possible decarburized layers was ensured. The finish-machined samples were carefully inspected to check tolerances and to record dimensions.

After degreasing, the specimens were tension-tested under various conditions. A vertical tube furnace surrounded the specimen for tests above the ambient, and immersion in a liquid coolant was used for low-temperature tests; thermocouples directly recorded all test temperatures. A slow head speed (0.01 in./min) permitted careful examination of the sample during test. Although most tests were made on longitudinal sheet specimens, enough transverse specimens were used so that pertinent trends could be detected.

5

Table III

Heat-Treatment Schedule for Fracture Testing

Material and Purpose	Treatment
4340 Melt-variable materials (air, VAR, VIR, and VIM) (treated to obtain maximum yield strength).	1550 F for 1/2 hr, oil-quenched, refrigerated at -320 F, tempered at 400 F for 2 hr.
4340 Air Melt (treated to examine martensite brittleness region).	1550 F for 1/2 hr, oil-quenched, refrigerated at -320 F, tempered 350 to 800 F for 2 hr.
4340 Air Melt (quenching variations but samples tempered to same yield strength level).	(1) 1550 F for 1/2 hr, oil quenched, refrigerated at -320 F, tempered at 400 and 750 F for 2 hr. (2) 1550 F for 1/2 hr → 1000 F for 5 min, air-cooled, refrigerated at -320 F, tempered at 400 and 750 F for 2 hr. (3) 1550 F for 1/2 hr → 600 F for 30 sec, air-cooled, refrigerated at -320 F, tempered at 400 and 750 F for 2 hr.
4340 Air Melt (treated to obtain tempered bainite or tempered martensite at a common room-temperature yield strength).	(1) 1550 F for 1/2 hr → 600 F for 1 hr, water quenched, refrigerated at -320 F, tempered at 600 F for 2 hr. (2) 1550 F for 1/2 hr, oil-quenched, refrigerated at -320 F, tempered at 850 F for 2 hr. (3) 2150 F for 1/2 hr, oil-quenched, refrigerated at -320 F, tempered at 750 F for 2 hr. (4) 2150 F for 1/2 hr → 1550 F for 1/2 hr, oil-quenched, refrigerated at -320 F, tempered at 750 F for 2 hr.
Crucible 218 (treated to obtain maximum strength).	1850 F for 1/2 hr, oil-quenched, refrigerated at -320 F, tempered at 1000 F for 2 + 2 hr.
Type 422 (treated to obtain maximum strength).	1900 F for 1 hr, oil-quenched, refrigerated at -320 F, tempered at 900 F for 2 hr.
Type 301 (treated to obtain high strengths).	(1) Cold-rolled 67%. (2) Cold-rolled 67% and aged 750 F for 8 hr.
PH15-7Mo (treated to obtain high strengths).	(1) 1750 F for 10 min, air cooled, refrigerated at -100 F, aged at 950 F for 1 hr. (2) Cold-rolled 60% and aged at 1100 or 1150 F for 1 hr.

For smooth-tensile testing, samples of 2-inch gauge length and 0.35-inch width were used to obtain ultimate tensile and 0.2% yield strength.   For 4340, Crucible 218, and Type 422, specimens of 0.067-inch thickness were used; for Type 301, specimens of 0.043-inch, and for PH15-7Mo, 0.049-inch thickness were used.

For notch fracture properties, fatigue-cracked center-notched sheet-tensile specimens (Figure 2) measuring 2 by 7.5 inch were used; in this report they are referred to as notched-tensile speci-mens.* Specimen blanks were sheared from annealed sheets and machined to dimensions (Figure 2). The pinhole diameters were reamed, and the center notch was spark-discharge machined. All tensile specimens were carefully checked for precise alignment of pin centers and center notch. Fatigue cracks were introduced at the ends of the center notch by a tension-tension fatigue machine, cycled (about 18,000 cycles) to obtain a total $2a_o$† of 0.3 to 0.4 times the specimen width, W. After heat treating, as outlined above, the specimens were tension tested. In general, the fatigue-crack length, the percentage shear, and the maximum load to fracture were recorded during the test. The percentage shear was carefully determined by measuring the shear-lip width, at 2X specimen thick-ness away from the edge,[6] with a calibrated filar eyepiece on a binocular microscope. In addition, the slow-crack length was determined in many room-temperature tests by the ink stain method,[6] or by recording the progress of the slow crack on movie film.

After being tested, fracture samples were stored in evacuated desiccators for electron microscope studies of fine structure.

A.   Gross Fracture Appearance

As a result of observations on all the materials, the gross-fracture appearance of notched tensile specimens in high-strength steels may be generally classified as follows:

(a)   Single-Shear or Full-Shear Ductile Failure.—As illus-trated in Figure 3(a), this type of failure shows a single shear plane across the sheet thickness, the shear plane usually being inclined near 45 degrees to the stress axis.

(b)   Parallel Shear Lips and Transverse Fracture.—This type of failure is a combination of the single shear and transverse fracture, as shown in Figure 3(b). As the ductility decreases, the parallel shear becomes narrower until a flat transverse fracture occupies the entire specimen width, as shown in Figure 3(f).

* Notched tensile specimen: center-notched fatigue-cracked sheet-tensile specimen, prepared according to recommendations of ASTM Committee on Testing High Strength Sheet Materials.[6]

† a_o = notch depth from center line.   (See Figure 2.)

(c) Double Shear or Trough-and-Ridge Failure.—Ideally,
this type of failure would consist of two inclined
shear planes intersecting at the center of the sheet
thickness. However, because of the transverse fatigue
cracks at the specimen center, failures of the type
shown in Figure 3(c) are more commonly encountered.
The two or three steps between the fatigue crack and
the trough-and-ridge provide the geometrically
needed transition.

(d) Orthogonal Shear Lips and Stepped Transverse Fracture.—
This type of failure is intermediate between the
trough-and-ridge formation [Figure 3(c)] and the true
orthogonal shear lip fracture [Figure 3(e)]. In the
stepped fracture, the transverse fracture alternates
with shear steps in a series of steps, with orthogonal
shear lips tapering toward the sheet surfaces
[Figure 3(d)].

(e) Orthogonal Shear Lips and Flat Transverse Fracture.—
When the transverse crack acquires sufficient velocity
to propagate itself in a continuous manner, this type
of fracture [Figure 3(e)] is encountered. The orthog-
onal shear lips taper down (or up in the other half
of the specimen) to intersect the sheet surface.

(f) Flat Transverse Fracture.—This totally brittle frac-
ture appearance [Figure 3(f)] shows no macroscopic
regions of shear failure. Although on a fine-structure
scale, these flat fractures may be associated with
numerous submicroscopic shear deformation markings.

Beachem and Srawley[7] described fractures of Types (a), (b),
(c), and (e) in a high-strength sheet material (AMS 6434 steel),
and, of course, flat-transverse fractures [Type (f)] are often
observed. However, the stepped transverse fracture [Type (d)] was
discovered as a fracture form intermediate between the idealized
trough-and-ridge (c) and the orthogonal shear-lip (d) types. In
other words, if the material is ductile enough to periodically
arrest propagation of the flat transverse fracture, generating
multiple shear steps—until a new transverse fracture is initiated
at the end of the shear step—then such alternating fracture
propagation gives rise to the observed stepped-transverse fracture.
Almost any trough-and-ridge type of fracture in these notched
tensile sheet specimens exhibits at least a few steps [Figure 3(c)].

Thus ductile fractures above the full-shear transition
temperature assume either the single-shear lip (a) or the
partially stepped trough-and-ridge (c) types of fractures.
However, fractures in the transition region usually exhibit the
forms (b), (d), or (e). Below nil-ductility level, completely
brittle fractures are characterized by a flat-transverse (i)
appearance.

8

B. Irregularities in Fracture Appearance

Fracture appearance as characterized in the foregoing may not be uniquely evident in a single sample, e.g., either side of a fractured sample may exhibit differences in the gross-fracture type. In addition, edge effects, such as the edge-shearing, forming an edge lip in Figure 3(d), are often seen when the fracture path deviates substantially from the transverse direction. These can often obscure percentage-shear measurements for K_{c3} determination, as in Figure 4, when an edge-nucleated fracture gives less than 100% shear at distance = 2B from the specimen edge; but in the absence of this edge effect a 100% shear would be obtained.* Such effects must be guarded against in interpreting results of notch tests. Also, significant exceptions to this general scheme of fracture appearance are evident in materials that are heavily cold-worked to obtain the extra high strength, as in Type 301 or PH15-7Mo.

IV. MICROFRACTURE FACETS—APPEARANCE AND TOPOLOGY

To reveal the detailed topographical contours of the numerous minute fracture facets formed during deformation to failure, these irregular surfaces must be examined at higher magnifications.

Light-microscope fractography,[8] although interesting, was soon found to have inadequate resolving power and depth of field for studying the ultimate details on such surfaces. The much greater depth of field of the electron microscope, along with its higher resolving power, naturally led to electron microfractography.

Early electron metallographic studies[9] of fracture surfaces were made from pressed pure-aluminum disks that were anodized to produce a thin alumina film on the surface—replicating the fracture contours. The isolated alumina film made satisfactory replicas that reproduced the morphology of the fractured surface.

Direct evaporation of carbon onto the fracture surfaces, followed by electrolytic polishing to separate the replica from the metal surface, has been used to reveal fractographic topography.[10] A modification of the two-stage direct-metal carbon replica has also been proposed for electron-fractographic studies.[11]

A two-step metal-shadowed silica replica from a polystyrene negative replica was developed[12] for studying fractures in ship plate steels. The negative polystyrene replica was deposited from solution, a backing block cemented to it, and the composite separated by freezing in dry ice. Silica and later metal were shadowed on the negative replica, which was subsequently dissolved in organic solvents.

---

* B = specimen thickness.

A pressed plastic replica technique was used for electron microfractography,[13] and such results were recently reviewed[14] in terms of cleavage fracture. This technique used a tough cellulose-acetate film (formerly sold under the trade name Faxfilm), one surface of which was premoistened with acetone. The moist acetate film was pressed on to the fracture surface to replicate the surface contours. After stripping, shadowing, and carbon evaporation the plastic could be dissolved away, leaving a metallized carbon replica.

Some fracture surfaces in steel were etched with bromine[15] for extraction replication of precipitates from such surfaces; and fatigue-ruptured surfaces of mild steel were lightly etched to reveal grain boundaries.[16]

To directly reproduce the topography of the minute fracture facets in these high-strength steels, a two-stage replica technique was optimized for application to this program:

One side of an 0.005-inch-thick cellulose-acetate tape was softened by wetting with acetone. This acetate film was pressed on to the fracture surface and allowed to dry. The tape was then stripped from the sample and placed on a glass slide for shadowing. Uranium-rotary shadowing, followed by a carbon-film deposit, provided a satisfactory replica. This uranium-shadowed carbon replica was separated from the primary acetate replica by dissolving the acetate film in warm acetone.

Figure 5(b) illustrates the type of submicrotopography obtained by this technique. However this technique as well as the aforementioned techniques from the literature showed nothing in terms of the metallurgical fine structures although they did faithfully reproduce topological contours of the fracture surfaces.

In studying the micromechanism of flow and fracture in these high-strength steels,[1-5] the inadequacy of replicating fracture contours, without being able to correlate them directly with the fine structures of these materials, was felt to be a substantial factor in our lack of understanding of the detailed micromechanics of fracture initiation and propagation. Therefore, an intensive effort was made to develop a new replica technique that would permit visualizing not only the fracture contours—as determined by velocity effects of fracture propagation—but to relate these effects directly with the significant microstructural features such as precipitates and grain boundaries. By combining the salient features of metal-shadowed carbon surface-replica and anodic extraction-replica techniques into one replica method, an etch-shadow extraction replica is obtained which contains information relating to microstructural features and fracture propagation velocity effects. Thus a bridge between these key parameters was obtained, and this technique is being used to advantage in further clarifying the detailed micromechanics of

10

deformation, fracture initiation, and propagation in these high-strength materials.

To illustrate the effectiveness of this technique, samples of Type 422 stainless were heat-treated by quenching from 1900 F and tempering at 900 F for 2 hours. The samples were fractured by a hammer blow on a cold chisel held at a notch that had been handfiled on one surface. Samples were fractured at room temperature and at 300 F to obtain characteristic fracture morphology.

A. Etch-Shadow Extraction Replica

In etch-shadow extraction-replica method, the fracture facets were first etched for 30 seconds in Vilella's etching reagent and the surface thoroughly rinsed in alcohol and dried. Platinum metal was directly rotary shadowed at 30 degrees, and then carbon rotary evaporated at 60 degrees. This double replica film was anodically extracted from the pre-etched surface by anodic dissolution of the surface in a 1% HCl in 5% Picral solution at about 10 volts.

The micrographs in Figure 5 show details of the fracture surface in Type 422 stainless tempered at 900 F for 2 hours and fractured at 70 and 300 F. Flat fracture facets were obtained in the samples fractured at 70 F (top row), whereas parabolic facets were obtained in the samples fractured at 300 F (bottom row). Figure 5(a) shows macroscopic views of the fracture surface at 9X; Figure 5(b) shows electron micrographs of cellulose-acetate pressed replicas of the fracture surface; and Figure 5(c) shows etch-shadow extraction replicas.

The top row of micrographs shows relatively brittle, flat fracture facets. Figure 5(b), top—a pressed cellulose acetate replica—shows many surface markings, river patterns, and other disturbed regions reflecting effects of velocity changes during fracture propagation; it does not, however, reveal anything about the metallurgical fine structure. The new etch-shadow extraction replica [Figure 5(c), top], on the other hand, shows precipitated carbides, austenite boundaries, and other fine-structural details in addition to the fracture-facet morphology.

Similarly, in the bottom row of micrographs representing a more ductile fracture type, the fracture morphology is revealed by the pressed cellulose acetate replica [Figure 5(b), bottom]; however, only in the etch-shadow extraction replica [Figure 5(c), bottom] are seen the structural details affecting initiation and hindrance to propagation of these ductile parabolic fracture facets. The details of these facets are seen even better in Figure 6 at a higher magnification.

11

Figure 6(a) shows a secondary fracture, progressing along
a vertically oriented, prior-austenite grain boundary. An
example of a parabolic fracture facet nucleated by a large
residual carbide or inclusion is clearly revealed in Figure 6(b);
a secondary fracture, initiated at a grouping of precipitated
carbide particles, may also be seen.

Thus, the new etch-shadow extraction-replica technique—
combining in one replica the salient features of shadowed surface
replica and precipitate extraction replica—provides unique
information which permits correlation of fine-structural features
with fracture propagation.

B. Slow-Crack Measurement

Measuring the length of the slow crack by the ASTM-recommended
ink-stain method was unsatisfactory because of the persistent
tendency of the ink to be drawn into a portion of the fast crack
by vacuum suction. Figure 7 shows ink penetrating through a
narrow center crack and spreading to a fan tail at the extreme
edge of the tensile specimen. Because of these effects, the ink-
stain measurements are considered unreliable in giving true values
of slow-crack length at the onset of fast-crack propagation.
Recording the slow-crack growth on 16-mm movie film (at 24 frames/
sec) permits more reliable measurement of the crack length at the
onset of fast-crack propagation; in addition K_{c1} values obtained
from these movie-film measurements agreed more consistently with
the K_{c3} values from percentage-shear measurements.

Irwin et al.[17] have also successfully used movie photography
and compliance gauges in their more recent studies of fracture
mechanics. An electrical-resistance technique[18] has also been
used by others. Furthermore, at the last meeting (May 15-16,
1962) of the ASTM Committee on Fracture Testing of High Strength
Metallic Materials, "it was generally recognized that the use of
ink in sharp-notched or fatigue-cracked specimens should not be
recommended for determining slow-crack growth."[19]

Therefore, movie-film photography is being used in our
determinations of slow-crack growth. Because the literature con-
tains only scanty evidence on comparative reproducibility of the
two methods, K_c measurements by both these techniques along with
K_{c3} values from percentage-shear measurements are given in
Table IV for 4340 steel (air-melted, VIM, and VAR heats).
Table IV reports only those ink-stain crack lengths where the
staining was considered to be reliable and relatively free from
gross suction and spattering effects. The much better agreement
between K_c values by the photographic and percentage-shear
measurements, compared with ink-stain measurements, is apparent.

Table IV

Fracture Toughness of 4340 Steel Determined by Ink-Stain, Photographic, and Percentage-Shear Measurements[a]

Code[b]	Heat Treatment[c]	Fracture Toughness		
		Ink[d]	Photographic[d]	Shear[e]
	Air-Melted			
23A9-L	1550 F, oil quenched	32.0	--	31.7
23A1-L	1550 F, oil quenched	43.2	--	39.0
23C16-L	1550 F, oil quenched + 350 F	69.8	--	66.7
23D17-L	1550 F, oil quenched + 350 F	70.1	--	71.0
23D8-L	1550 F, oil quenched + 400 F	110	--	110
23D3-L	1550 F, oil quenched + 400 F	172	--	130
23F7-L	1550 F, oil quenched + 400 F	--	79.4	74.2
23G10-L	1550 F, oil quenched + 400 F	--	69.5	73.1
23K7-L	1550 F, oil quenched + 400 F	--	87.8	73.9
23J12-L	1550 F, oil quenched + 400 F	--	64.8	66.0
23G2-L	1550 F, oil quenched + 400 F	--	96.7	93.9
23H7-L	1550 F, oil quenched + 450 F	--	123	108
23F10-L	1550 F, oil quenched + 450 F	--	95.6	90.4
23G13-L	1550 F, oil quenched + 500 F	--	100	81
23H4-L	1550 F, oil quenched + 500 F	--	169	154
23F4-L	1550 F, oil quenched + 500 F	--	178	161
23K13-L	1550 F, oil quenched + 500 F	--	177	161
23J18-L	1550 F, oil quenched + 500 F	--	170	159

[a] Room-temperature tests on 2 by 7-1/2 by 0.067-inch, centrally notched, fatigue-cracked samples.

[b] L = longitudinal; T = transverse.

[c] All samples austenitized at indicated temperature for 1/2 hour, refrigerated at -320 F after oil quenching, and tempered at indicated temperature for 2 hours.

[d] Fracture toughness as a function of critical crack length, 1000 psi $\sqrt{in.}$

[e] Fracture toughness as a function of percentage shear, 1000 psi $\sqrt{in.}$

13

Table IV (Continued)

Fracture Toughness of 4340 Steel Determined by Ink-Stain, Photographic, and Percentage-Shear Measurements

Code	Heat Treatment	Fracture Toughness		
		Ink	Photographic	Shear
23G17-L	1550 F, oil quenched + 550 F	--	111	88
23F15-L	1550 F, oil quenched + 550 F	--	157	153
23J11-L	1550 F, oil quenched + 550 F	--	132	120
23G18-L	1550 F, oil quenched + 550 F	--	162	161
23G7-L	1550 F, oil quenched + 550 F	--	153	138
23H10-L	1550 F, oil quenched + 550 F	--	139	149
23K14-L	1550 F, oil quenched + 550 F	--	189	187
23L19-T	1550 F, oil quenched + 850 F	196	160	133
23K5-L	2150 F, oil quenched + 750 F	157	159	162
23K21-T	2150 F, oil quenched + 750 F	--	151	138
23K1G-L	2150 F → 1550 F, oil quenched + 750 F	111	--	119
23K10-L	2150 F → 1550 F, oil quenched + 750 F	--	146	142
23K19-T	2150 F → 1550 F, oil quenched + 750 F	118	111	106
23Al6-L	1550 F → 1000 F for 5 min → 600 F for 0.5 min, air cooled, 750 F	206	--	174
23B6-L	1550 F → 1000 F for 5 min → 600 F for 0.5 min, air cooled, 750 F	191	--	153
23C18-L	1550 F → 600 F for 0.5 min, air cooled, 750 F	196	--	156
Vacuum-Induction-Melted				
10A5-L	1550 F, oil quenched + 400 F	--	195	197
10B20-T	1550 F, oil quenched + 400 F	--	205	201
Vacuum-Arc-Remelted				
22A52-L	1550 F, oil quenched + 400 F	132	95.2	87.4
22Al7-T	1550 F, oil quenched + 400 F	87.2	75.1	61.0

14

The movie method also permits deliberate and detailed study of the progress of slow-crack growth to the onset of rapid-crack propagation because single frames can be projected on a screen. The crack appearance at the onset of rapid-crack propagation in several samples of 4340 steels are illustrated in Figure 8. Figures 8(a) and 8(b) show the slow cracks proceeding on a somewhat curved surface, surrounded by a dark region that represents the shear lips; apparently, the crack often deviates somewhat from the transverse direction. Figures 8(c), 8(d), and 8(e) show a forked appearance in the vicinity of the slow crack. This appearance is due to multiple light reflections from the sloping terraces of metal in the region of the plastically deformed zone surrounding the slow crack. Occasionally, the slow-crack length differs between one side of the center notch and the other [Figures 8(d) and 8(e)] even though the specimen dimensions and the notch geometry and dimensions are well within specified tolerances and there is no evidence of specimen misalignment in the tensile machine.

V. EXPERIMENTAL RESULTS ON AIR-MELTED 4340 STEEL

A. Mechanical Properties

In relating the microstructural aspects to flow and fracture properties, several distinctly separate variables must be considered. In quenched and tempered martensitic steels, the yield strength, tensile strength, and fracture toughness are all known to depend significantly upon the tempering parameter. Although the dependence of yield and tensile strengths on tempering temperatures is well known, the relationship of fracture toughness to fine-structural characteristics has not been established.

Therefore, both the smooth and notch tensile properties of air-melted 4340 were determined, along with detailed structural investigations, as a function of various tempering treatments. Fracture-mode transition as a function of tempering was characterized, in addition to detailed investigation of the submicrotopography, through replica-electron microscopy.

Figure 9 shows the effect of tempering at various temperatures on the smooth tensile properties, on hardness, on fracture toughness (K_{c3}), on fracture appearance, on net fracture stress (σ_n), and on fracture propagation resistance (R).*

---

* R = Fracture propagation resistance is the ratio between net fracture stress and yield strength.

15

Significantly, while the smooth-tensile properties decline with higher tempering temperatures, a fracture-mode transition is observed in the 100 to 700 F tempering range (Figure 9). However, between 400 and 550 F, a large scatter is observed in the fracture property data. This is the temperature range that has been historically associated with the so-called 500 F embrittlement phenomenon. However, a sufficient number of repeat tests in this temperature range clearly established that the scatter in the notch properties—e.g., K_c, σ_n, R, or percentage shear—is significantly increased, but no actual decrease exists in notch tension properties, in contrast to the reported results from Charpy impact data.[23] The curve of least-square averages in Figure 9 shows a smooth transition, free from a dip or discontinuity. An insufficient number of tests with this material, however, can easily lead one to the erroneous conclusion that an actual dip occurs in the curve of fracture properties versus tempering temperature. The reason for the enhanced scatter in fracture data in this temperature range may be understood in terms of the heterogeneous fine-structure data (Section V-5); the minute details of fracture topography as revealed by electron submicro-fractography, are also illustrated at various strength levels in quenched-and-tempered structures (Section V-C).

B. Properties and Fine Structures

Until a few years ago, surface-replica and extraction-replica techniques were mostly used for studying the submicroscopic struc-tures in metallic materials. However, recent interest in direct transmission of thin-foil samples has tended to single out this technique over those used in the past. The combined use of all these powerful techniques, however, has yielded a more complete and comprehensive characterizing of all the fine-structural aspects of metallic systems than can be obtained by transmission techniques alone.[20] Therefore, in this program, surface and extraction replication methods are combined with the transmission technique to fully characterize each material studied.

Surface replicas of Parlodion shadowed with uranium and extraction replicas of carbon-Parlodion were obtained from undeformed portions of the smooth tensile specimens. The surface-replica micrographs are shown at 15,000X and include several martensite laths; the extraction replicas, on the other hand, are shown at twice this magnification (30,000X) to illustrate the detailed morphology of the carbides.

Direct transmission electron microscopy was also used to characterize the detailed submicrostructures in this 4340 steel at various strength levels obtained after quenching and after subsequent tempering at 100 to 1300 F.

For microstructural examination, samples of tempered mar-
tensite structures were cut from smooth sheet tensile specimens
of the air-melted material that had been austenitized at 1550 F
for 1/2 hour, oil quenched, refrigerated in liquid nitrogen, and
tempered at 200 to 1300 F in 100-degree intervals for 2 hours each.

Thin sections of air-melted 4340 for transmission-electron
microscopy were obtained by grinding and cold rolling the annealed
material to 0.001-inch thickness. Individual samples about
5/8 by 1 inch were sealed in Vycor tubing that had been preflushed
several times with argon. Austenitizing, refrigerating, and
tempering treatments were similar to those for the smooth-sheet
tensile specimens.

1. Structures at a Tensile Strength
   of 320,000 psi

The quenched structure (at a tensile strength of 320,000 psi)
appears roughened on the surface-replica micrograph [Figure 10(a)],
but no discrete precipitate particles are visible. The trans-
mission micrograph also shows the martensite structure as having
a substantial distribution of heterogeneous strain producing strong
interference fringes; some evidence of autotempering during the
oil quench is also seen from decoration of microtwin interfaces
within the martensite laths [Figure 10(d)]. The dark inter-
martensite boundaries also suggest heavier local precipitation.

The extraction replica shows a discontinuous, unresolvable
precipitate in many martensite laths [Figure 10(b)]. This two-
dimensional precipitate—which may be partially suppressed by a
more drastic quench, e.g., by quenching into iced brine from the
austenitizing temperature—probably represents an early stage of
ε-carbide precipitation somewhat analogous to the Q-tempering
of low-carbon martensites.[21,22] Although no definite diffraction
evidence has been obtained so far, this unresolved precipitate
is believed to be ε carbide because at a somewhat higher tempering
temperature more of this material yields a distinct ε-carbide
electron-diffraction pattern.

This rapid transformation at a relatively low temperature,
combined with the similarity in spacing of the (101) planes of the
hexagonal ε carbide, and that of the (010) martensite lattice
suggests the possibility of a direct shear transformation of mar-
tensite to this transition-carbide structure.[21] Such a shear
transformation would require only small atomic movements for
limited transformation over volumes where concentration fluctu-
ations provide favorable pre-existing arrangements. The crystallo-
graphic congruence of the (101) martensite plane with the carbide
structure is even more interesting because this martensite plane
is parallel to the (111) austenite stacking-fault plane. Thus,
the postulated mechanism may suggest a shear transformation

17

to form growth-limited nuclei of ϵ carbide at favorable sites during quenching; however the formation and growth of ϵ carbide during subsequent retempering must occur by the more usual diffusion-controlled nucleation and growth mechanism.

The extraction replica of the quenched sample also shows few large, rounded particles ($\approx$500 A in diameter), which give an X-ray diffraction pattern of cubic symmetry having lattice parameters similar to those of $M_{23}C_6$. The existence of this structure has been established in more than one heat (Section VI-B), but the surprising presence of an $M_{23}C_6$-type carbide in 4340 is not yet explained.

Tempering at 100 F for 2 hours showed somewhat increased microtwin decoration by further carbide precipitation at these interfaces; heterogeneous strains persisted within the matrix, contributing to marked interference contrast effects.

Upon tempering at 200 F, some carbide particles became resolvable as individual platelets, but they were few in number and were sparsely scattered in the microstructure. Individual carbide platelets also grew to visibly resolvable entities.

Upon tempering at 300 F, the decoration of microtwins could be observed more distinctly by transmission microscopy, and some discrete carbide plates were seen. Otherwise the fine-structural changes were small.

Thus, the high tensile strength (320,000 psi) and low toughness (36,000 psi $\sqrt{\text{in.}}$) of the quenched material are altered only slightly upon tempering at temperatures up to 300 F (Figure 9) because of only minor changes in the fine structures that accompany these treatments.

2. Structures at Tensile Strengths of
    260,000 to 290,000 psi

Tempering at 400 to 500 F is not only characterized by the fracture-mode transition observed in Figure 9, but in addition all the fracture properties—fracture toughness, net fracture stress, percentage shear, and fracture propagation resistance— exhibit a much larger scatter than what is observed by tempering either above or below this range. A large number of specimens were tested at each tempering temperature in this range to establish a least-square average curve through the experimental points of Figure 9. This demonstrates a smooth, though steep, fracture-mode transition upon tempering through this range, in contrast to data previously reported in the literature.[23]

Therefore the wide scatter in the data, which characterizes this tempering range in 4340 steel, is suggested as a possible reason for observed anomalies in impact test data in the published literature.[23] Fine-structure data would tend to support this explanation.

For example, at 400 F, the surface-replica micrograph [Figure 11(a)] shows the martensite laths sharply defined because of accelerated etching at the intermartensite boundaries; this is believed to be due to accelerated carbide precipitation and growth at these preferred sites.

This is also the temperature range where the M_3C carbide first appears,and at the top of this range, almost completely replaces the ε carbide originally present. For example, Figure 11(b) shows M_3C platelets within martensite laths. This extraction replica (400 F temper) shows M_3C platelets as large as 0.15 micron in length, but the filmy ε carbide coexists along with these large platelets. Indeed, many M_3C platelets are surrounded by the filmy material, suggesting a direct in situ ε carbide to M_3C transition, as seen in both extraction replica [Figure 11(b)] and transmission [Figure 11(c)] micrographs.

The transmission micrograph [Figure 11(d)] illustrates the localized growth-inhibiting effect of microtwin interfaces. At these interfaces, precipitation seems to progress by planar extension along the interface—producing the pronounced cross-hatched pattern seen in Figure 11(d)—but little, if any, sideways growth is evident away from the interface. Significantly, this type of precipitation is found only locally, while other areas in the structure appear to have a more random nucleation and growth of the precipitate [Figure 11(c)].

The scatter in the fracture properties in Figure 9 is explained by the simultaneous existence of local regions of highly limited dislocation path length, such as the cross-hatched regions in Figure 11(d), and other regions permitting substantially greater dislocation motion as in Figure 11(c). The accelerated intermartensite-boundary precipitation and the varying extents of ε carbide and M_3C carbide in different regions of the structure [Figure 11(b)] probably further contribute to the observed scatter in the fracture properties data.

Thus, at least in 4340 steel, the so-called 500 F embrittlement may be understood as a phase-transition region associated with fine-structural heterogeneity, which produces a wide scatter in fracture-property measurements in the midst of a fracture-mode transition. Specific search was made through extraction-replica, surface-replica, and transmission-electron microscopy, but no evidence was obtained of thin ferrite networks[23] or of continuous carbide films[24] previously suggested in the literature as possible explanations of the so-called 500 F embrittlement in 4340 steel.

19

3. Structures at Tensile Strengths of
   210,000 to 250,000 psi

   Upon tempering to 600 F (tensile strength of 250,000 psi), the scatter in fracture-property data diminishes (160,000 to 190,000 psi $\sqrt{in.}$ K_c), and structurally the martensite laths begin to show relatively unroughened and smooth areas. Only a trace of ϵ carbide is detected by diffraction methods at 600 F. These more homogeneous structures result in more reproducible and less scattered notch-property data.

   This trend continues to 700 F, where spheroidal carbide particles are first observed. However, the platy carbides also continue to grow, reaching ≈0.7 micron length at 800 F, as seen in the transmission micrograph [Figure 12(d)]; extraction replicas [Figure 12(b)] fail to pick up such large particles. The dislocation networks [Figure 12(d)] become distinctly visible because of progressive relaxation of internal strains. With this strain relaxation and carbide size growth, the smooth-tensile properties have declined (≈218,000 psi tensile strength at 800 F temper), while the fracture properties approach a plateau as the net fracture stress (200,000 psi at 800 F temper) approaches the yield stress and the notch-fracture test itself becomes less meaningful.

4. Structures at Tensile Strengths of
   130,000 to 190,000 psi

   Upon tempering at 900 F and above, the steady decline in tensile and yield strengths continues, but the percentage elongation begins to increase more rapidly.

   At 900 F, the martensite platelets tend to fragment into subgrains, as seen in the transmission micrograph [Figure 13(d)] and in the slight faceting of the surface replica [Figure 13(a)]. This fragmentation of the martensite laths into distinct cells by in situ polygonization plus the coalescence of the carbides into spheroidal and disk-like shapes [Figures 13(a), 13(b), and 13(c)] account for the more rapidly increasing ductility, as suggested by the data for percentage elongation. As previously indicated, the results of notch fracture tests in this region are insensitive because of the equality of net stress and yield stress.

   At still higher temperatures, the carbides continue to agglomerate and grow, while the martensite develops a pronounced substructure, until at 1200 F the intermartensite boundaries have almost disappeared [Figures 14(c) and 14(d)]. Even at this temperature, both the rod-like and spheroidal carbide particles are of the M_3C type. Some dislocations generated at the carbide-matrix interface are seen in Figure 14(d).

These multiple reactions of precipitate growth and agglomeration and matrix recrystallization (which ultimately replace the martensite-lath structure by a more equiaxed subgrain network) produce a continued decline in tensile and yield strengths (130,000 and 120,000 psi, respectively, at 1200 F temper) while the percentage elongation continues to rise ($\approx$13% at 1200 F temper).

Thus the fine structures and notch properties of 4340 steel were related at various strength levels obtained by quench and temper treatments.

C. Submicrotopography of Air-Melted 4340 at Various Strength Levels

To characterize the micromechanics of fracture initiation and propagation in high-strength steels, detailed examination of several aspects of fracture surfaces must be correlated with the macroscopic fracture-property determinations and fracture mechanics.

To reveal the detailed submicrotopographic features of fractures in air-melted 4340 steel at various strength levels of quenched-and-tempered structures, shadowed replicas of the fracture surface were prepared by a two-stage carbon-replica technique. Submicrotopograms were obtained from the room-temperature smooth-tensile specimens. All samples were austenitized at 1550 F, refrigerated at -320 F, and tempered for 2 hours at indicated temperatures.

1. Tensile Strength of 320,000 psi

The macroscopic fracture appearance of untempered 4340 steel (320,000 psi tensile strength and 228,000 psi yield strength) showed a central region of transverse fracture, surrounded by shear lips (Figure 15). At this strength level, the submicroscopic topography (Figure 16) showed that the flat fracture in the sample center had large areas of glide-plane decohesion,[25] and cleavage-fracture facets, interspersed with numerous parabolic dimples[26,27] or domains,[28] many of which exhibited a crater or crack nucleus near the focus of the parabola. This essential heterogeneity characterizes discontinuous crack propagation in these semibrittle fractures. An interesting example of a transition from glide-plane decohesion to a cleavage fracture is illustrated in Figure 16(a), which shows a clearly demarcated difference in orientation of the two planes; the glide plane near the bottom exhibits numerous flow lines, but the cleavage plane is relatively flat and free from markings. The top left-hand corner of Figure 16(a) illustrates complex initiation of several fracture nuclei propagating in

21

different directions. The regions of extensive replica folding, such as the one near the lower left-hand corner of the photo-micrograph, outline the macroscopically visible "fibers," which give rise to the fibrous appearance of these ductile fractures; these regions are roughly 15 to 30 microns in diameter and exhibit considerable size variation.

The shear lips (Figure 15, top) were characterized by numerous parabolic dimples or domains, with flow markings within each frac-ture level [Figure 16(b)]. The markings of smaller level differences within the main fracture levels are better illustrated at a higher magnification in Figure 16(c), which also shows elongated domains and equiaxed domains in proximity of each other.

Tensile samples from the transverse sheet direction showed similar microfractographs, again with highly heterogeneous, discontinuous crack propagation. Figure 17(a) shows an extensive glide-plane decohesion with various segments of minor fracture levels having a variety of geometrical forms; several parabolic and elliptical domains may be seen within the main-shear decohesion plane. At the top is a transition to a cleavage-fracture facet. The regions of extensive replica folding, corresponding to the macroscopically visible granulation or "fiber stringers," are parallel bands, as expected, instead of the generally circular or oval forms seen in the longitudinal tensile samples. Details of one of the large decohesion planes may be seen in Figure 17(b) at a higher magnification. The shear lips on the transverse fracture sample again showed a profusion of dimples or domains, usually exhibiting a fracture nucleus at the focus, and numerous level markings within the parabolic domains themselves [Figure 17(c)].

2. Tensile Strength of 280,000 psi

The macroscopic appearance of the fracture surface of quenched-and-tempered (400 F) 4340 steel at tensile and yield strengths of 280,000 and 222,000 psi, respectively, showed a full shear fracture with double 45-degree shear planes meeting at the center of specimen thickness (longitudinal tensile specimen, Figure 15). The submicrotopography typically exhibited numerous dimples or domains, and shear-plane decohesions, as in Figure 18 (a). Also shown are the boundaries of one of the macroscopic fibers with a diameter of about 20 microns; Figure 18(b) shows a second region that reveals many shear decohesions along with some dimples.

The transverse fracture sample macroscopically showed a transverse flat-fracture region bordered by shear lips (Figure 15). The submicrotopograph correspondingly revealed a greater abundance of shear-decohesion and flat-cleavage planes than the longitudinal sample [contrast Figures 18(c) and 18(a)].

3. Tensile Strength of 190,000 psi

The macroscopic appearance of the fracture surface of quenched-and-tempered (900 F) 4340 steel at 190,000 and 180,000 psi tensile and yield strengths, respectively, showed full-shear fractures of the 45-degree plane, shear type and the double 45-degree type (longitudinal tensile specimen, Figure 15). The submicrotopographs are characterized by numerous parabolic dimples or domains [Figure 19(a)] as well as by extensively elongated domains [Figure 19(b)] with many intersections of ensiform and river markings. Figure 19(a) more clearly reveals a continuing trend, observed on the samples tempered at lower temperatures, of enhanced movement or material flow near the macroscopically visible fiber boundaries. This enhanced flow takes the form of shear decohesion or numerous dimpled fracture nuclei. The location and significance of these fiber boundaries should be more thoroughly explored for a proper understanding of fracture mechanics in these materials.

The transverse specimen showed a macroscopically flat but fibrous fracture (Figure 15), and the submicrotopograph showed extensive and numerous glide-plane decohesions along with the usual dimples or parabolic fracture paths [Figures 19(c) and 19(d)]. Figure 19(c) illustrates an excellent example of the tongues[26,27] seen on fracture planes; these are believed to be indications of secondary cracks in the fracture plane where the replica found its way into the crack, creating small laps or tongues projecting from the replica surface. Both figures exhibit regions of severe replica folding caused by the macroscopic transverse fibers.

4. Tensile Strength of 130,000 psi

Macroscopic fracture appearance of quenched-and-tempered (1200 F) 4340 steel at 130,000 and 120,000 psi tensile and yield strengths, respectively, showed full-shear, double 45-degree type of fibrous fracture (longitudinal tensile sample, Figure 15). The submicrotopograph showed a mixture of extensive glide-plane decohesion and elongated dimpled-fracture facets [Figure 20(a)]. Shear decohesion extending over entire macroscopic fibers are seen in Figure 20(b). Many fracture facets contain numerous secondary fracture initiations and intersecting secondary fracture planes.

Macroscopic examination of the transverse sample showed a shearing-off type of fibrous fracture surface (Figure 15). The submicrotopography was characterized by a preponderance of elongated fracture dimples or domains, with evidence of plastic shearing on these facets [Figure 20(c)]. Excessive replica folding along parallel lines 10 to 30 microns apart at the boundaries of the microscopically visible fibers may be seen in Figure 20(d).

23

This study of submicrotopographic features of fracture propagation must be extended to relate the various events in fracture propagation (such as change in rates of propagation—characterized by markings on the fracture facets) to the fine structure of these materials. The fracture facets themselves do not reveal obvious geometrical relationships to fine structural entities; further efforts must be directed toward developing the structural link between fracture facets and the fine structures by means of modified electron microscopic techniques.

VI.   PROCESSING VARIABLES AFFECTING 4340 STEEL

Three heat-treating variables and four melting variables were evaluated to determine their effects on structure and properties of 4340 steel.

A.   Effect of Heat-Treatment Variables

Heat-treating variables applicable to low-temperature transformation products of austenite were evaluated to determine their effects on air-melted 4340 steel. Three separate variables were evaluated: (1) austenitizing temperatures, (2) quenching variations, and (3) bainitizing treatments.

1. Austenitizing Temperatures

The effects of 1550 and 2150 F austenitizing temperatures on smooth and notch tensile properties were evaluated for samples of 4340 steel tempered to comparable yield strengths.

Upon austenitizing at 2150 F (as compared with 1550 F austenitizing)the following structural differences were observed in the quenched matrix: prior-austenite grain size was much coarser (Figure 21); the $M_{23}C_6$ residual carbide present in the 1550 F austenitized material was dissolved; and retained austenite was slightly increased (by about 1%). The much coarser austenite grain size (52.9 microns in diameter at 2150 F austenitizing) required a lower tempering temperature to produce room-temperature yield strength equivalent to that of the 1550 F austenitizing (8.0 micron diameter at 1550 F austenitizing).

Figures 22(a) and 22(b) compare the smooth and notch-tensile properties resulting from the two austenitizing treatments. Despite the excess carbon dissolved in the matrix, due to dissolution of the $M_{23}C_6$ residual carbides, the effect of grain size was dominant in producing equivalent room-temperature yield strengths by tempering to 750 F for the 2150 F treatment and to

24

850 F for the 1550 F treatment. Both the larger grain size and excess carbon in solution combined to produce a higher transition temperature and lower fracture properties in the 2150 F austenitizing treatment.

To separate the pure austenite-grain-size effect from the effects of austenitizing temperature, step-quench treatments were used. Upon step quenching the 2150 F austenitized material (by holding at 1550 F for 1/2 hour), no significant differences were produced in smooth and notch-tensile test data [compare Figures 22(b) and 22(c)]. Structurally, the $M_{23}C_6$ carbide did not reprecipitate in the austenite upon holding at 1550 F for 1/2 hour. Therefore, this behavior suggests an insensitivity of notch properties to different states of quenched-in thermal fluctuations in the austenite, upon holding the austenite at 1550 F after prior austenitizing at 2150 F.

2. Quenching Variations

The effects of step-quenching treatments were evaluated by introducing thermal arrests at 1000 and 600 F during quenching from 1550 F. Short-time holding in the bay region (a region important in austforming treatments) was found to have no significant effect on smooth and notch tensile properties (Table V). However, upon a short isothermal hold, just above the M_S, i.e., at 600 F, the change in cooling rate through the martensite range was great enough that autotempering raised the tensile and yield strengths slightly and lowered the notch properties, σ_n and K_c. Also, it will be recalled from Table IV that a double step-quench at 1000 F plus 600 F, produced no significant difference from the 600 F step-quenching effect (Table V).

3. Bainitizing Treatments

The fracture properties of lower bainitic structures, as compared with those of tempered martensites, have been a matter of some controversy.[29,30] Therefore 4340 steel samples were isothermally transformed to 100% lower bainite at 600 F (just above the M_S temperature), quenched and refrigerated to -320 F, and retempered at 600 F for 2 hours. The retained austenite in the water-quenched bainitic structure was ≈0% as measured by quantitative X-ray diffraction method.[31] Quenched and refrigerated martensitic structures were tempered at 850 F for 2 hours to obtain similar yield strengths at room temperature. Fracture properties of these tempered martensitic and bainitic structures were evaluated at the same yield strength, and the data are given in Figure 23.

Figure 23 shows that the room-temperature yield strength of bainite (tempered at 600 F) is equal to the room-temperature yield strength of martensite (tempered at 850 F). Thus, in samples tempered at the same temperature, the yield strength

Table V

Effect of Quenching Variations in Air-Melted 4340 Steel[a]

Quenching Treatment	Specimen Code	Tempering Temp. (°F)	Tensile Strength (1000 psi)	0.2% Yield Strength (1000 psi)	Net Fracture Stress (1000 psi)	Shear (%)	Fracture Toughness[c] (1000 psi $\sqrt{In.}$)	Net Fracture Stress / Yield Strength
1550 F, 1/2 hr, oil quenched	--b	400	284	222	91.7	72.4	86.4	0.41
	--b	750	228	211	177	100	200	0.84
1550 F, 1/2 hr → 1000 F, 5 min, oil quenched	23A4	750	229	214	172	100	196	0.80
	23A15	750	229	214	169	100	186	0.79
1550 F, 1/2 hr → 600 F, 0.5 min, air cooled	23B18	400	280	236	59	30	54.0	0.27
	23D12	400	280	236	59	45	48.5	0.23
	23C18	750	237	220	145	100	156	0.66
	23A2	750	237	220	151	100	162	0.68

a Material was air melted, center notched (2 by 7-1/2 by 0.067 in.), fatigue cracked, and heat treated; all specimens were of longitudinal type; test temperature was 70 F.

b Average values reported (Section VII-B).

c As a function of percentage shear.

of bainite is inferred to be lower than the yield strength of martensite. This result agrees with previous data in the literature.[29]

The transition temperature of the tempered bainite is around 0 F, but that of the tempered martensite is ≈-100 F. At -320 F, the fracture toughness (K_{c3}) is ≈21,000 psi $\sqrt{in}$. for the tempered bainite and ≈39,000 psi $\sqrt{in}$. for the tempered martensite. The corresponding net fracture strengths are shown in Figure 23. Thus the tempered martensite in 4340 is seen to be tougher in terms of sheet notch toughness than tempered bainite at a comparable yield strength. This result agrees with reduction c. area values reported in the literature for some constructional steels.[29] These data also illustrate the need to compare toughness of different metallographic structures at the same strength level; otherwise, erroneous conclusions may be easily drawn.

B. Effect of Melting Variables

In addition to heat-treating variables, melting is a major process variable in making high-strength steels. To determine the effect of melting variables on fracture properties of high-strength steels and to correlate the properties with basic differences in either initial fine structures or in variations in fine structures during stressing to failure, different melting methods were used to obtain four heats of 4340 steel. Electric-furnace air-melted 4340, was thus compared with vacuum-arc-remelted (VAR), vacuum-induction-melted (VIM), and vacuum-induction-remelted (VIR) products. All sheet compositions were within 0.03% variation of carbon level and within 0.006% variation in nitrogen level. Besides the significant interstitials, all other elements were held as constant as possible.

The air-melted (electric furnace) and vacuum-melted heats were processed to 0.120-inch-thick sheet, and the chemical analyses are given in Table I. Carbon and nitrogen were somewhat lower and nickel and silicon were somewhat higher in the VIR and VIM materials than in the air-melted and VAR heats.

1. Grain Size and Inclusions

Intercept grain size (Table VI) was determined for the air-melted, VAR, VIM, and VIR sheets of 4340 steel (etched in a solution containing picric acid and zephiran chloride). The air-melted material had the smallest prior-austenite grain size (15.8), and the VIR material had the coarsest grain size (7.2). The prior-austenite grain boundaries were readily etched in the air-melted materials, somewhat more difficult to etch in the VIR and VIM materials, and extremely difficult to etch in the VAR material.

ASTM inclusion ratings (Table VI) showed the VIR and VIM steels to be very clean; the VAR material appeared to be somewhat cleaner than the air-melted steel. Micrographs representing typical inclusion content are shown in Figure 24.

Table VI

Grain Size and ASTM Inclusion Ratings
of Melt-Variable 4340

| Material | Type A | | Type B | | Type C | | Type D | | Intercept Grain Size |
	Thin	Heavy	Thin	Heavy	Thin	Heavy	Thin	Heavy	
Air Melted	1.4	1.1	2.2	1.3	0	0	1.7	1.5	15.8
VAR	0.2	0.5	1.1	1.3	0	0	2.1	1.5	12.0
VIM	1.0	0	1.0	0	0	0	2.0	1.0	9.4
VIR	0	0	1.0	0	0	0	1.0	1.0	7.2

2. Heat Treatment

For easy machining of tensile blanks, the 0.120-inch-thick sheets were annealed by furnace cooling from 1500 F.

To compare smooth and notch tensile properties of the melt-variable 4340 steels, tempering for 2 hours at 400 F was selected because this treatment gave the maximum yield strength where the fracture toughness parameter would depend most critically on processing variables.

3. Retained Austenite

Retained austenite was measured by the X-ray integrated line intensity method.[31] About 3% retained austenite was present in all of the melt-variable 4340 steels after austenitizing at 1550 F, oil quenching, and refrigerating in liquid nitrogen; most of this austenite was transformed upon tempering at 500 F or higher. Ice-brine quenching from the austenitizing temperature plus refrigerating at -320 F reduced the austenite content to about 2%.

4. Carbide Types

An $M_{23}C_6$ type of cubic carbide was found in all of the melt-variable 4340 materials in the austenitized (1550 F) and quenched condition. The presence of such a carbide would undoubtedly play a role in affecting hardenability and strength properties of the alloy. However, previous investigators had not found this cubic carbide in low-chromium alloy steels.[32] Alstetter[33] reported $M_{23}C_6$ in modified 43XX compositions containing 1.5 to 3.0% silicon; however, a suggestion of silicon interaction was implied[33] in the formation of stable $M_{23}C_6$. This new finding of $M_{23}C_6$ in commercial 4340 compositions containing 0.24 to 0.28% silicon clearly shows that high silicon is not necessary to stabilize $M_{23}C_6$ in 4340 compositions.

To characterize the nature of precipitate structures in 4340 steel tempered to various strength levels, X-ray diffraction analyses were made of anodically extracted residues. Samples, 5/8 by 2 by 1/10 inch, were heat-treated in exactly the same way as the tensile test pieces, and carbides were extracted electrolytically in a solution of ammonium chloride and citric acid at a current density of 250 ma/in^2.

Only two carbides were found by X-ray diffraction: (1) a small amount of $M_{23}C_6$ residual carbide and (2) precipitated M_3C carbides in samples tempered at 400 F and higher. The residual $M_{23}C_6$ could be dissolved in the steel by austenitizing at 2100 F.

Electron diffraction of selected areas of extraction replicas, obtained from quenched-and-tempered specimens showed ε carbide[21,34-36] and M_3C to be present. These electron diffraction data are summarized in Table VII. No Bragg diffraction could be obtained from the extraction replica of the oil-quenched sample. Epsilon carbide was detected at 300 to 600 F. Electron diffraction from the sample tempered at 300 F exhibited two broad diffraction halos, which were relatable to the ε-carbide structure.

M_3C was first found after tempering at 400 F and at all higher tempering temperatures. Further work must be done to define more clearly the conditions of ε carbide to M_3C transition, which seems to be associated with a fracture-mode transition. Faster quenching rates to surpress autotempering during quenching from the austenitizing treatments and other variables must also be investigated.

5. Fracture Properties

Smooth-sheet-tensile properties and notch properties of the air-melted, VAR, VIM, and VIR materials are represented in Figures 25 and 26 as a function of test temperatures (from -200 F to +300 F); all the steels were quenched and tempered to maximum

Table VII

Carbides Detected in Air-Melted 4340 Steel
by Electron Diffraction
of Extraction Replicas

Condition	Carbide Detected
Quenched	None
300 F Temper	Early ϵ Carbide
400 F Temper	ϵ Carbide + Weak M_3C
500 F Temper	M_3C + Weak ϵ Carbide
600 F Temper	M_3C + Trace ϵ Carbide
800 F Temper	M_3C

strength levels (400 F temper for 2 hours). The notch properties are expressed in terms of net fracture stress, fracture appearance transition, fracture toughness, and crack propagation resistance.

In terms of maximum observed net fracture strength, the VIM material showed values up to 200,000 psi, with the VIR materials following closely behind at about 190,000 psi; the VAR and air-melted materials, however, showed maximum net-fracture stresses of around 110,000 psi. In terms of transition temperatures (using the criterion of fracture appearance transition temperature), the VIM and VIR material exhibited transition at below -100 F, but the VAR and air-melted materials had transitions at or just below room temperature (72 F).

Similarly, in terms of maximum observed fracture toughness, K_{c3} (calculated from percentage shear values), the air-melted and VAR materials have average values of around 110,000 psi $\sqrt{in.}$, whereas the VIM and VIR have average maximum K_{c3} values of over 200,000 psi $\sqrt{in.}$

Again, in terms of the ratio of the net fracture stress to the yield stress, $R = \sigma_n/\sigma_y$ (which is a measure of the crack propagation resistance),[37] the air-melted and VAR materials show average maximum values of around 0.5, whereas the VIM and VIR materials have average maxima of around 0.8 to 0.9. Thus when Srawley's[37] empirical R_{min} requirement of 0.7 for roll-formed and welded construction is used, the VIM and VIR meet the required crack-propagation-resistance criterion, but the air-melted and VAR steels do not.

Despite their coarse austenite grain size, the VIM and VIR materials had higher σ_n, higher toughness K_{c3}, higher R, and lower transition temperature than the air-melted and VAR stocks. Although the VIM and VIR materials had somewhat lower smooth tensile and yield strengths, the observed difference in σ_n and R appear too large to be explained solely on the basis of these differences in smooth tensile properties. The greater cleanliness and chemical compositions (e.g., lower carbon and nitrogen and higher nickel and silicon levels, see Table I) of the VIM and VIR would tend to favor greater toughness but fine-structure studies may shed further light on this subject. The greater toughness of the VIM and VIR materials relative to the air-melted 4340 is readily understood. However the poor properties in VAR material must be related to its higher inclusion content and to possible segregation effects. The fracture appearance of air-melted, VAR, and VIR notched samples (Figure 27) not only illustrates the relative brittleness of the air-melted and VAR materials, but the streaked fracture surface of the VAR specimen strongly suggests a directional structure effect, unusual in longitudinal samples.

The substantial difference in fracture properties as a function of processing variables is also significant, and suggests the need for specifying materials processing in the reporting of fracture properties in the literature. Much of the data in the literature lacks complete materials processing history, and thus has only limited usefulness for direct comparisons.

VII. TYPE 422 STAINLESS STEEL

A detailed characterizing of the fine structures and results of fracture testing at a variety of temperatures are given for Type 422 stainless steel.

A. Material Inspection

Inspection of the billet showed the material to be clean, sound, and free from visible internal defects; chemistry appeared to be normal throughout the billet. The chemical analyses and the sheet processing data are given in Tables I and II.

ASTM inclusion ratings for the material are given in Table VIII A typical microstructure at 100X (Figure 28) shows many particles of well-dispersed oxides.

Table VIII

ASTM Inclusion Ratings of Type 422 Stainless Steel

Type A		Type B		Type C		Type D	
Thin	Heavy	Thin	Heavy	Thin	Heavy	Thin	Heavy
1.3	1.0	2.8	2.3	0	0	4.2	2.0

B. Heat Treatment

The 0.120-inch-thick hot-rolled sheets were annealed by slow cooling from 1600 to 1300 F, holding at 1300 F for several hours, and furnace cooling to room temperature.

A microstructural examination showed 1900 F to be the highest austenitizing temperature at which no delta ferrite formed. Samples were therefore austenitized at 1900 F in argon for 1 hour, oil quenched, immediately refrigerated in liquid nitrogen for at least 15 minutes, and finally tempered at appropriate temperatures for 2 hours. The austenitic grain size determined by the intercept method was 4.0.

A 900 F tempering temperature was used to evaluate fracture toughness because it produces maximum yield and tensile strengths, thus making the fracture properties most sensitive to structural factors. For actual engineering applications, however, a better compromise between strength and toughness would be advisable.

The M_S temperature of this material was determined by using a direct-plotting dilatometer. The expansion and contraction of a 4-inch-long sample was transformed into an electrical signal through a linear-differential transformer, the output of which was plotted on the y axis of an x-y recorder; the x axis plotted temperature as sensed by a thermocouple spot-welded to the sample. The M_S temperature of this steel was 475 F after austenitizing at 1900 F.

C. Retained Austenite

After being oil quenched, Type 422 stainless steel contained 1 to 3% retained austenite. This retained austenite was quite stable, and was not appreciably lowered when the material was refrigerated in liquid nitrogen; in fact, a tempering temperature above 1000 F was required to decompose the austenite. Such a small amount of austenite would not however contribute appreciably to secondary hardening in this steel.

D. Carbides and Analyses

To identify the carbide structures in Type 422 steel, electrolytically extracted residues were analyzed by X-ray diffraction, and extraction replicas were analyzed by electron diffraction. Austenitizing this steel at 1900 F does not dissolve all of the $M_{23}C_6$ carbide; in fact, upon subsequent tempering two precipitated carbides appear: M_3C and $M_{23}C_6$. The relative intensity of electron diffraction lines from these precipitated carbides (rated as weak, medium, and strong) is shown in Figure 29 as a function of tempering temperature. The M_3C carbide was first detected by electron diffraction after 400 F tempering. The carbide diffraction pattern became more distinct, and persisted upon tempering at 500 through 900 F. Upon tempering above 900 F, the M_3C pattern became weaker, and was replaced by the alloy carbide $M_{23}C_6$ (the decrease in intensity of the M_3C pattern suggests a re-solution of this carbide). The $M_{23}C_6$ diffraction became stronger and sharper above 1000 F.

The weight percentage of extracted residues obtained from quenched-and-tempered samples are also given in Figure 29. The weight percentages were determined by anodically dissolving samples in a 1% HCl-alcohol solution and collecting and weighing the residues. The quenched sample contained about 0.2% residue, consisting mostly of residual $M_{23}C_6$, which remained undissolved during austenitizing. Upon tempering to about 500 F, the residue increases to about 0.7 to 0.9 weight percent. This would account for only a small portion of carbon in the steel; thus, most of the carbon in the steel (0.2%) must be still dissolved in the martensite in this tempering region. When $M_{23}C_6$ precipitates above 900 F, however, more carbon enters the carbide, and the weight-percent residue curve rises rapidly to about 3 to 4%.

E. Electron Probe Microanalysis of Carbides

Some of the anodic residues were compacted into 1/4-inch-diameter pellets by using a hydraulic press at 8000 psi. These pellets were used for electron probe X-ray microanalysis. Several areas, approximately 1/2 mm square, on each sample were analyzed for alloy content by the electron probe; a comparison was made with calibrated standard samples.

In Table IX, a summary is given (in terms of metal atom percent) of the findings obtained on these pellets for tempering conditions at which the M_3C carbide dissolves and the $M_{23}C_6$ carbide precipitates in its place. Some of these data are also plotted in Figure 29.

33

Table IX

Effect of Tempering Temperature on Alloy
Content of Anodic Residues

Tempering Temperature (°F)	Fe	Cr	Mo	V	W
900	86.0	13.7	0	0.3	0
1000	77.4	21.8	0	0.8	0
1100	19.1	74.2	2.7	3.9	0.1
1200	22.4	71.9	1.9	2.7	1.1

These preliminary microprobe data are extremely interesting in revealing the metal-atom concentration changes as a function of tempering. No detailed mechanistic conclusions will be drawn from these data until further confirming experiments are made to check the values. However, the promise of the method is clearly indicated in the trends of carbide-composition changes suggested by these data.

F. Properties and Fine Structure

Smooth tensile properties and fine structures of Type 422 were examined and correlated by varying the tempering treatments to produce tensile strengths from 260,000 to 150,000 psi.

Smooth tensile and hardness data are given in Figure 30 as a function of tempering treatment. Tensile and yield strengths exhibit minima of around 230,000 and 160,000 psi, respectively, at about 500 to 600 F. The yield strength shows a pronounced maximum at 900 F, after which both yield and tensile strengths tend to decline. Hardness data seem to parallel the tensile properties. Elongation increases with tempering temperature to about 700 F, then decreases to about 1000 F—suggesting temper embrittlement— and subsequently increases.

For evaluating fracture-mode transition in this material and relating the significant factors in fine structure and fracture propagation, a 900 F tempering temperature was used. Because this temperature produces maximum yield and tensile strengths, the fracture properties are most sensitive to structural factors, even though a better compromise between strength and toughness would be desirable for engineering application or design purposes.

G. Electron Metallography

The fine structure of quenched-and-tempered Type 422 was explored by direct-transmission electron microscopy, by extraction replica, and by surface replica methods. Again, magnifications were adjusted to show general areas and to reveal specific aspects of the structural details. Thin sections were obtained from annealed material ground and cold-rolled to 0.001-inch thickness; individual samples to be heat-treated were sealed in Vycor tubing that had been preflushed with argon.

Figures 31 to 39 show details of fine structure of Type 422 at various strength levels obtained by quenching from 1900 F and tempering at 300 to 1300 F at 100-degree intervals. These data will be correlated with fracture mechanical information in the detailed investigation of deformation processes leading to fracture at a variety of test temperatures.

1. As-Quenched and 300 F Tempered Structures

The as-quenched structure (260,000 psi tensile strength), as seen by surface replication (Figure 31), has a relatively smooth surface with some grooving of the prior-austenite boundaries. The individual martensite laths, however, are not clearly delineated. The austenite-boundary grooving is explained in terms of the accelerated carbide precipitation in these regions (as seen in the extraction-replica micrograph). The identity of this filmy carbide is yet uncertain because efforts to detect ϵ carbide or M_3C in this structure have been unsuccessful.

In the transmission micrographs, a heterogeneously strained martensitic matrix is seen with some carbide precipitation at the boundaries and dislocations. In the higher magnification transmission micrograph, parallel microtwin striations are clearly seen with a minimum spacing of about 150 A. Interestingly enough, a network of dislocations, or a substructure, appears to be forming within the microtwins themselves. Furthermore, the transmission micrograph at high magnification provides a clear example of a needle-like martensite lath and internal microtwinning which were previously considered[38] to be mutually exclusive phenomena.

The structure of the 200 F tempered material showed no significant changes as compared with the quenched structure.

Upon tempering to 300 F, where the strength level (260,000 psi tensile) remains substantially unchanged, the fine structures remain similar. The surface replica micrograph of the 300 F

tempered structure is similar to that of the quenched structure except for a more definite delineation of the martensite needles, a somewhat greater surface roughening, and more pronounced etching of the prior-austenite boundaries. The extraction replica also suggests only somewhat increased breadth of the filmy carbide precipitate along the prior-austenite boundaries, but the carbide morphology still prevents detection by diffraction techniques, as in the quenched sample.

Consistent with recent theories[39] of the martensite-transformation mechanics, heterogeneous and macroscopic strains are still observed. These strains result from the trains of heterogeneous shears, following transformation along an interface of parallel screw dislocations. The high-magnification transmission micrograph shows numerous masses of dislocation tangles within the martensite laths themselves.

The low-magnification transmission micrograph also reveals a row of thin, small, dark-etching needles within a broad martensite lath. These are reminescent of the frozen-in martensite embryos seen in samples of Type 410 stainless steel.[20] A special effort must be made to determine the precise nature of this structural manifestation and its possible role in the subsequent transformation and deformation characteristics of this alloy.

2. 400 F Tempered Structure

Tempering at 400 F results in no significant change in tensile strength, but the surface replicas of the 400 F tempered structure (Figure 32) show pronounced delineation of martensite laths, a general surface roughening, and further accelerated etching of the prior-austenite boundaries. The extraction replica suggests continuous-general precipitation of a fine carbide, which was identified by electron diffraction as M_3C carbide—insufficiently extensive in the third dimension to give good Bragg reflections.

The transmission micrographs show coherent lamellar carbide plates in a Widmanstaetten configuration as well as dislocation tangles. In addition, microtwins within martensite laths are clearly seen. Tangles of dislocation networks are tending to form a substructure that is visible within individual martensite laths (see circle).

3. 500 F Tempered Structure

Tempering at 500 F produces a significant drop in tensile and yield strengths (Figure 30). The replica and transmission micrographs of the 500 F tempered structure (Figure 33) suggest the growth of the M_3C carbide to a maximum length, reaching micron dimensions. The significant coarsening of the M_3C precipitate is

36

clearly evident in the extraction replica. Thus, the observed
dip in the tempering curve (Figure 30) at 500 F may be understood
in terms of the pronounced growth in carbide-precipitate size
(Figure 33). The surface replica also shows a general smoothening
of the matrix, and this is further confirmed by the reappearance
of blank, precipitate-free areas in the extraction replica. The
transmission micrographs show dislocation tangles around precipitate
particles.

4.   600, 700, and 800 F
     Tempered Structures

     Although basically similar structures are seen after 500
and 600 F tempering, the M_3C precipitate at 600 F appears to be
somewhat shorter, and the precipitate plate edges appear to be
more jagged. In addition, the matrix appears to be slightly more
roughened, and the transmission micrographs suggest a fine new
precipitate at dislocation nodes and intermartensite boundaries.

     At 700 and 800 F (Figures 34 and 35) the trends above be-
come more pronounced, indicating a gradual dissolution of the
M_3C carbide and its replacement by a new precipitation of $M_{23}C_6$
in a very fine form. This $M_{23}C_6$ precipitation, though not yet
detected by diffraction techniques, undoubtedly contributes to
the secondary hardening effect observed (Figure 30) upon tempering
at these temperatures.

5.   900 and 1000 F Tempered Structures

     At 900 F tempering (Figure 36) the martensite matrix is
further roughened, as seen in the surface replica, and this effect
is further pronounced at 1000 F (Figure 37) where the first
visible signs of a fine, general precipitation is observed.
Diffraction will also detect the alloy carbide $M_{23}C_6$ at 1000 F.
However, examining the transmission micrographs from these tempering
treatments and comparing them with those from the 600 to 800 F
tempering regions provide an explanation for the observed hardening
and strengthening (Figure 30). The alloy-carbide precipitation
is apparently growth inhibited, resulting in an extremely fine
precipitation that is unresolved even in the transmission micro-
graphs at 1000 F. However, the entire sequence of transmission
micrographs illustrates an increasing concentration of pinned
dislocations and dislocation networks, which would clearly increase
the flow stress and tensile strength properties. The dislocation
concentrations seen at 900 and 1000 F, at the higher magnifications,
clearly illustrate this behavior—which may be described as a pinned-
dislocation strengthening mechanism that probably accounts for the
delayed softening or temper resistance of Type 422.

37

6. 1100, 1200, and 1300 F
   Tempered Structures

   At 1100 F (Figure 38), a significant smoothening of the martensite matrix in the surface replica clearly suggests growth of the $M_{23}C_6$ carbide; this is further confirmed by the extraction replica. The transmission micrograph (Figure 38) shows the previously observed pinned dislocation networks (at 900 and 1000 F) rearranged into tangled networks and cellular structures. Also seen are alloy-carbide precipitate particles.

   At 1200 and 1300 F, the fragmentation into cell structures continues, followed by a decrease in strength properties. At 1300 F (Figure 39) a discernible increase is noted in cell size. Growth of carbides is also seen in the surface and extraction replicas.

H. Fracture Testing

   Smooth and notch tensile testing of Type 422 stainless steel quenched and tempered to maximum strength levels was performed at various temperatures, both above and below ambient, in order to characterize tough-to-brittle transition. The heat treatment used consisted of austenitizing at 1900 F for 1 hour, oil quenching, refrigerating at -320 F, and tempering at 900 F for 2 hours. A 900 F tempering was used to evaluate fracture toughness because this treatment produces a maximum in yield and tensile strengths so that the fracture properties would be most sensitive to structural factors.

   The results, which are shown in Figure 40, illustrate a transition behavior in the 250 to 100 F region. At 250 F and above, the crack propagation resistance criterion ($R = \sigma_n/\sigma_y$) has a value of 1 or greater. In the 250 to 100 F region, R drops to 0.3, i.e., a change in σ_n from 180,000 psi to about 60,000 psi occurs. The K_{c3} values follow a close parallel. Thus, at room temperature, at 180,000 psi yield strength, the numerical value of σ_n and K_{c3} for this material is about 50,000. The fracture appearance of the notch and smooth bar test specimens (Figures 41 and 42) confirm these observations.

   Fine-structure studies, submicrofractography, and other details of the micromechanics to failure must be further studied in relation to fracture properties.

38

VIII.   CRUCIBLE 218 HOT-WORK STEEL

The fine structures of Crucible 218 were characterized for various strength levels of quenched-and-tempered conditions. Such characterizing of fine structures in relation to mechanical properties is a fundamental prerequisite to understanding the deformation mode and fracture behavior of these materials.

To evaluate fracture toughness and fracture-mode transition characteristics and to determine their dependence on structural factors, tempering to 1000 F was selected because at the maximum tensile strength level (upon 900 to 950 F tempering) the transition temperature range would be so high as to be significantly affected by further tempering during testing.

A.   Material Inspection

The processing and chemical analysis of Crucible 218 are given in Tables I and II. Billet inspection showed some carbon variation from the midsection to the surface and the billet end; a cross section at the billet end showed carbon content variation from 0.37% at the center to 0.39% at the edge. A midsection analysis showed the carbon content to be 0.42% both at the center and at the surface. However, this variation lies within the nominal composition range for air-melted stock.

Numerous inclusions were observed in this material, and a representative area of the material is shown at 100X in Figure 43. The ASTM inclusion ratings are given in Table X. The austenite grain size determined by the intercept method was 10.8.

Table X

ASTM Inclusion Ratings of Crucible 218
Hot-Work Steel

Type A		Type B		Type C		Type D	
Thin	Heavy	Thin	Heavy	Thin	Heavy	Thin	Heavy
0.9	0.9	1.0	0.9	0	0	2.8	1.9

B. Heat-Treatment and Sample Preparation

Hot-rolled sheets, 0.120 inch thick, were annealed at 1650 F for easy machining of tensile specimens. All samples were austenitized at 1850 F in argon for 1/2 hour, oil quenched, and immediately refrigerated in liquid nitrogen for at least 15 minutes. Tensile specimens were tempered in air for 2 + 2 hours at various tempering temperatures. Samples used for transmission-electron microscopy were tempered in a predessicated argon atmosphere.

For transmission electron microscopy, thin sections were prepared by grinding and cold rolling the annealed material to 0.001-inch thickness. The heat-treated specimens were then electrolytically thinned in a chromic-acetic acid solution.

The M_s temperature of this steel (after austenitizing at 1850 F) was 510 F, as determined by a direct-plotting dilatometer. Knowledge of this temperature was required to properly evaluate micrographs of quenched samples.

C. Retained Austenite

Retained austenite measurements by X-ray diffraction showed that samples oil-quenched from the austenitizing temperature contained about 3% austenite, and that refrigeration in liquid nitrogen reduced this to about 2%. Tempering below 900 F for 2 + 2 hours did not change the amount of retained austenite; but tempering above 900 F reduced the retained austenite to about 1%, and tempering for 2 + 2 hours at 1000 F transformed all of the remaining austenite.

D. Carbides

Small quenched-and-tempered samples were anodically dissolved in an ammonium chloride-citric acid electrolyte fo· X-ray and chemical analyses of the undissolved residues. The amounts of residue extracted from Crucible 218 after quenching and tempering for 2 + 2 hours at various temperatures are giv·n in Figure 44. Each plotted point represents the average of ·t least two extractions; the deviation from the arithmetic ean was less than 10% in every case. Chemical analyses—by electron microprobe analysis on extracted residues compressed int) pellet—are also shown in Figure 44 in the tempering regi)n where alloy carbide replaces M_3C.

The residual carbides in the austenitized and quenched material were found by X-ray diffraction analysis to be MC and M_7C_3. The precipitated carbides in this complex steel were identified by electron diffraction of particles supported on extraction replicas. Combined X-ray and electron diffraction data suggest that much of the vanadium in the steel is in the residual MC carbide and that this carbide does not further precipitate on tempering up to 1200 F. At a tempering temperature of around 400 F, ϵ carbide in very fine form and some platelets of M_3C were detected; the ϵ carbide persists to about 600 F, but traces of M_3C persisted up to 1100 F. The electron diffraction patterns show that one or more alloy carbides precipitate when samples are tempered above 900 F; when the samples are overaged at 1100 F, diffraction shows the presence of M_2C as well as M_7C_3. By tempering at 1200 F, some of the M_2C transforms into M_6C while some of the M_7C_3 transforms into $M_{23}C_6$.

E. Strength and Structure Correlations

The various strength levels attained in tempered martensitic structures of Crucible 218 were related in detail to the fine-structural changes in this material.

1. Mechanical Properties

Tensile properties for Crucible 218 are given in Figure 45. The tensile properties for quenched specimens are not shown because premature failure made it impossible to obtain a yield strength value. These brittle specimens failed at stresses between 131,000 and 183,000 psi; fracture was initiated at surface flaws.

Upon tempering quenched martensite at various temperatures—to about 800 F—the tensile strength (Figure 45) decreases, but then reverses in direction to give a maximum at around 950 F before decreasing rapidly; the minimum in tensile strength at about 800 F may reflect temper brittleness in this material. Yield strength changes slightly upon tempering between 300 and 950 F and then rapidly decreases above 950 F; elongation remains substantially unchanged up to about 950 F and then increases.

The literature[40] records maximum tensile and yield strengths of Vascojet 1000 upon austenitizing at 1850 F for 1/2 hour and tempering at 1000 F for 1 + 1 + 1 hours; however for H-11 compositions[41] with variable carbon contents (0.23 to 0.43%), yield strengths showed maxima after similar heat treatments, but the tensile strength did not reveal any pronounced peak. No maximum in either tensile or yield strength was observed[42]

in H-11 type steels. These differences have not yet been explained.

Hardness changes (Figure 45) show a drop at around 300 F, and a secondary hardening at 900 F. All of these property changes were related to observed fine structural changes in this material.

2. Fine Structures in Quenched-and-
    Tempered Crucible 218

Samples of Crucible 218 at various strength levels—produced by quenching and by tempering for 2 hours at 200 to 1200 F—were examined by surface replica, extraction replica, and thin-section direct-transmission electron microscopy. The fine structures that appear after various heat treatments are illustrated in Figures 46 through 53, which show Parlodion-surface replicas shadowed with uranium metal, carbon-Parlodion extraction replicas, and thin-section transmission electron micrographs.

The surface-replica micrographs, at a low magnification (15,000X), reveal the etched topographical contours on represent-ative large areas. The extraction replicas, at 30,000X, establish the morphology of precipitates. On the other hand, the trans-mission micrographs at 30,000X and 60,000X illustrate specific aspects of fine-structural details, including the nature and distribution of dislocations, microtwinning, and other internal structural characteristics. Such complete fine-structural characterization is essential to a proper understanding of the detailed mechanism of flow and fracture in this complex material.

a. Quenched and 200 and 300 F
    Tempered Structures

The surface-replica micrograph of the as-quenched structure (Figure 46) shows several large (up to ≈0.2 micron diameter) particles in a martensitic matrix; these particles are residual carbides and possibly some inclusions. The martensite laths vary considerably in size, and frequently some of then have a roughened surface reminescent of an unresolvable fine precipitate. Although some martensite laths show significant surface roughening, others were characteristically free from etching attack, suggesting a pronounced heterogeneity in the extent of fine precipitation within individual laths. Also some of the prior-austenite boundaries were quite heavily attacked, such as the two boundaries emerging from a triple point near the center of the micrograph.

42

The extraction replica (Figure 46) shows a considerable amount of fine filmy precipitate and possibly a few precipitate particles, which are not resolvable even in this electron micrograph at 30,000X. The replica suggests that the filmy precipitate may have been in almost continuous sheets that were torn apart during replica preparation. The filmy material frequently envelopes larger (up to ≈0.2 micron diameter) rounded particles of residual carbides or inclusions. The exact nature and precipitation kinetics of these filmy precipitates must be characterized by electron diffraction.

The transmission electron micrographs (Figure 46) show a variety of internal structures within the martensite laths. Individual martensite laths substantially differ in contrast because of orientation, dislocation concentration, and precipitation differences. Numerous instances of fine precipitate nucleation at intermartensite boundaries may be seen in the thin section at 30,000X; an example of an active dislocation source at an intermartensite boundary is seen at 60,000X. These transmission micrographs do not reveal any resolvable precipitate within the martensite matrix, but rather suggest an etching effect due to compositional heterogeneity or an actual filmy precipitate. In transmission at 60,000X (Figure 46) a fine structure is observed within a martensite needle, in the form of fine parallel lines lying along the martensite-lath length. The interlinear spacing is about 100 to 700 A. These lines may represent a form of internal microtwin, or they may be dislocation lines decorated by an extremely fine precipitate. In some regions, a cell structure within the linear striations is suggested; the average cell diameter is about 250 A (see circle).

Surface-replica micrographs from samples tempered to 200 F were not much different from those of the quenched structures. Extraction replicas also showed marked similarity in the form of thin filmy precipitates. Transmission micrographs suggested some increased precipitation at intermartensite boundaries, upon dislocation lines and loops, and possibly some internal microtwin interfaces; but the actual precipitate size was still too small to be clearly resolved.

Surface-replica micrograph of structures tempered at 300 F showed substantially increased etch surface roughening (covering almost every martensite lath throughout the structure) in marked contrast to the selective etch roughening of a few martensite laths in the as-quenched and in the 200 F tempered microstructures. In addition, the intermartensite and prior-austenite boundaries were attacked more uniformly throughout. Transmission micrographs showed precipitation upon boundaries, dislocations, and internal microtwins not much different from that found in the 200 F tempered material.

b. 400 F Tempered Structure

In contrast to the 300 F tempered structure, the martensite-surface roughening appears to become more localized after a 400 F temper (Figure 47). In other words, the martensite laths in some regions show less roughening than others. Also, deep-etched martensite boundaries characterize the surface-replica micrographs after a 400 F temper, suggesting accelerated boundary precipitation; also a few platelets of carbide particles are seen within the martensite laths. This heterogeneous precipitation (which causes the localized martensite roughening) may be responsible for the observed drop in hardness upon tempering to this temperature.

In addition to the filmy precipitate, the extraction replica (Figure 47) shows platelets of a clearly resolvable precipitate. These precipitate platelets exhibit ragged edges and irregular protrusions, due to the envelope of the thin filmy precipitate around them. This appearance may suggest an in situ transformation of one carbide type to another; however, this point needs to be checked further. The micrograph also illustrates an austenite boundary with filmy precipitate and platelets. The filmy precipitate is continuous along the boundary, but the platelets are distinctly discontinuous.

In the transmission micrographs (Figure 47), discrete particulate and platy segments of precipitate are seen for the first time in this tempering series. Pronounced precipitation in parallel bands about 700 A apart are illustrated in one region (top left of transmission micrograph at 30,000X); these are precipitates upon the microtwin interfaces.

The aggregate changes in microstructure are still small, and the consequent changes in properties are also slight.

c. 500 F Tempered Structure

There was no appreciable change in microstructure between 400 F and 500 F tempering, as seen by surface-replica electron microscopy (Figures 47 and 48), except perhaps for a slight further increase in the regions of unroughened martensite surface. These slight structural changes are accompanied by only small losses in tensile and yield strengths on tempering to 500 F.

The extraction replica (Figure 48) for the 500 F tempered sample shows a mixture of the filmy precipitate and platelets and resolvable particles. The extraction replica further shows that the platelets have grown in thickness, but remained almost unchanged in length.

44

The transmission micrographs (Figure 48) reveal more internal structures in the form of irregular dislocations and dislocation loops. The thin section at 30,000X is a good example of two martensite plates probably meeting at the common unrotated (111) plane and exhibiting a typical midrib appearance. The accidental presence of a third lath, intruding between the top ends of the two otherwise adjacent martensite laths, has helped to delineate the exact nature of the midrib. The orientations of the two adjacent laths, probably having adjacent habit planes such as $(225)_\gamma$ and $(259)_\gamma$, $(529)_\gamma$ and $(259)_\gamma$, or $(225)_\gamma$ and $(529)_\gamma$ produce the observed difference in microtwin directions.[38]

Transmission microscopy also shows that the precipitate platelet spacing within martensite laths is similar (100 to 700 A) to the spacing between microtwins in the quenched structure (Figure 46).

d. 700 and 800 F Tempered Structures

With tempering at 700 to 800 F, the tensile and yield strengths decline to a minimum. The M_3C carbide agglomeration and growth and the accelerated boundary precipitation continue.

At 800 F, an almost continuous etching attack is suggested in the surface replica (Figure 49), and the precipitate morphology is seen in the extraction replica (Figure 49); the boundary filmy precipitate has a superimposed discontinuous-platy precipitate. The martensite matrix contains platy and spheroidal carbides and remnants of filmy carbide.

Transmission microscopy (800 F tempered) (Figure 49) shows regions of heavy precipitation and dislocation-precipitate interactions and also uncluttered areas. The high dislocation density, irregular pileups, and nucleation of alloy carbide on dislocation nodes are seen.

e. 900 F Tempered Structure

Upon tempering to 900 F, the tensile strength change is reversed in direction, and begins to increase correspondingly.

The surface replica micrograph (Figure 50) of the 900 F tempered structure suggests a finer precipitate size than was seen at 800 F (Figure 49), and the extraction replica tends to support this observation because of many more small particles in addition to the previously observed platy precipitates. These observations suggest a new precipitation of perhaps an alloy carbide at these temperatures. Diffraction data mark

45

900 F as the point at which the intensity of M_3C carbide begins to decrease, for M_2C and M_7C_3 are observed above 900 F. In addition, carbide analyses of extracted residues show increase in alloy content of carbides above 900 F. An interesting example of a set of three platelets precipitated upon microtwin interfaces (330 A spacing) may be seen in the lower right-hand corner of the extraction-replica micrograph.

A fine general precipitation, accelerated at intermartensite boundaries, is also suggested in the transmission micrograph (Figure 50) at 30,000X. At 60,000X, preferred nucleation of fine precipitates at dislocation nodes and lines is clearly seen; some of the previously observed large platy precipitates may also be seen in this micrograph. The observed increase in tensile strength (Figure 45) of 280,000 psi at 800 F to almost 300,000 psi at 900 F tempering is related to this precipitation strengthening although the insensitivity of the yield strength to this structural change is not yet explained.

> f. 1000 F Tempered Structure

The surface replica micrograph (Figure 51) of the 1000 F tempered structure shows a considerably greater amount of general fine precipitation but a reduced amount of the coarse, platy precipitates. The extraction replica confirms this observed trend to dissolving of the previously observed coarse, platy precipitates accompanied by increased fine precipitation.

The transmission micrograph at 30,000X (Figure 51) shows almost complete absence of the coarse, platy precipitates, but a high density of fine precipitates and dislocations. At a higher magnification (60,000X), the transmission micrograph shows a unique development of numerous dislocation interactions producing threefold nodes suggesting $\langle 100 \rangle$ dislocations resulting from $1/2$ a $[111] + 1/2$ a $[\bar{1}\bar{1}1] \longrightarrow$ a $[001]$ dislocation reactions.[43] Because of the complete absence of any recognizable parallel dislocations, the interacting dislocations may well be lying on noncrystallographic planes. These dislocation interactions are presumably induced by coherent straining of the lattice by the progressing fine precipitation.

This high density of dislocation interactions, dislocation loops, and precipitate-dislocation interactions must produce substantial slip interference due to forest interactions to give rise to the continued maintenance of high yield strength at this temperature. Diffraction data (Figure 44) suggest precipitation of several alloy carbides, and this conclusion is supported by the carbide composition changes.

46

g.   1100 F Tempered Structure

The most noticeable feature of the surface-replica micro-
graph of the 1100 F tempered structure (Figure 52) is a clear
delineation of the prior-austenite boundaries; this marked
delineation is probably related to two events: (1)   accelerated
precipitation at the prior austenite boundaries, which increases
the etching rate of these regions, and (2)   loss of intermartensite
boundaries through fragmentation and recrystallization in situ[44-46]
of the martensite laths themselves.

The extraction replica (Figure 52) also illustrates precipitate
growth.   Comparing this figure with the corresponding replica
from the 1000 F temper shows that the background has become
free of the thin filmy material, but the spheroidal precipitates
have increased in both size and number.   Previously observed
platelets have also decreased in number and in size.

The most significant event revealed by the transmission-
electron micrograph at 60,000X is the recrystallization in situ
or polygonization, which eventually replaces the martensite
boundaries.   The polygonized substructure consists of the usual
dislocation networks, forming walls or boundaries of the substruc-
ture.   Also, the subgrains themselves contain few dislocations
and transmit more electrons than nonrecrystallized areas.

The diameter of the substructure cell varies considerably
from several microns down to 0.1 micron.   The substructure size,
in the lower limit, is smaller than that reported in the
literature from microbeam measurements.[47]   In addition, a 2-micron
cell size was found in pure iron by electron transmission methods.[48]

The rapid decline in strength properties (Figure 45) upon
tempering at these temperatures is attributed to a combination
of (1)   the removal of the internal dislocation-forest structure
by recrystallization in situ, (2)   the elimination of martensite
boundaries, and (3)   the rapid depletion of carbon from the
martensite lattice.

h.   1200 F Tempered Structure

The chief feature of all the micrographs (Figure 53) from
the 1200 F tempered structure is further agglomeration and
substantial increase in precipitated carbide size.   Most of the
carbides are spheroidal or angular, but roughly equiaxed.   The
transmission micrographs show, in addition, almost complete
fragmentation of the martensite laths into subgrain elements.
The carbide particles are so large that many of them fall out of
the thin foil during specimen preparation for transmission,
leaving angular holes to mark areas originally occupied by these
large carbides (Figure 53).

F. Fracture Testing

The smooth and notch tensile properties, determined over a range of temperatures, are given in Figure 54. Testing was confined to temperatures above the ambient because the transition behavior, in terms of fracture toughness (K_{c3}) net fracture stress (σ_n), crack propagation resistance (R), or fracture appearance, was in the 100 to 200 F region. The fracture strength properties were lower for the transverse sheet direction, compared with the longitudinal direction. Correspondingly, the transition range of the transverse sheet direction seems to extend to higher temperature levels. At room temperature, K_{c3} and σ_n are about 50,000 at a yield strength of around 220,000 psi.[49,50] These values are somewhat lower than some data in the literature, but these variations are probably due to differences in their processing history, which was not specified. The crack propagation resistance, $R = \sigma_n/\sigma_y$, is about 0.25 at room temperature, and increases to about 0.7 at 200 F.

The fracture appearance of smooth and notch-tensile samples (in both longitudinal and transverse sheet directions) are shown in Figures 55 and 56 for ambient and 300 F test temperatures.

In the smooth samples (Figure 55), a flat fracture is observed for the transverse sheet direction even at 300 F, but in the longitudinal direction, a ductile, shear fracture is noted at 300 F, and a flat, brittle fracture with orthogonal shear lips is found at room temperature. However, at room temperature the notched specimens, in both the longitudinal and transverse directions, fractured in a flat, brittle failure (Fig.56). All of this information supports the fracture property data exhibiting considerable brittleness near ambient temperatures.

Studies of the fine structures, in terms of submicro-fractography, transmission electron microscopy, and other techniques, must be continued to provide further understanding of the deformation processes leading to failure in this medium-alloy hot-work steel for high-strength applications.

IX. TYPE 301 STAINLESS STEEL

Type 301 stainless steel is austenitic at room temperature, but it transforms to martensite upon cold working. The combined effects of heavy deformation plus simultaneous martensitic transformation produce marked strengthening of this material.

For this investigation, a Type 301 stainless steel was cold-rolled 67% and subsequently aged to produce various combinations of high strength and toughness. Tensile and notch-strength properties were evaluated, and structural studies undertaken.

48

A. Material Inspection

Type 301 having the composition given in Table I was received in sheet form and further processed as indicated in Table II.

The ASTM inclusion rating of the material (Table XI), as well as the micrograph in Figure 57, shows it to be relatively clean.

Table XI

ASTM Inclusion Ratings of Type 301 Stainless Steel

Type A		Type B		Type C		Type D	
Thin	Heavy	Thin	Heavy	Thin	Heavy	Thin	Heavy
0	0	2.0	1.0	0	0	5.0	2.0

B. Sample Preparation

Sheets of 1/4-hard Type 301 stainless steel were cold reduced by further cold rolling to obtain a total reduction of 67% in thickness. In addition, some samples were given various 8-hour aging treatments so that structure and properties could be studied.

C. Mechanical Properties

Figure 58 shows change in hardness as a function of aging temperatures—after 67% reduction by cold rolling. Upon aging for 8 hours at each temperature, the hardness slowly rises to a maximum (R_C 53.4) at 750 F; above 850 F, the hardness rapidly decreases.

Table XII shows tensile strength and yield strength data for Type 301 as-work-hardened and as-work-hardened and aged. For the unaged samples, room-temperature yield strength (249,000 psi) and tensile strength (264,000 psi) increase to 300,000 psi and 325,000 psi, respectively, at -320 F. Corresponding values for transverse strengths are consistently higher. The effect of aging is to increase both tensile and yield strengths by about 20,000 psi over most of the test temperature range.

49

Table XII

Tensile Properties of 0.043-Inch-Thick Sheets of Type 301 Stainless Steel

Test Temperature ($^\circ$F)	Type	Cold-Rolled 67%		Cold-Rolled 67% + 750 F for 8 hr	
		Tensile Strength (1000 psi)	0.2% Yield Strength (1000 psi)	Tensile Strength (1000 psi)	0.2% Yield Strength (1000 psi)
-320	Long	325	300	336	297
-32C	Trans	369	335	376	356
-200	Long	288	263	310	282
-200	Trans	325	303	346	325
-100	Long	271	261	296	276
-100	Trans	307	286	333	311
+ 76	Long	264	249	280	268
+ 76	Trans	288	264	315	299

Room-temperature notch-strength properties for Type 301 in the extra-work-hardened and aged conditions are given in Table XIII. Desirable properties are indicated by longitudinal K_{c3} values of about 135,000 psi $\sqrt{\text{in.}}$ in the 67%-cold-rolled condition and about 170,000 psi $\sqrt{\text{in.}}$ in the tempered condition; however, the values for transverse notch toughness are only about $K_{c3} = 60,000$ psi $\sqrt{\text{in.}}$ for the cold-rolled condition and $K_{c3} = 55,000$ psi $\sqrt{\text{in.}}$ for the aged condition, but they agree well with the values obtained by other workers.[40]

Table XIII

Room-Temperature Notch Toughness for 0.043-Inch-Thick Sheets of Type 301 Stainless Steel

Type	Cold-Rolled 67%			Cold-Rolled 67% + 750 F for 8 hr		
	σ_n (1000 psi)	K_{c3} (1000 psi$\sqrt{\text{in.}}$)	σ_n/σ_y	σ_n (1000 psi)	K_{c3} (1000 psi$\sqrt{\text{in.}}$)	σ_n/σ_y
Longitudinal	145	134	0.58	178	166	0.66
Longitudinal	151	140	0.61	188	177	0.70
Transverse	78.4	63.0	0.30	68.3	54.8	0.24
Transverse	74.2	59.7	0.28	68.5	55.1	0.24

D. Temperature Rise during Spark Notching

The notches in the test specimens of Type 301 were machined by an electrical discharge method. Because this material owes its high strength to stored cold-worked energy, any increases in temperature effected by machining had to be determined. Thermocouples were therefore spot-welded to the affected areas prior to machining, and a temperature increase of only about 10 deg F was noted. As a further check, the microstructure near the notch of a quenched martensitic sample was examined by electron metallography and found to be quite similar to an area away from the notch. These experiments clearly established that aging is not a serious problem during spark notching of cold-rolled samples.

E. Microstructures

Samples for transmission electron microscopy were cold reduced a total of 93% by first grinding the 0.12-inch-thick strips to about 0.019 inch and then cold rolling them to about 0.001 inch. These samples, measuring 1-1/4 by 5/8 by 0.001 inch, were sealed in argon-filled vycor tubes and heat treated. One sample was annealed at 1950 F for 1 hour, and another was examined in the as-rolled condition. Transmission electron micrographs of these samples are shown in Figure 59.

The transmission micrograph [Figure 59(a)] of the annealed sample shows an annealing twin with characteristic interference fringes at the twin boundaries. The matrix shows only a few dislocations; a slip trace within the twin band shows some dislocation groups. Dislocations are also seen at the twin boundaries.

In the micrograph of an annealed specimen that was accidentally deformed during preparation [Figure 59(b)], the slip traces zigzag across a twin band, as is typical, but they contain some dislocation pileups. Although the slightly strained foil had holed through at several points during preparation, no holes appear at dislocation pileups near twin interfaces as suggested by Nutting.[51] In fact, the only hole is in the center of the micrograph near a group of dislocations. A more precise investigation must be undertaken to determine the exact nature of this phenomenon, which may be significant from the stress corrosion viewpoint.

The cold-rolled sample (93% reduction in thickness) was found by X-ray diffraction to consist mostly of a body-centered α structure, with 4 to 8% remaining austenite.

The as-rolled fine structure [Figure 59(c)] reveals a lamellar flow pattern characteristic of heavily deformed metals. The individual bands, which consist of both martensite boundaries and deformation band walls, are about 0.1 micron wide. However,

51

closer examination reveals a distinct tendency for the formation
of a cellular substructure that varies considerably in size from
several microns down to 0.1 micron. Where the cell structure is
better developed, the dislocation concentration within the cell
is reduced, as expected.

The microstructures after cold reducing 67% are shown in
Figure 60 at 250X under the light microscope and at 7500X under
the electron microscope.

Sheet cross sections in the rolling direction show the usual
deformation banding in the light micrograph, but the surface-
replica electron micrographs show the individual martensite laths
to be wavy and considerably deformed. In the transverse direction,
the cross section (light micrographs) shows somewhat thicker
deformation bands, but in the electron micrographs the martensite
laths are difficult to distinguish from the deformation banding.

Figures 61 and 62 show a set of surface-replica electron
micrographs of Type 301 stainless after cold rolling and cold
cold rolling and aging for 8 hours at 650, 750, 850, 950, and
1050 F. The cold-rolled structure again shows severe wavy banding
where the individual martensite laths are frequently indistinguish-
able from the deformation bands.

After aging at 650 F (Figure 61), the deformed martensitic
matrix in some regions fragments and develops an irregular sub-
structure that completely obliterates the original martensite
appearance.

After aging at 750 F, some directional surface roughening
is observed throughout the matrix. This condition suggests an
incipient precipitation within the structure; however, the banded
microstructure still persists.

At 850 F aging, the precipitation-induced surface roughening
is replaced by resolvable precipitate particles (Figure 62). The
loss of the banded structure is also apparent.

After aging at 950 and 1050 F, the precipitate becomes more
clearly resolved and even less of the martensitic morphology
remains (Figure 62).

Extraction replica micrographs did not reveal the initial
stages of the fine precipitation up to 750 F aging. This is
probably related to the difficulty of extraction replicating
an incipient precipitation effect from such a severely distorted
structure. However, at 850 F aging, a fine precipitate was
clearly seen which progressively increased in amount and in
particle size at 950 and 1050 F aging (Figure 63). Significant
characteristics of this carbide precipitate are its continued
resistance to growth and agglomeration up to 1050 F as well as
the preservation of its directionality of dispersion due to slip-
plane nucleation.

At 850 F aging, electron diffraction showed the precipitate to be mainly M_2X plus a possible trace of M_7C_3 and $M_{23}C_6$. At 950 and 1050 F, only $M_{23}C_6$ was detected.

Thus, heavily worked and shear-transformed Type 301 stainless steel offers wide possibilities in studying the combined effects of deformation and transformation upon the sequence of structural changes and consequently upon properties.

X. PH15-7Mo STAINLESS STEEL

The semiaustenitic stainless steels such as PH15-7Mo can be heat-treated through a combination of several steps; the main purpose of these steps is to control the transformation to martensite. Thermal and thermomechanical treatments were selected so that maximum strength would be produced in this alloy system. Furthermore, aging conditions were carefully preselected so as to produce similar room-temperature strength levels either by direct thermal or thermomechanical treatments.

The metallurgical characteristics and fine-structure features produced in PH15-7Mo with these schemes were related to strength and fracture properties. However, further detailed study of fine structure and fracture properties is needed for a comprehensive understanding of the mechanical deformation characteristics of this complex alloy system.

A. Material Inspection

Polished samples of PH15-7Mo showed a substantial concentration of what appears to be titanium carbonitride particles (Figure 64). Chemical analysis of the steel, Table I, showed that 0.08% titanium was present.

Electron probe X-ray microanalysis showed these particles to be high in titanium content but low in iron. Figure 65 shows this titanium enrichment in the particles as revealed by X-ray scanning images.[52] In a scanning microanalyzer, an accelerated electron beam of 0.2 to 1.0-micron diameter is focused on the specimen surface and then scanned over the surface. As the probe scans the surface, the X-rays generated at every point are preselected by a crystal spectrometer to obtain the intensity of a given wavelength, e.g., λ corresponding to $TiK\alpha$. By modulating the brightness of a cathode-ray tube with the signal from the X-ray spectrometer, the two-dimensional distribution of a single element over the sample surface may be recorded (Figure 65).

B. Heat Treatments

For sheet-tensile property evaluations, two heat treatments were used:

(1) Refrigerated and Aged Condition.—The mill-annealed material is conditioned by holding at 1750 F for 10 minutes and air cooling. To further promote austenite to martensite transformation, the samples are refrigerated within 1 hour to -100 F, held under refrigeration for 8 hours, and air-warmed to room temperature. The final step is an aging treatment at 950 F for 1 hour.

(2) Work-Transformed and Aged Condition.—In this treatment, the sheets were first cold-rolled to 60% reduction in thickness; then they were aged at a temperature to produce the same strength level as in Treatment (1).

These two treatments were designed to produce the same strength level to provide some understanding of structural relationship to properties in these semiaustenitic precipitation-hardening stainless steels.

C. Preliminary Microstructures

To characterize the effects of austenite conditioning, transformation, and precipitation steps, samples of PH15-7Mo were heat-treated to condition and transform the austenite and subsequently aged at 450 to 1150 F.

The mill-annealed material contained substantial amounts of delta ferrite, which persists through the 1750 F conditioning and transformation. Delta-ferrite stringers are clearly seen in Figure 66 which illustrates the structure after 1750 F conditioning, transformation, and aging for 1 hour at 1150 F.

During the conditioning treatment at 1750 F, carbides precipitate out of the austenite, mainly at the ferrite-austenite boundaries; this lowers the carbon level of the austenite, and raises the M_S temperature to above room temperature. By automatic-recording dilatometry, the M_S temperature of this material (conditioned at 1750 F for 10 minutes) was found to be 175 F.

D. Carbide Analyses

Aged samples were anodically dissolved in an electrolyte of 1% HCl in alcohol. The anodic residues were weighed and analyzed by X-ray diffraction (Table XIV).

Table XIV

Carbide Analyses of Heat-Treated
PH15-7Mo Stainless Steel

Treatment	Residue[a] (Wt. %)	Carbide Type
1750 F for 10 min, air cool	--	--
+(-100 F for 8 hr)	1.1	$M_{23}C_6$
+ 750 F for 1 hr	0.9	$M_{23}C_6$
+ 850 F for 1 hr	1.0	$M_{23}C_6$
+ 950 F for 1 hr	1.0	$M_{23}C_6$
+1050 F for 1 hr	1.6	$M_{23}C_6$
+1150 F for 1 hr	1.7	$M_{23}C_6$

a
　　Each value represents the average of at least
　　two independent extractions; maximum deviation
　　was less than 10% of the average.

Only a single type of carbide, $M_{23}C_6$, was detected with or without the aging treatment. The weight percent of residue showed no significant increase upon aging at temperatures up to 950 F. At 1050 F the residue amount increased. More detailed study of carbide-precipitation kinetics is needed for proper understanding of the fine structures and their relationship to strength properties in this alloy system.

E.   Retained Austenite

Quantitative measurements of retained austenite by an X-ray diffraction method showed significant austenite retention when this alloy is cooled to room temperature after the conditioning treatment (Table XV).

Refrigerating to -100 F reduced the retained-austenite content to 3%. Upon aging at 950 F, a possible slight increase in austenite[53] was observed although this result must be rechecked before concluding that the A_1 temperature is lowered this far. At 1150 F, however, austenite unquestionably increases up to 16% upon 1-hour aging.

Table XV

Retained Austenite in Heat-Treated PH15-7Mo Stainless Steel

Treatment	Retained Austenite (Vol. %)
1750 F for 10 min, air cool	17
+(-100 F for 8 hr)	3
+ 750 F for 1 hr	2
+ 850 F for 1 hr	2
+ 950 F for 1 hr	5
+1050 F for 1 hr	3
+1150 F for 1 hr	16

F. Mechanical Properties

Tables XVI and XVII give smooth and notch tensile strength properties of PH15-7Mo steel in the refrigerated and aged condition and in the cold-worked and aged condition. The heat-treating conditions were preselected to produce comparable room-temperature strength levels through these two heat-treatment paths. The strength-increase rate as a function of lower test temperature is higher for the cold-work treatment. At any given test temperature, the cold work and aging treatment seems to raise the yield strength to the tensile-strength vicinity. However, the room-temperature notch toughness, K_{c3}, of the longitudinal cold-worked and aged material (222,000 to 233,000 psi $\sqrt{in.}$) is much higher than that of the refrigerated and aged material (51,000 psi $\sqrt{in.}$). In the transverse direction, cold rolling plus aging improves the notch toughness to some extent (e.g., K_{c3} of 95,000 psi $\sqrt{in.}$ as compared with 59,000 psi $\sqrt{in.}$ in the refrigerated-aged condition), but the total improvement is not nearly as effective as in the longitudinal case. For the observed yield strength levels ($\approx$220,000 psi), the room temperature notch toughness values of the refrigerated and aged material ($\approx$50,000 to 60,000 psi $\sqrt{in.}$) are relatively low, compared with most of the other high-strength materials studied in this program.

Figure 67 shows changes in hardness after cold-work transformed material and refrigeration-transformed material are aged at various temperatures for a constant time (1 hour). Most of the incremental hardening achieved through work-hardening transformation tends to persist even after substantial overaging at 1050 F; the work-hardened material retains a major part of this hardness differential throughout the aging sequence although the difference decreases somewhat as the aging progresses.

Table XVI

Longitudinal Tensile Properties of 0.049-Inch-Thick Sheets of PH15-7Mo Stainless Steel

Test Temperature (°F)	Refrigerated and Aged		Cold-Rolled 60% + 1100 F for 1 hr	
	Tensile Strength (1000 psi)	0.2% Yield Strength (1000 psi)	Tensile Strength (1000 psi)	0.2% Yield Strength (1000 psi)
-320	-	-	297	293
-200	261	250	273	270
-100	251	233	-	-
+ 76	230	213	234	231
+200	220	200	229	226

Maxima in hardness are achieved upon aging at 900 to 950 F for 1 hour; Rockwell "C" 54.2 was obtained with cold-work transformation, and Rockwell "C" 46.2 was obtained with refrigeration transformation.

Table XVII

Room-Temperature Notch Toughness of 0.049-Inch-Thick Sheets of PH15-7Mo Stainless Steel

Type[a]	Refrigerated and Aged at 950 F for 1 hr			Cold-Rolled 60% and Aged		
	σ_n (1000 psi)	K_{c3} (1000 psi$\sqrt{in.}$)	σ_n/σ_{ys}	σ_n (1000 psi)	K_{c3} (1000 psi$\sqrt{in.}$)	σ_n/σ_y
Longitudinal	57.7	51.2	0.27	200	222	0.86
Longitudinal	57.6	51.5	0.27	206	223	0.88
Transverse	66.1	58.9	0.31	95.6	95.6	0.43
Transverse	-	-	-	94.7	94.7	0.41

a
  Longitudinal specimens aged at 1100 F for 1 hour; transverse specimens aged at 1150 F for 1 hour.

G. Fine-Structure Study

The fine structure of this material in the high-strength condition, achieved through refrigeration plus aging, is shown in Figure 68.

The surface replica micrograph shows smooth martensite plates, which appear to be free of any precipitates in the matrix.

The extraction replica, however, reveals the stringers of $M_{23}C_6$ precipitate particles (identified by selected-area electron diffraction) at the structural boundary regions; the morphology and size of the precipitate suggests that these precipitates originated in the 1750 F conditioning treatment. These precipitates are also found in as-quenched (i.e., unaged) samples. However, aside from these coarse precipitate stringers, the matrix shows little if any precipitate.

In the transmission micrograph at 25,000X (Figure 68), a fine network of cellular precipitate outlines some substructure network. This fine precipitate probably strengthens the material in the aging treatment. Further characterization of the fine structures in this alloy system is needed for better correlation of properties with the fine-scale metallurgical changes in this complex alloy system.

XI. B-120VCA TITANIUM ALLOY

Sheet material of B-120VCA titanium alloy was processed for fine structure and property determinations. The first transmission electron microscopy of this alloy revealed some new elements of structure that may be of substantial significance. The platy Widmanstaetten α precipitate shows fine internal markings across the widths, which suggest internal twinning. The α-β interface seems to be the center of active dislocation sources. These fine structural features, as well as the persistent ghost boundaries in the annealed structure, must be carefully related to deformation and fracture phenomenon in this alloy, which has the highest strength-to-weight ratio.

A. Material Processing

The processing and chemical analysis of B-120VCA are given in Tables I and II. Mill-annealed sheets of this material were received; however, a considerable portion of these sheets had to be further cold-rolled (some 60%) prior to further processing.

B. Heat Treatment

Small samples, approximately 5/8 by 5/8 by 5/32 inch, were annealed at 1400 F for 15 minutes in an argon atmosphere. The samples were subsequently aged in argon at 900 and 600 F for various periods of time up to 72 hours.

C. Hardness

Table XVIII shows that hardness slightly increases only after 72 hours at 600 F, but it increases significantly after 40 hours at 900 F.

Table XVIII

Hardnesses of Aged B-120VCA Titanium Alloy

Aging Treatment		Hardness (R$_c$)
Temperature (°F)	Time (hr)	
600	1	30.9
	8	30.8
	40	30.9
	72	31.2
900	1	30.8
	8	31.2
	40	39.5
	72	42.4

D. Microstructures

Samples for thin-section transmission electron microscopy were ground to about 0.010 inch thick and cold-rolled to about 0.001 inch. Two samples from this thin sheet were annealed at 1400 F for 15 minutes, and one of these annealed samples was aged for 72 hours at 900 F. The two samples were electrolytically thinned for direct transmission microscopy. Although replica micrographs[54] and a transmission micrograph of an α-titanium alloy[55] have been published, no transmission work on β-titanium alloy (B-120VCA) has been heretofore published.

The annealed sample [Figure 69(a)] consists of β grains with no precipitates. A growing grain boundary held back by a large inclusion particle showed the boundary curving inward at the particle. A small residual oxide film on the sample surface presumably produces the Moiré fringes[56] seen prominently in the lower grain, but to lesser extent over the entire specimen surface.

Upon aging the sample at 900 F, the equilibrium α phase precipitates in a platy-acicular morphology within the β matrix, as illustrated in Figure 69(b). These plates, up to 1 micron long, are arranged in a Widmanstaetten pattern within the β grains. Pronounced heterogeneous nucleation is evident at a grain boundary where all the plates seem to emerge in the form of "columnar crystals"; the plate density at the boundary is greater than the density within the matrix (see right-hand edge). Even low-angle boundaries behave in a similar manner. Characteristically, because of the polymorphic nature of the transformation, there is no depletion zone adjacent to the pronounced boundary growth.

At a higher magnification [Figure 69(c)] the plates appear internally twinned, showing a series of fine-parallel markings across their widths; this may represent internal twinning or a two-phase dispersion. This point must be further checked by electron diffraction.

The α-β interface seems to be the center of many active dislocation sources. An active source which has thrown off three distinct, almost classical, loops is clearly seen near the top of Figure 69(c).

This new material, which has never been studied by transmission electron microscopy, must be thoroughly examined to develop a basic understanding of the fine-structural features governing its flow and fracture behavior.

Another phenomenon in this β alloy that must be more thoroughly investigated is the role of the so-called "ghost boundaries," which persist after annealing (Figure 70). These vestigial remains of a previous boundary network are apparently unsuccessful as grain-boundary pins, but local chemistry changes or precipitate stringers outline their location. These networks must play a role in the subsequent progress of deformation and fracture, and this must be carefully determined in further investigations.

XII.   SUMMARY AND CONCLUSIONS

Several high strength alloys (e.g., low-alloy AISI 4340, Type 422 stainless, and Crucible 218 hot-work type steels) were processed to 0.120-inch-thick sheets; work-hardened Type 301 stainless, PH15-7Mo precipitation-hardening stainless, and

B-120VCA beta titanium alloy were secured in sheet form, but had to be further cold-rolled to dimensions needed in the testing program.

Fracture testing, using smooth-sheet tensile specimens and fatigue-cracked center-notched tensile specimens, involved some development of technique to ensure quality of data. Slow-crack measurement by the movie film method was established as being superior to the ink-stain method in reliability and reproducibility.

Gross fracture appearance in notched tensile sheets that had failed were characterized in terms of a sixfold classification scheme. Ductile fractures above the full shear transition temperature were either the single-shear lip type or the partially stepped trough-and-ridge or double-shear types. On the other hand, fractures in the transition region were of the parallel-shear lip plus transverse fracture, orthogonal-shear lip plus stepped-transverse fracture or orthogonal-shear lip plus transverse fracture. Below the nil-ductility level, flat transverse fracture occupied the entire sample cross section.

The fine structures of quenched-and-tempered air-melted 4340 steel were characterized at various strength levels. Fracture-mode transition as a function of tempering was characterized, and the structural details of fracture topography were established on a submicroscopic scale. The 500 F embrittlement phenomenon in 4340 steel was found to be associated with a wide scatter obtained in fracture test data upon tempering in the 350 to 550 F region. Structurally, the simultaneous existence of regions of severely limited dislocation path length with other regions of greater dislocation motion explains the observed scatter in fracture-property data.

Three heat-treating variables and four melting variables were evaluated to determine their effect on structure and properties:

(1) Tempered martensite structures in 4340 steel are tougher than tempered bainite (lower bainite) at comparable strength level.

(2) Vacuum-induction melting (VIM and VIR) produced considerably tougher material than air-melted 4340; maximum fracture toughness of VIM and VIR was 220,000 psi $\sqrt{in.}$ but that of air-melted material was only about 110,000 psi $\sqrt{in.}$ One VAR heat showed properties similar to those of the air-melted material, but this behavior is suspected to be related to inclusion and segregation effects; further tests must be made on a cleaner heat of steel.

61

A complete characterizing of fine structures of Type 422 stainless steel at various strength levels revealed many interesting fine-structural sidelights, besides explaining the significant changes in strength properties as a function of thermal treatments. The presence of distinct microtwins within a needle-shaped martensite lath reopens a controversy on the role of microtwins in variable carbon martensites. The strengthening of Type 422 in the maximum secondary-hardening region and its delayed temper softening appear to be due to a pinned-dislocation strengthening mechanism.

Notch properties were evaluated at maximum yield strengths in order to gain higher sensitivity of notch properties to structural factors, even though a lower strength level would give the best compromise of strength and toughness. Notched tension tests (at a yield strength of 180,000 psi) gave a room-temperature fracture toughness, as a function of percentage shear (K_{c3}), of about 50,000 psi $\sqrt{in.}$ and a crack-propagation resistance factor of around 0.3.

Fine-structural study of Crucible 218 (H-11 type) explained the high-strength heat treatment, temper embrittlement, and overaging phenomena in terms of matrix fine structures, precipitation, and dislocation interactions. The classical midrib structure in martensite was explained by transmission microscopy. Fracture properties of Crucible 218 showed a transition region at 100 to 200 F. At room temperature, K_{c3} was about 50,000 psi $\sqrt{in.}$ at a yield strength of 220,000 psi.

Type 301 stainless steel, extra-work-hardened to about 249,000 psi yield strength level by cold rolling, was found to have longitudinal notch toughness, K_{c3} of about 135,000 to 140,000 psi $\sqrt{in.}$; however the transverse K_{c3} was only about 60,000 to 63,000 psi $\sqrt{in.}$ Aging at 750 F for 8 hours causes precipitation of M_2X and increases both smooth tensile strength properties and longitudinal notch toughness (K_{c3} of the order of 170,000 psi $\sqrt{in.}$ at a yield strength of 268,000 psi) the adverse transverse notch toughness is not remedied by this treatment. In transmission microscopy, chemical attack during polishing was found to be unrelated to dislocation pile-ups at twin boundaries. This phenomenon may be of considerable significance in stress-corrosion behavior of this alloy, and should be further explored.

Samples of PH15-7Mo semiaustenitic steel (refrigeration transformed as well as cold-roll transformed) were aged to the same room-temperature strength level of about 230,000 psi, and tested for notch strength. The material transformed by cold rolling was considerably tougher than that transformed by refrigeration; longitudinal K_{c3} values of about 51,000 psi $\sqrt{in.}$ in the refrigerated and aged condition, contrasted with 222,000 to 233,000 psi $\sqrt{in.}$ in the worked and aged condition. Transmission electron microscopy appears to be the only fine-structure technique that is capable of revealing the extremely fine precipitation of carbide upon aging after transformation of this alloy. The

coarse carbide precipitation during conditioning is easily discerned by extraction replica methods, and identified as $M_{23}C_6$.

B-120VCA beta titanium alloy was examined by transmission electron microscopy for the first time. This new study revealed some new elements of structure that may be of substantial significance in determining the strength of this material. The platy Widmanstaetten α precipitate contained fine internal markings, resembling microtwins, across their width. The α-β interfaces also suggest active dislocation sources.

Thus, the fine structures of several high strength alloys were characterized and correlated with strength and fracture properties to an extent never before achieved.

XIII. LITERATURE CITED

1. B. R. Banerjee and J. J. Hauser, "Research and Application Engineering to Determine the Effects of Processing Variables on Crack Propagation of High-Strength Steels and Titanium," ASD Contract No. AF33(616)-8156, First Quarterly Progress Report, August 1, 1961.

2. Ibid., Second Quarterly Progress Report, November 1, 1961.

3. Ibid., Third Quarterly Progress Report, February 1, 1962.

4. Ibid., Fourth Quarterly Progress Report, May 1, 1962.

5. Ibid., Fifth Quarterly Progress Report, August 1, 1962.

6. "Fracture Testing of High Strength Sheet Materials," ASTM Bull. 4, 29, 40 (1960); 5, 389, 877 (1961).

7. C. D. Beachem and J. E. Srawley, "Crack Propagation Tests of High Strength Sheet Materials," National Research Laboratory Report 5507, August 18, 1960; C. D. Beachem, "Effect of Test Temperature upon Topography of Fracture Surfaces of AMS 6434 Sheet Steel Specimens," National Research Laboratory Memorandum 1293, March 1962.

8. C. A. Zapffe and M. Clogg, Jr., Trans. ASM 34, 71 (1945).

9. J. Nutting and V. E. Cosslett, Metallurgical Applications of the Electron Microscope, Institute of Metals, London, 1950.

10. C. Crussard et al., J. Iron Steel Inst. 183, 146 (1956); J. Plateau, G. Henry, and C. Crussard, Rev. Univ. Mines 12, 1 (1956).

11. R. L. Scott and A. M. Turkalo, Proc. ASTM 57, 536 (1957).

12. A. Revere and R. Jaccodine, Project SR-122, Final Report to Ships Structure Committee, January 23, 1959 (Bishops Index No. NS-011-078).

13. W. C. Hagel and R. E. Smith, unpublished paper presented at the 1956 Annual Meeting, Electron Microscope Society of America.

14. J. R. Low, "Fracture," in Swampscott Symposium, John Wiley and Sons, Inc., New York, 1959, pp. 68-89.

15. G. Henry and J. Plateau, Fourth International Congress for Electron Microscopy, Julius Springer, Berlin, 1960, pp. 638-650.

16. C. Crussard, J. Plateau, R. Tamhankar, C. Henry, and D. Lajeunesse, "Fracture," in Swampscott Symposium, John Wiley and Sons, Inc., New York, 1959, pp. 524-561.

17. L. Smith, Naval Research Laboratory (private communication).

18. E. A. Steigerwald and G. L. Hanna, ASTM Preprint 74, 1962.

19. J. E. Campbell, "Review of Recent Developments," Battelle Memorial Institute, Columbus, June 29, 1962.

20. J. J. Hauser, J. M. Capenos, and B. R. Banerjee, Trans. ASM 54, 514 (1961).

21. K. H. Jack, J. Iron Steel Inst. (London) 162, 26 (1951).

22. R. H. Aborn, Trans. ASM 48, 51 (1956).

23. C. J. Klinger et al., Trans. ASM 46, 1557 (1954).

24. B. S. Lemont, Trans. ASM 45, 498 (1953) (discussion to A. G. Allten and P. Payson).

25. C. Crussard et al., "Fracture," in Swampscott Symposium, John Wiley and Sons, Inc., New York, 1959, p. 524.

26. J. A. Kies, A. M. Sullivan, and G. R. Irwin, J. Appl. Phys. 21, 716 (1950).

27. C. Crussard et al., J. Iron Steel Inst. (London) 183, 146 (1956).

28. N. A. Tiner, ASTM Preprint 82, 1961.

29. F. Staub and J. Tymowski, Hutnick 25, 133 (1958).

30. Tan Yü Rua, Acta Met. Sin., 262 (1959).

31. B. L. Averbach, Trans. AIME 197, 87 (1953).

32. W. Crafts and C. Offenhauer, Trans. AIME 150, 275 (1942).

33. C. Altstetter, Trans. AIME 224, 394 (1962).

34. M. Arbuzov and G. Kurdjumov, J. Phys. Acad. Nauk. SSSR 5, 101 (1941).

35. G. Kurdjumov and L. Lyssak, J. Iron Steel Inst. (London) 156, 29 (1947).

36. C. S. Roberts, B. L. Averbach, and M. Cohen, Trans. ASM 45, 576 (1953).

37. J. E. Srawley, "Resistance to Crack Propagation of High Strength Materials for Rocket Motor Casings," Quarterly Report No. 1, Project 5093-32-004.

38. P. M. Kelly and J. Nutting, J. Iron Steel Inst. (London) 197, 199 (1961).

39. M. Cohen, Trans. AIME 212, 171 (1958).

40. G. B. Espey, M. H. Jones, and W. F. Brown, Jr., Proc. ASTM 59, 837 (1959).

41. J. L. Shannon, Jr., et al. Proc. ASTM 60, 761 (1960).

42. J. C. Hamaker, Jr., and E. Vater, Proc. ASTM 60, 691 (1960).

43. B. R. Banerjee et al., J. Appl. Phys. 33, 556 (1961).

44. C. Crussard, Rev. Metallurgie 41, 111 (1944).

45. C. G. Dunn and F. W. Daniels, J. Metals 191, 147 (1951).

46. J. Talbot, C. de Beaulieu, and G. Chaudron, Compt. rend. 238, 2162 (1954).

47. J. N. Kellar, P. B. Hirsch, and J. S. Thorp, Nature 165, 554 (1950).

48. D. G. Brandon and J. Nutting, J. Iron Steel Inst. (London) 196, 160 (1960).

49. J. E. Srawley and C. D. Beachem, "Crack Propagation Tests of Some High Strength Sheet Steels," Naval Research Labbratory Report 5263, January 10, 1959.

50. G. K. Manning, "The Effect of Small Cracks on the Load-Carrying Ability of High Strength Steel," Sixty-Fourth Annual Meeting, American Society for Testing Materials.

51. J. Nutting, "Microstructure and Mechanical Properties," talk presented in Pittsburgh, Pennsylvania, April 11, 1962.

52. B. R. Banerjee, J. Metals, 13, 905 (1961).

53. G. Krauss, Jr., and B. L. Averbach, Trans. ASM 52, 435 (1960).

54. ASTM E-4-XI Committee, "Symposium on Advances in Electron Metallography," ASTM STP No. 245, p. 3 (1958).

55. A. L. Dalton, D. Webster, and H. C. Child, "Structural Processes in Creep," Iron and Steel Institute (London), Special Report 70, p. 166, 1961.

56. G. A. Bassett, J. W. Menter, and D. W. Pashley, Proc. Roy.Soc. (London) A246, 345 (1958).
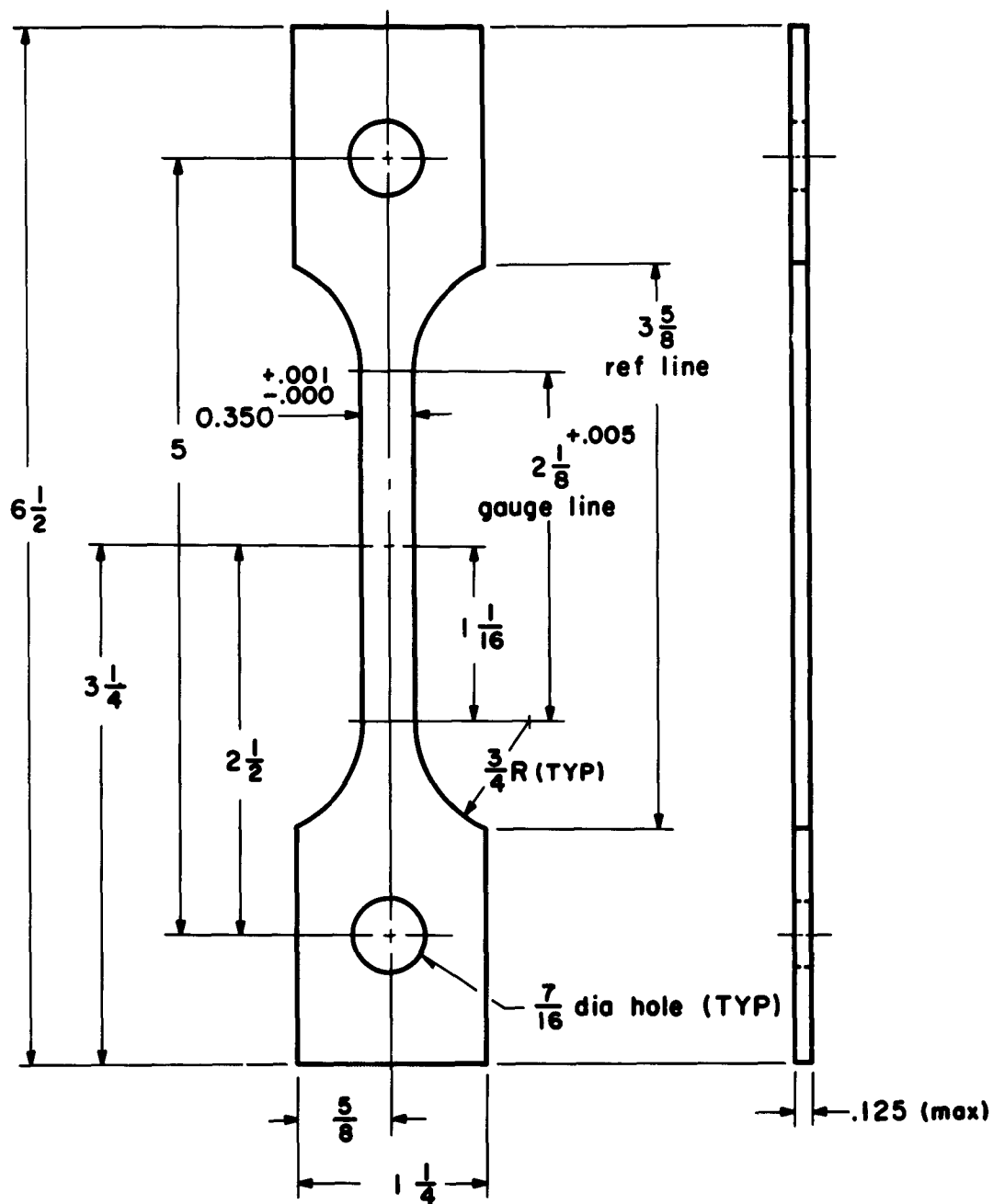
Center line of gauge section must correspond with diameter of holes.

Figure I

Smooth Sheet Tensile Specimen

68

Notes:
(1) Cut notch on ELOX MACHINE or equivalent.
(2) Extend notch into a crack 0.525 inch overall length by fatigue cycling.

Notch Detail
Scale : 3X Size

.003 Max. Notch Radius (Both Ends)

0.750 +.002 Dia.(2 Places)

0.030 to 0.080 Thickness Range

(b) Type 301 Stainless Specimen

Notes:
1. Cut notch on Elox machine or equivalent.
2. Extend notch into a crack 0.7 inch over-all length by fatigue cycling.

Notch Detail (2X)

.003 max notch radius (both ends)

.750 +.002 dia (TYP)

.044 to .125 (thickness range)

(a) Standard Specimen

Figure 2

Center – Notched Sheet Tensile Specimens

69

(a) Single Shear Lip

(b) Parallel Shear Lips

(c) Trough-and-Ridge Shear Lips

(d) Stepped Transverse Fracture and Orthogonal Shear Lips

(e) Orthogonal Shear Lips

(f) Flat Transverse Fracture

Schematic Diagram of Fracture Edge Contours
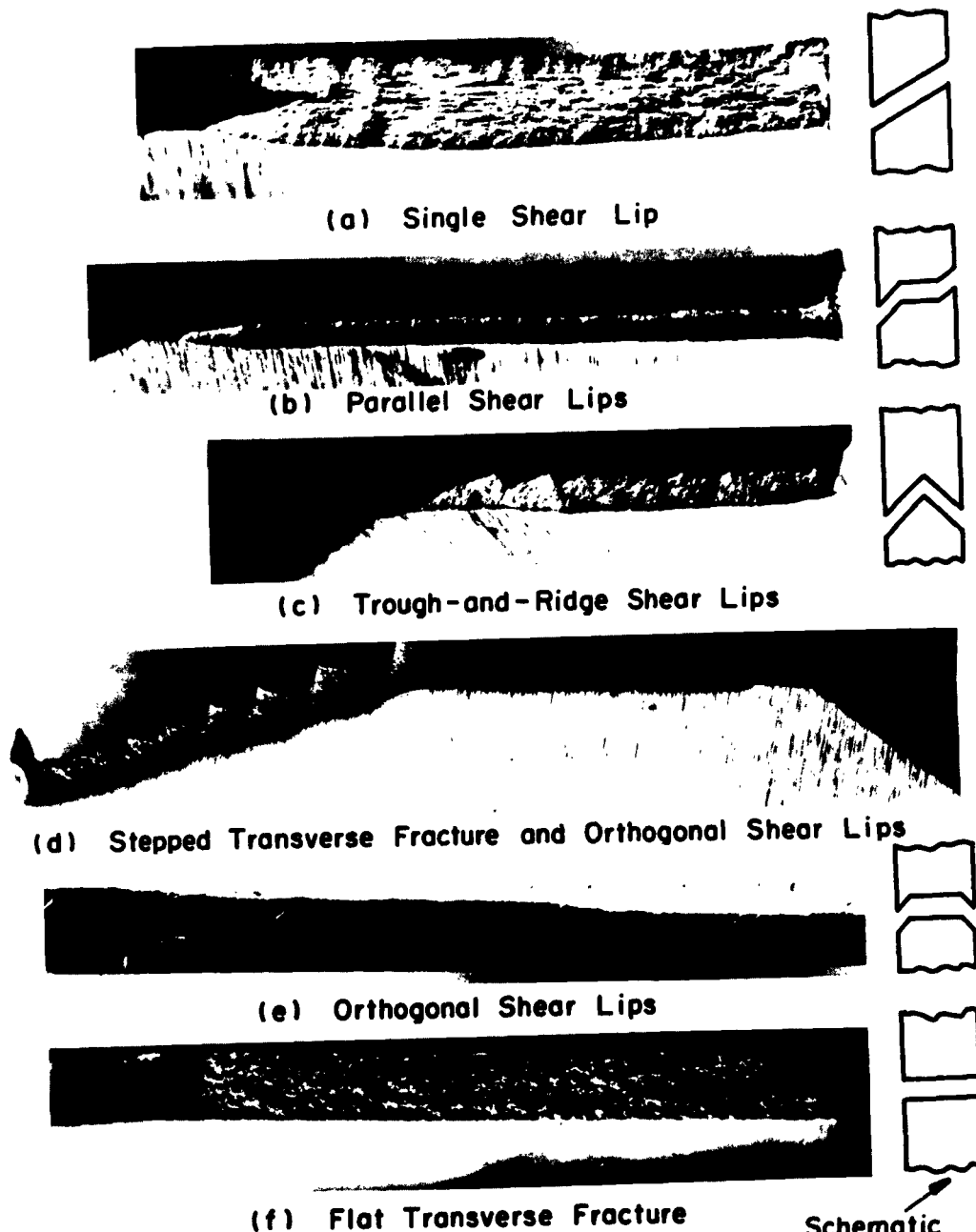
Figure 3

Gross Fracture Types in Notched Tensile Specimens of High-Strength Steels

Figure 4

Edge-Nucleated Fracture in Air-Melted 4340 Steel
Obscuring True Indication of Percentage Shear
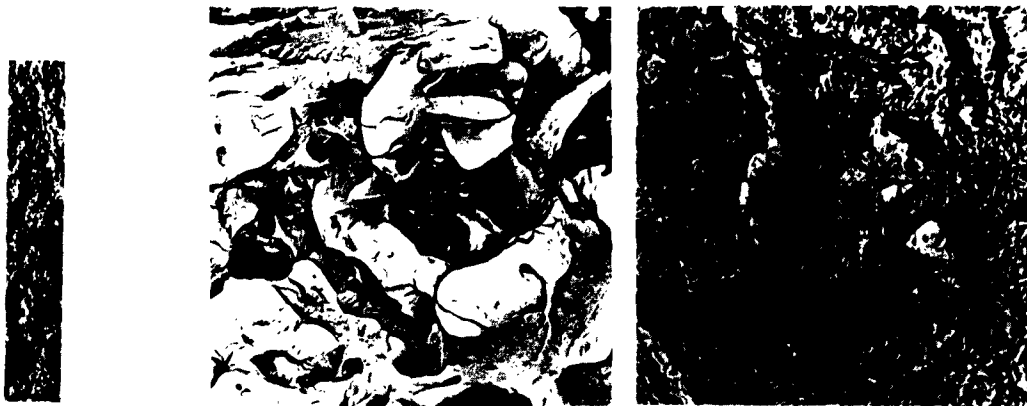
Fractured at 70 F (Shows Flat Fracture Facets)
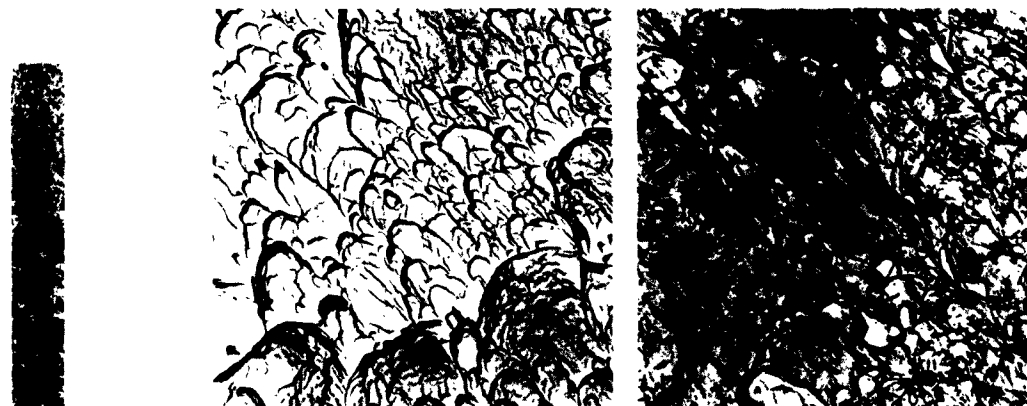
Fractured at 300 F (Shows Parabolic Dimples)

(9X)	1 μ	
(a)	(b)	(c)
Macrograph	Submicrofractograph	Etch-Shadow Extraction Replica

Figure 5

Fracture Surfaces of Type 422 Stainless Steel
Quenched and Tempered at 900 F for 2 Hours

(a)

(b)

1μ
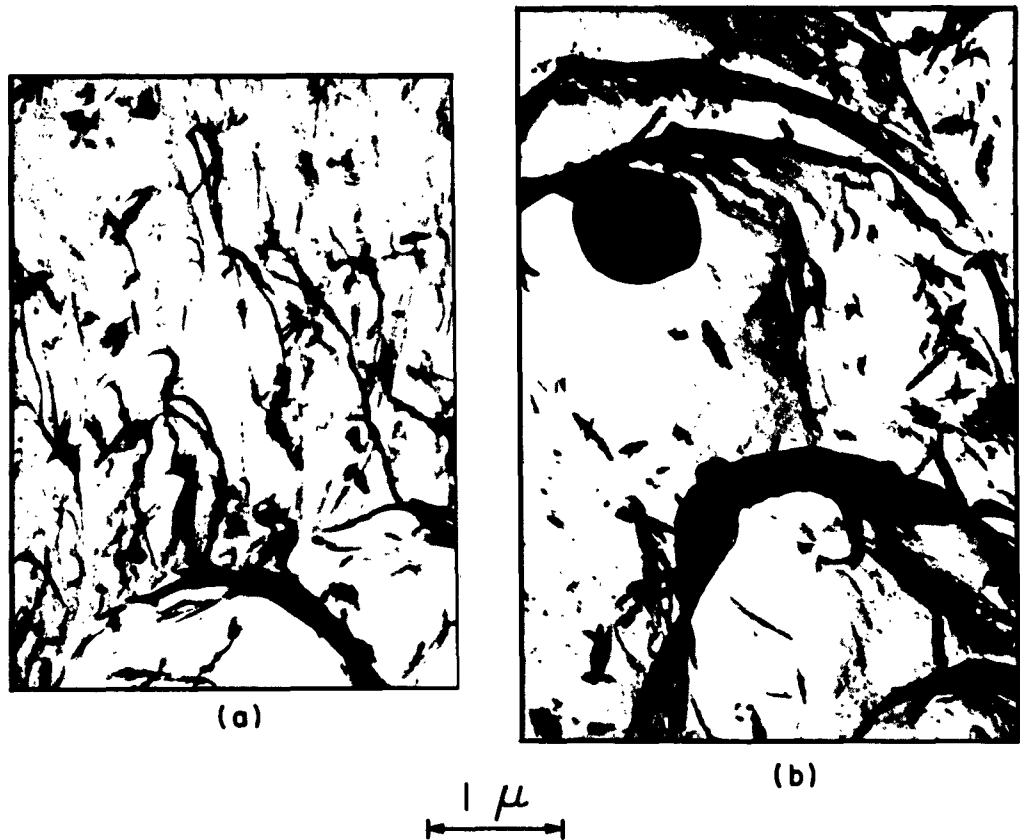
Figure 6

Structural Details within Parabolic Dimples as seen
in Etch – Shadow Extraction Replicas

Note parabolic fractures nucleated by precipitated
particles and by an inclusion.

73

Figure 7

Centrally Notched Tensile Specimen That Had Ink Drawn
beyond Slow-Crack Length during Testing

(a) Specimen 10B20

$K_{cI} = 205,000$ psi $\sqrt{in}$.

(b) Specimen 23L19

$K_{cI} = 160,000$ psi $\sqrt{in}$.

(c) Specimen 23K21

$K_{cI} = 151,000$ psi $\sqrt{in}$.
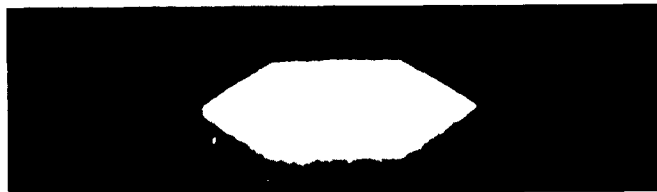
(d) Specimen 23K19

$K_{cI} = 111,000$ psi $\sqrt{in}$.

(e) Specimen 23G13

$K_{cI} = 100,000$ psi $\sqrt{in}$.

Figure 8

Movie Frames Just Prior to Onset of Rapid Crack Propagation
in 4340 Centrally Notched Samples

Note extent of cracks and occasional asymmetry ; forked appearance
represent localized deformation in the plastic zone surrounding the
slow crack.

Movie taken at 24 frames/sec.

K_{cI} = Fracture toughness as a function of critical crack length.

75
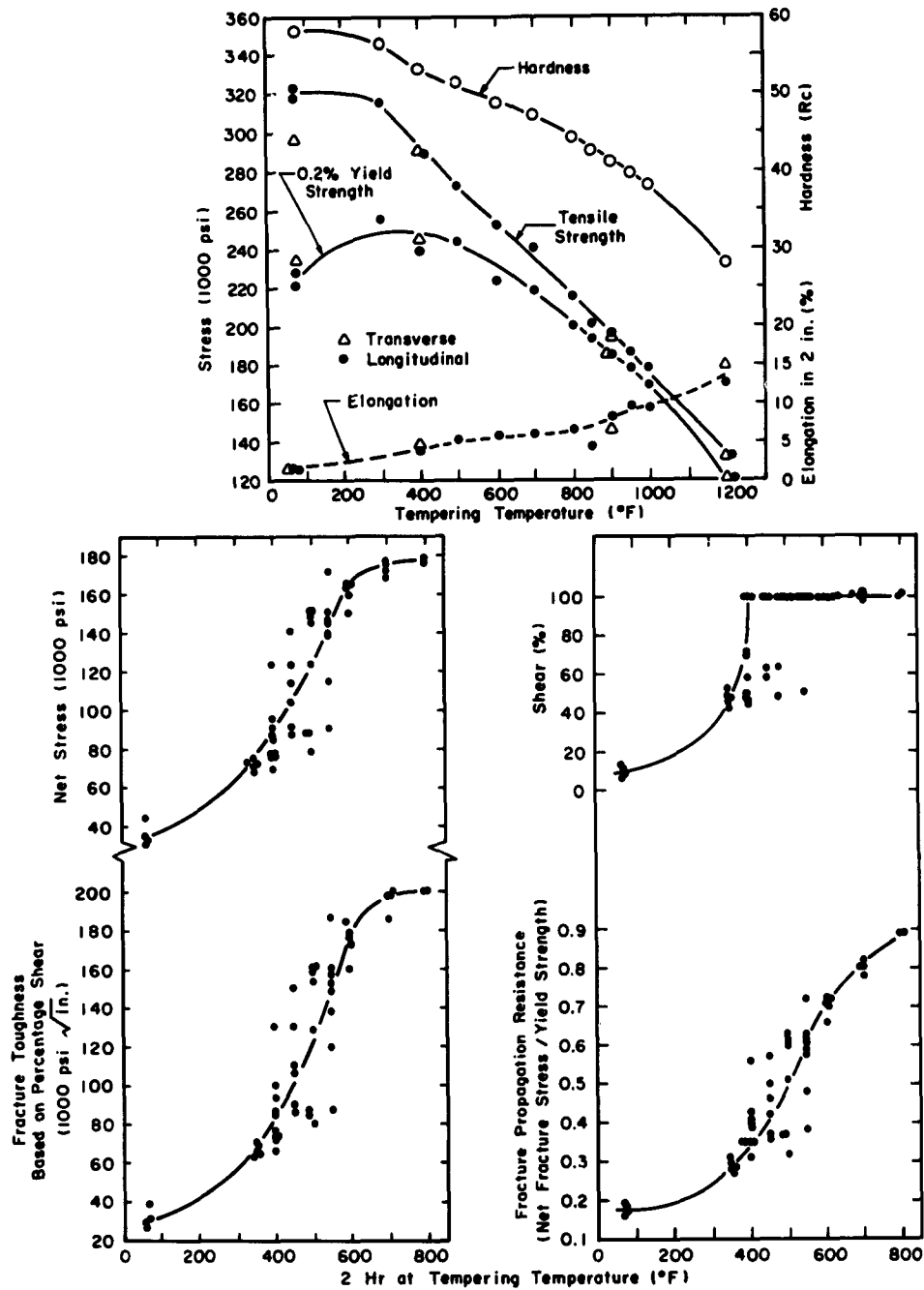
Figure 9

Mechanical Test Results as a Function of Tempering Temperature
for Air-Melted 4340 Steel

(a) Surface Replica
Micrograph (15,000X)
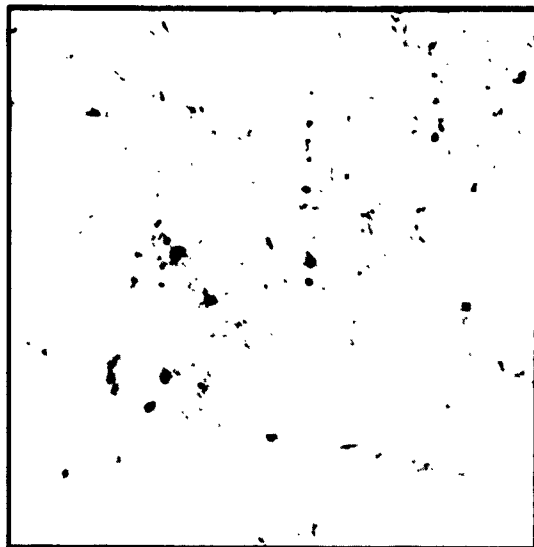
(b) Extraction Replica
Micrograph (30,000X)

(c) Thin Film Transmission Electron
Micrograph (20,000X)
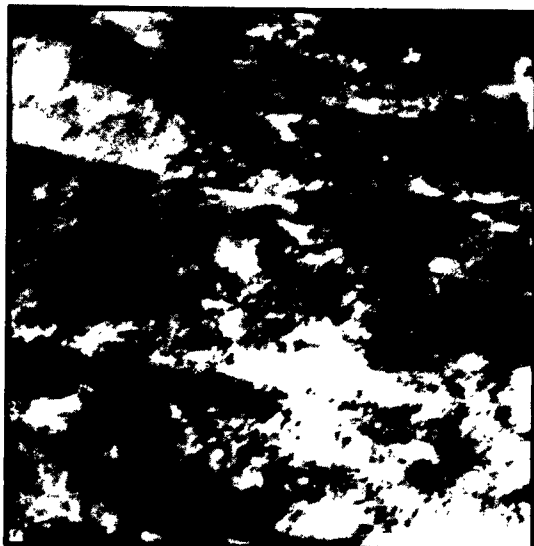
(d) Thin Film Transmission Electron
Micrograph (60,000X)

Figure 10

Micrographs of Air-Melted 4340 Steel Oil Quenched
from 1550 F and Refrigerated at -320 F

5% Picral + 0.2% HCl
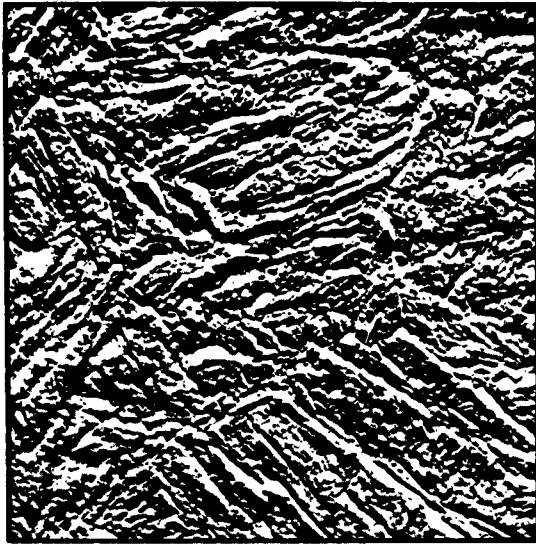
(a) Surface Replica
Micrograph (15,000X)
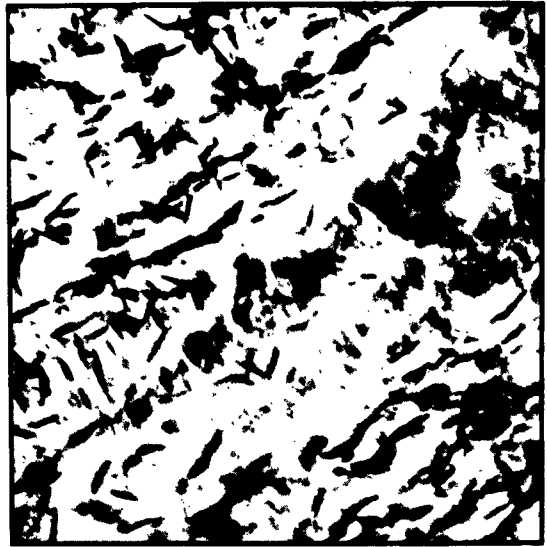
(b) Extraction Replica
Micrograph (30,000X)
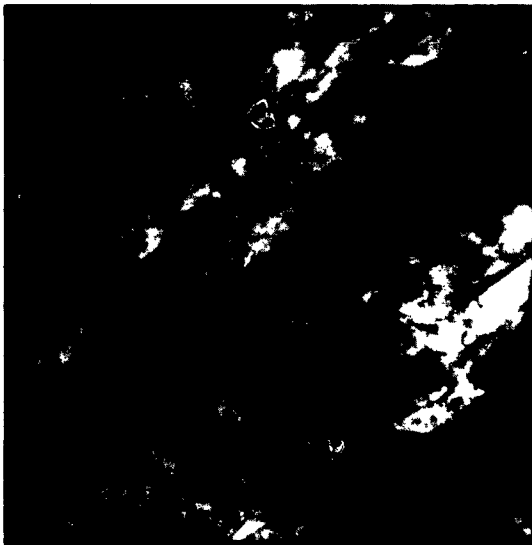
(c) Thin Film Transmission Electron
Micrograph (60,000X)
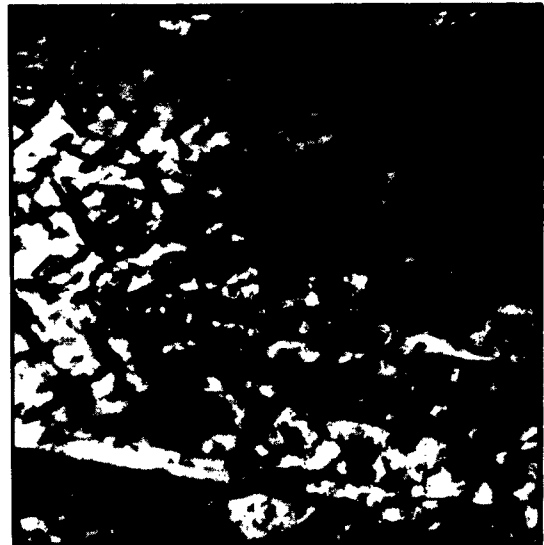
(d) Thin Film Transmission Electron
Micrograph (41,000X)

Figure II

Micrographs of Air-Melted 4340 Steel Tempered
at 400 F for 2 Hours

5% Picral + 0.2% HCl

78

(a) Surface Replica
Micrograph (15,000X)

(b) Extraction Replica
Micrograph (30,000X)

(c) Thin Film Transmission Electron
Micrograph (20,000X)

(d) Thin Film Transmission Electron
Micrograph (60,000X)

Figure 12

Micrographs of Air-Melted 4340 Steel Tempered
at 800 F for 2 Hours

5% Picral + 0.2% HCl

79

(a) Surface Replica
Micrograph (15,000X)

(b) Extraction Replica
Micrograph (30,000X)

(c) Thin Film Transmission Electron
Micrograph (20,000X)

(d) Thin Film Transmission Electron
Micrograph (60,000X)

Figure 13

Micrographs of Air-Melted 4340 Steel Tempered
at 900 F for 2 Hours

5% Picral + 0.2% HCI
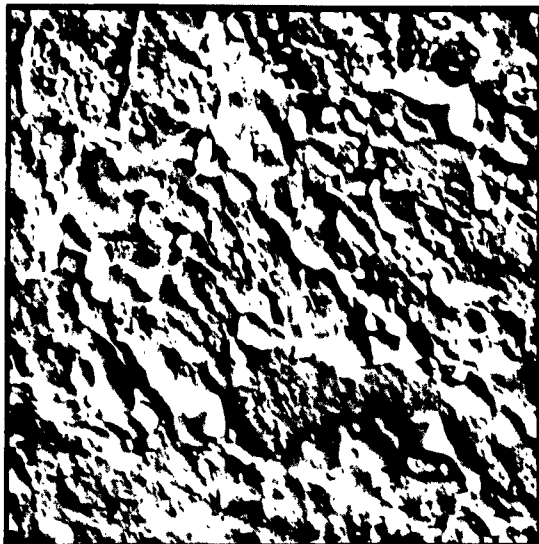
(a) Surface Replica
Micrograph (15,000X)

(b) Extraction Replica
Micrograph (30,000X)

(c) Thin Film Transmission Electron
Micrograph (20,000X)

(d) Thin Film Transmission Electron
Micrograph (60,000X)

Figure 14

Micrographs of Air-Melted 4340 Steel Tempered
at 1200 F for 2 Hours

5% Picral + 0.2% HCl

81

Oil Quenched

400 F for 2 hr

900 F for 2 hr

1200 F for 2 hr

Longitudinal   Transverse

Figure 15

Fracture Surfaces of Smooth Tensile Specimens
of Air-Melted 4340 Steel

Tested at 70 F

(a) From Central Region (5,300X)
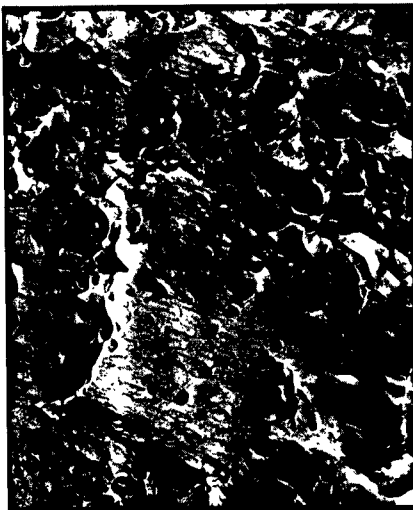
(b) From Shear Lip (5,300X)
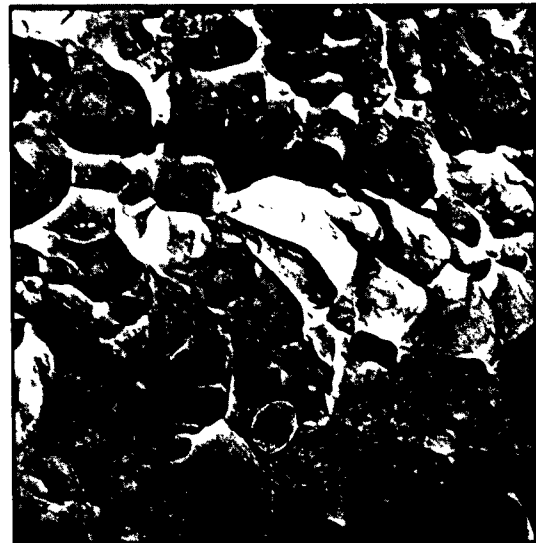
(c) From Shear Lip (15,000X)

Figure 16

Fracture Surfaces of 4340 Steel at Tensile
Strength of 320,000 psi

Longitudinal, smooth tensile (as quenched).

83

(a) From Central Region (5,300X)

(b) From Central Region (15,000X)
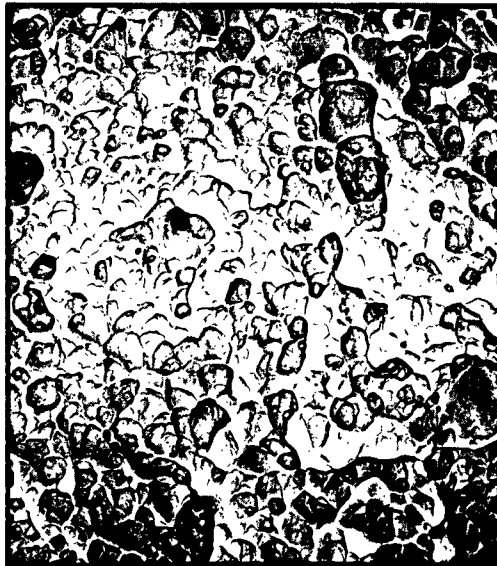
(c) From Shear Lip (5,300X)

Figure 17

Fracture Surfaces of 4340 Steel at Tensile
Strength of 320,000 psi

Transverse, smooth tensile (as quenched).

(a) Longitudinal (5,300X)

(b) Longitudinal (15,000X)
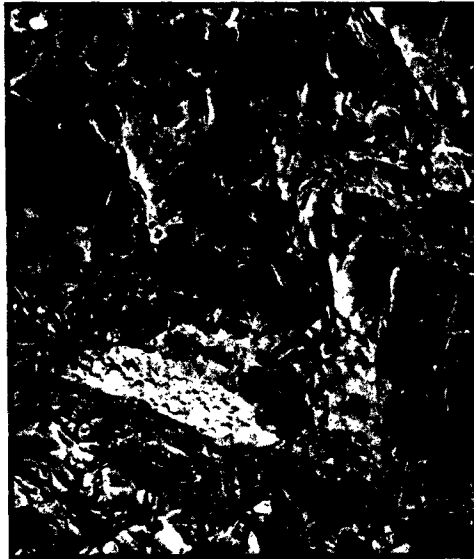
(c) Transverse (5,300X)

Figure 18

Fracture Surfaces of Steel 4340 at Tensile
Strength of 280,000 psi

Smooth tensile (tempered at 400 F).

(a) Longitudinal (5,300X)

(b) Longitudinal (15,000X)
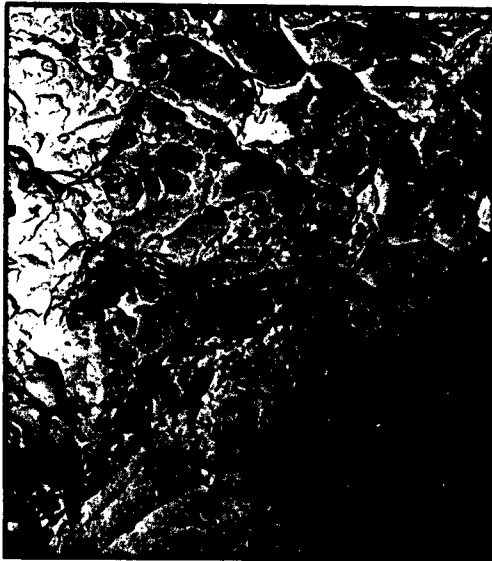
(c) Transverse (5,300X)

(d) Transverse (15,000X)

Figure 19

Fracture Surfaces of 4340 Steel at Tensile
Strength of 190,000 psi

Smooth tensile (tempered at 900 F).

86

(a) Longitudinal (5,300X)

(b) Longitudinal (15,000X)

(c) Transverse (5,300X)

(d) Transverse (15,000X)

Figure 20

Fracture Surfaces of 4340 Steel at Tensile
Strength of 130,000 psi

Smooth tensile (tempered at 1200 F).

87
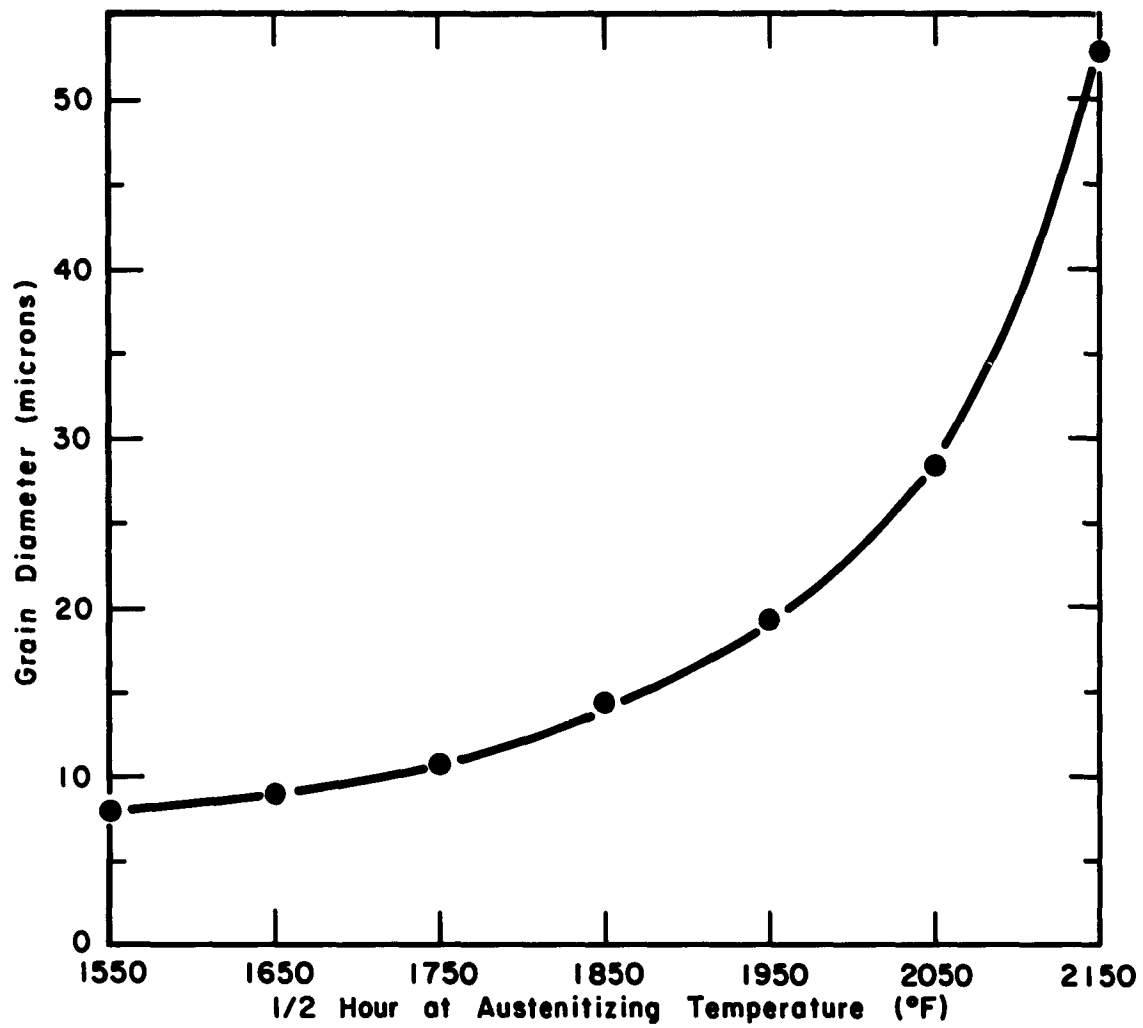
Figure 21

Grain Size of Air — Melted 4340 Steel
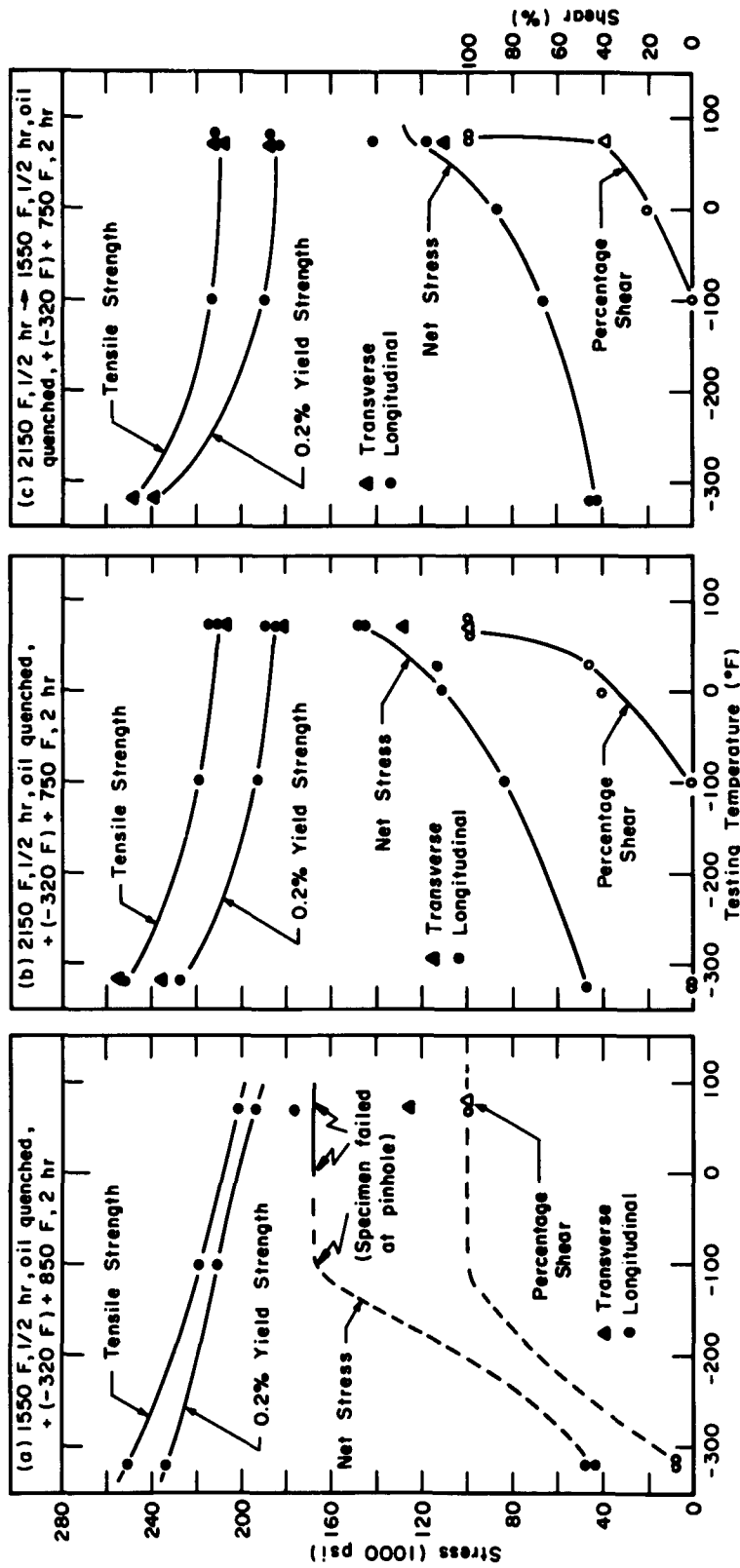
Figure 22

Properties of Air-Melted 4340 Steel (0.067-Inch-Thick Specimens) Given Modified Treatments to Produce a 190,000 psi Yield Strength at Room Temperature

89

Properties of Tempered Martensite and Tempered Bainite (at an Equivalent Strength Level) in Air-Melted 4340 Steel
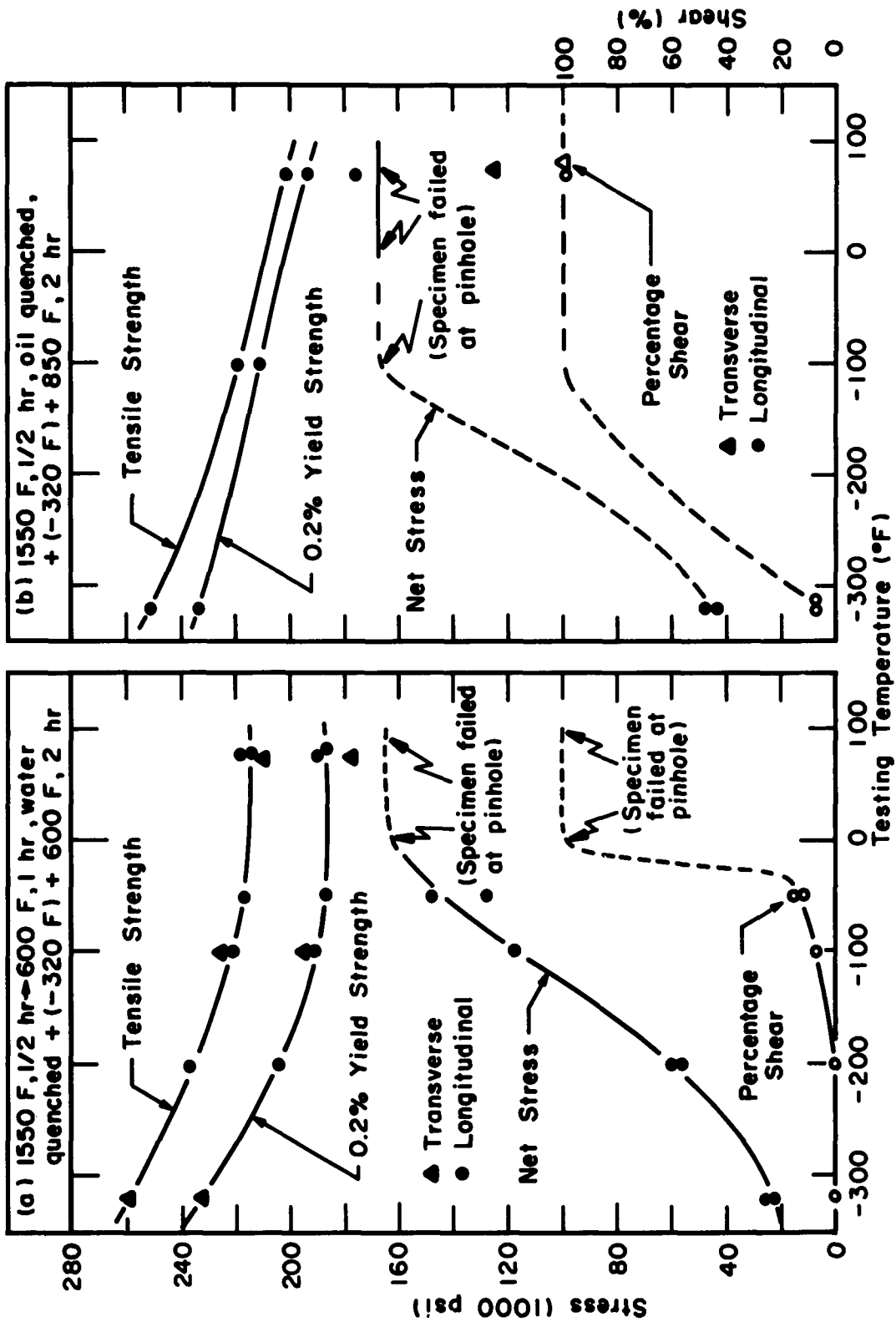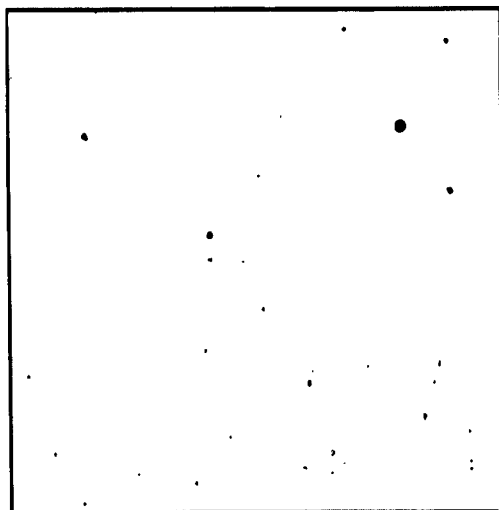
Figure 23
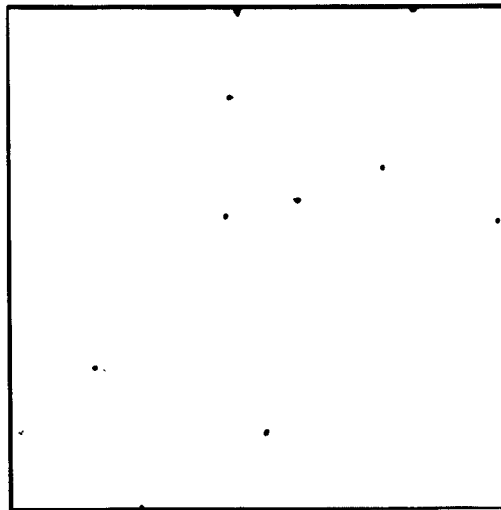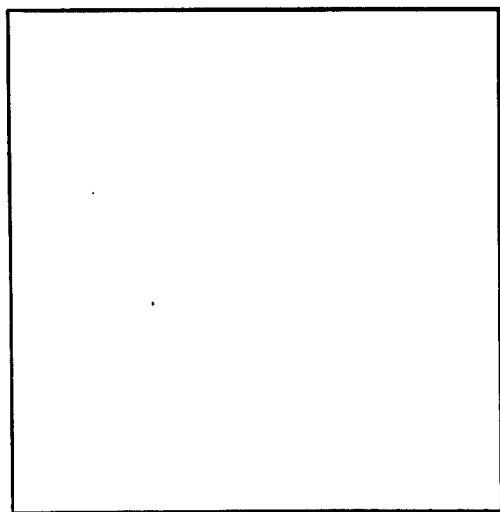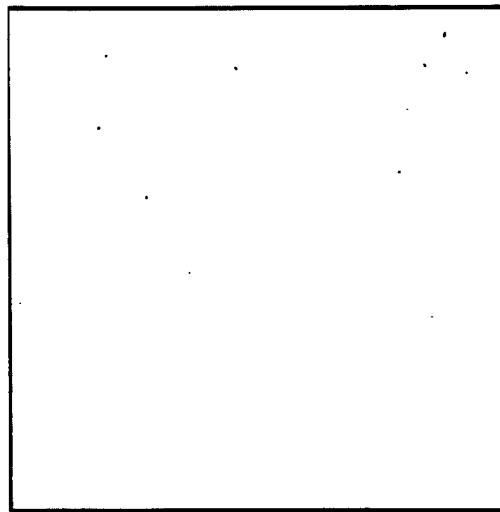
Air Melted   VAR

VIR   VIM

Figure 24

Nonmetallic Inclusions in Melt-Variable AISI 4340 (100X)
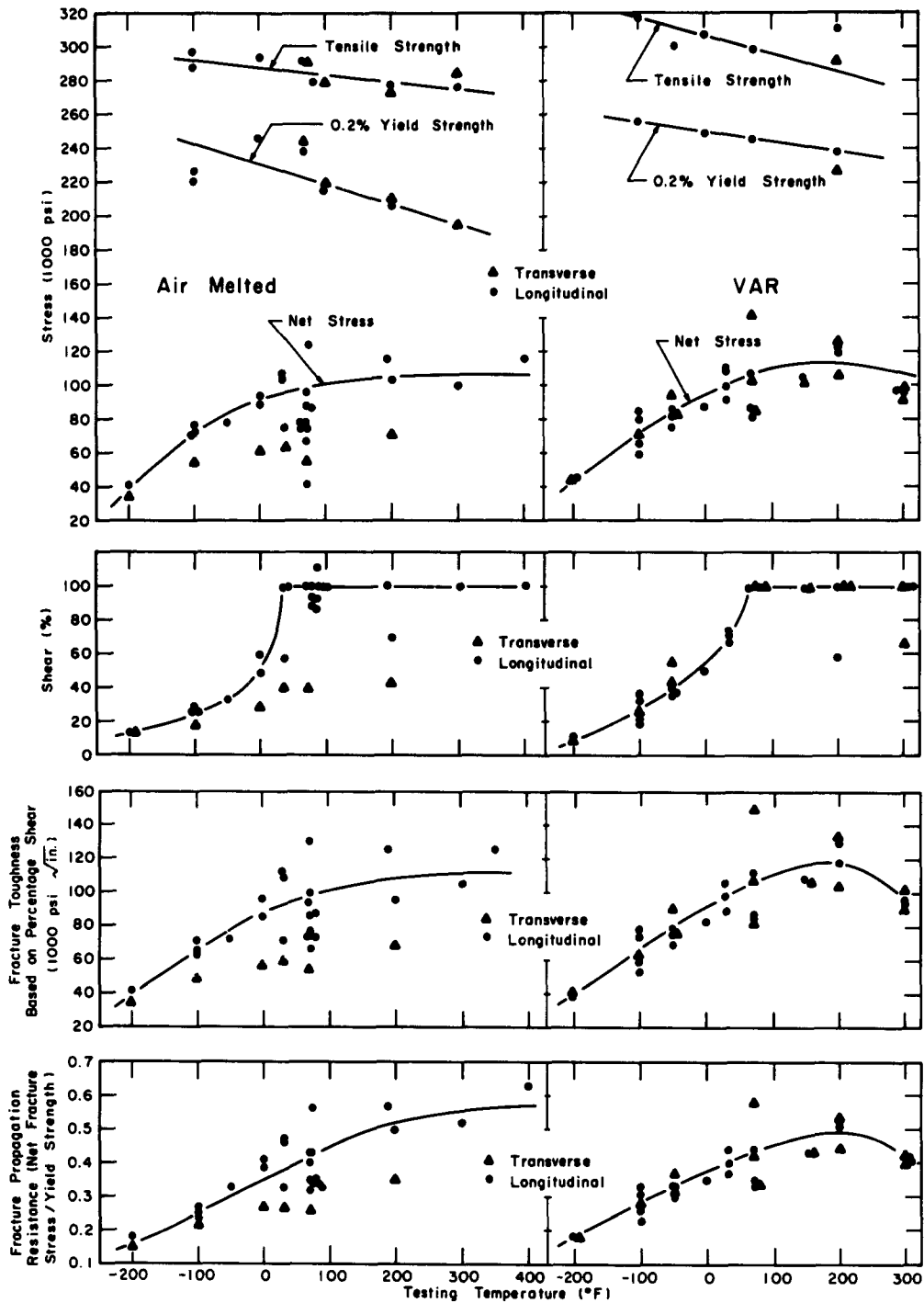
Figure 25

Smooth - Bar Tensile Properties and Notch Strength Properties
of Air - Melted and Vacuum - Arc - Remelted 4340 Steel

Austenitized at 1550 F for 1/2 hour, oil quenched, refrigered at −320 F,
and tempered at 400 F for 2 hours.
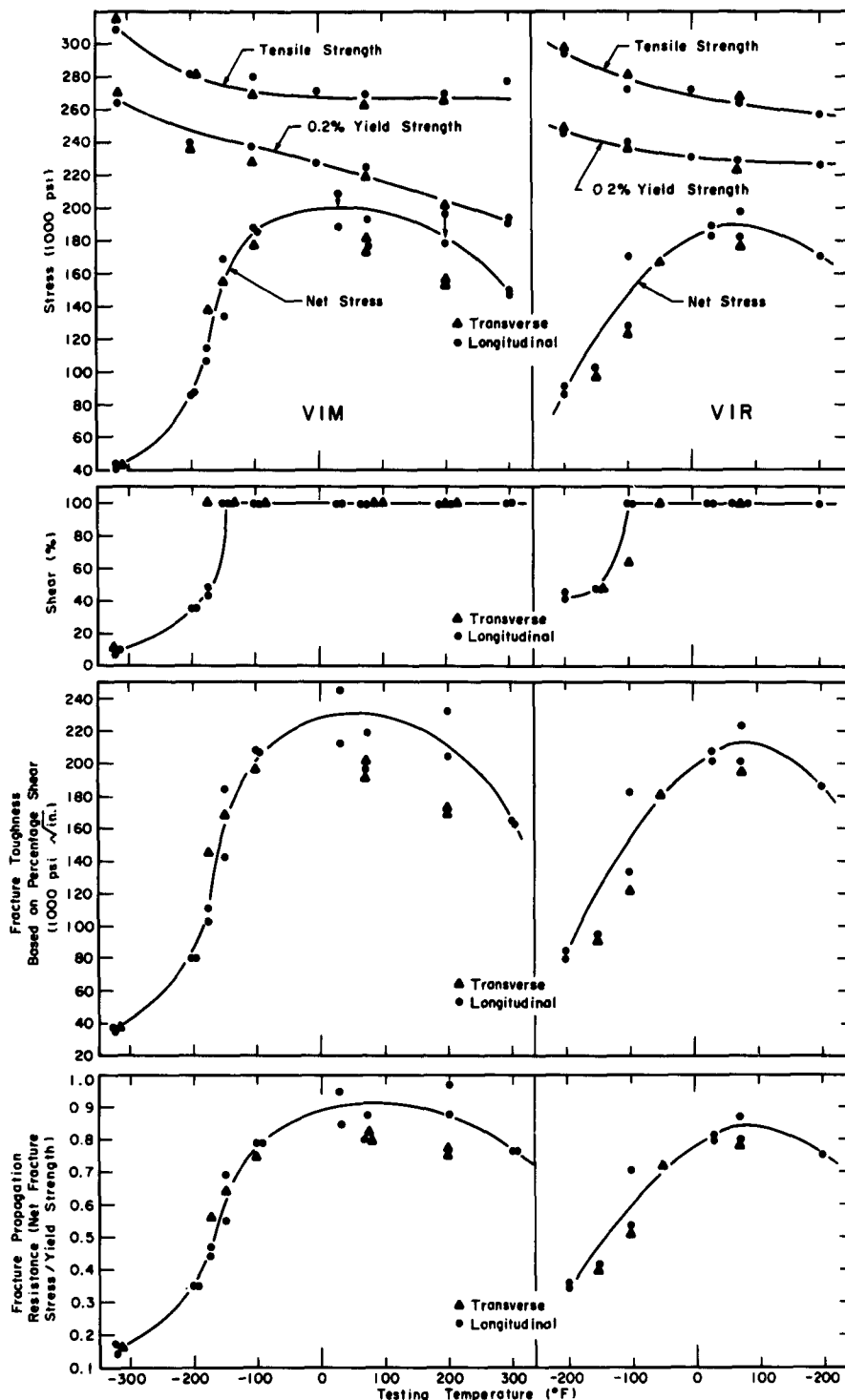
Figure 26

Smooth-Bar Tensile Properties and Notch Strength Properties of Vacuum-Induction-Melted and Vacuum-Induction-Remelted 4340 Steel

Austenitized at 1550 F for 1/2 hour, oil quenched, refrigerated at -320 F, and tempered at 400 F for 2 hours.

93
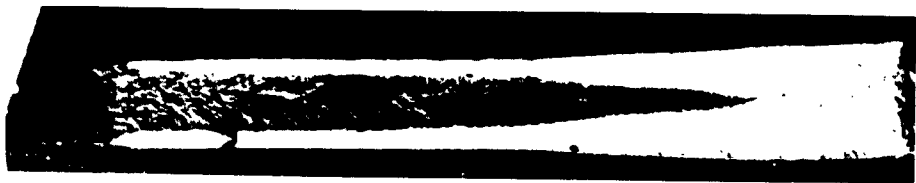
Air Melted and Tested at 70 F
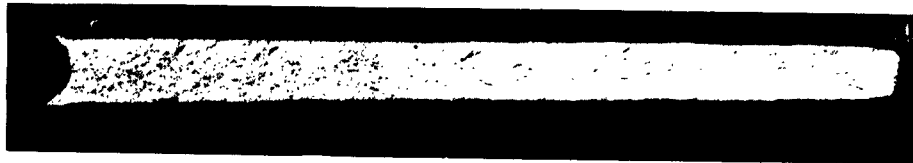
Air Melted and Tested at −100 F
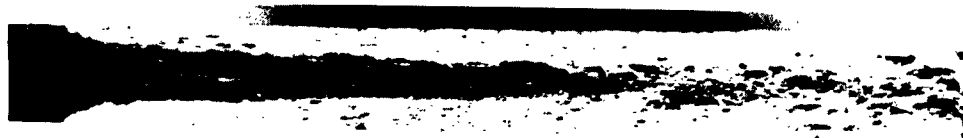
VAR and Tested at 70 F

VAR and Tested at −100 F

VIR and Tested at 70 F
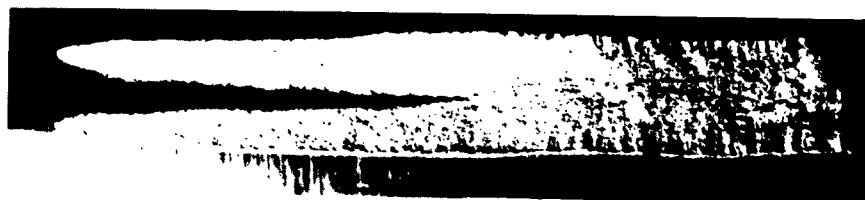
VIR and Tested at −100 F

Figure 27

Fracture Appearance of Longitudinal Notch−Tensile Samples
of Air Melted, VAR, and VIR 4340

Longitudinal specimens oil quenched from 1550 F, refrigerated at
−320 F, and tempered at 400 F for 2 hours.

94
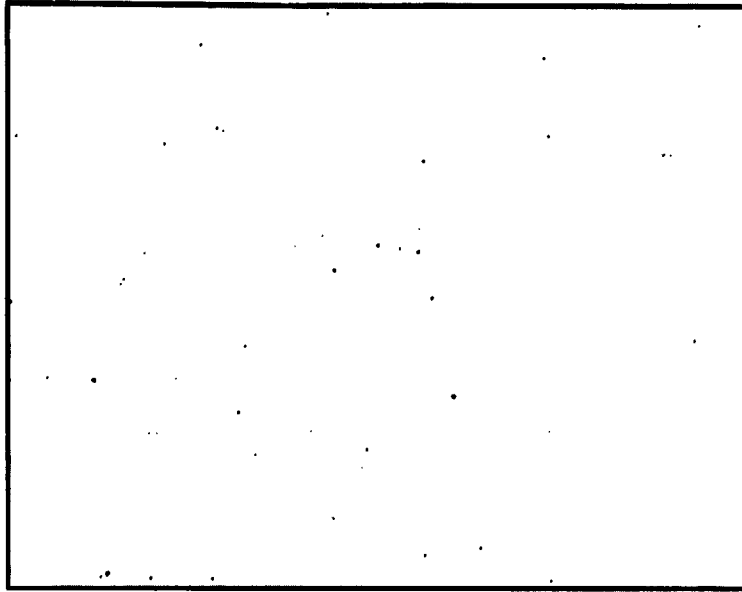
Figure 28

Typical Inclusion Content in Type 422 Stainless Steel (100X)
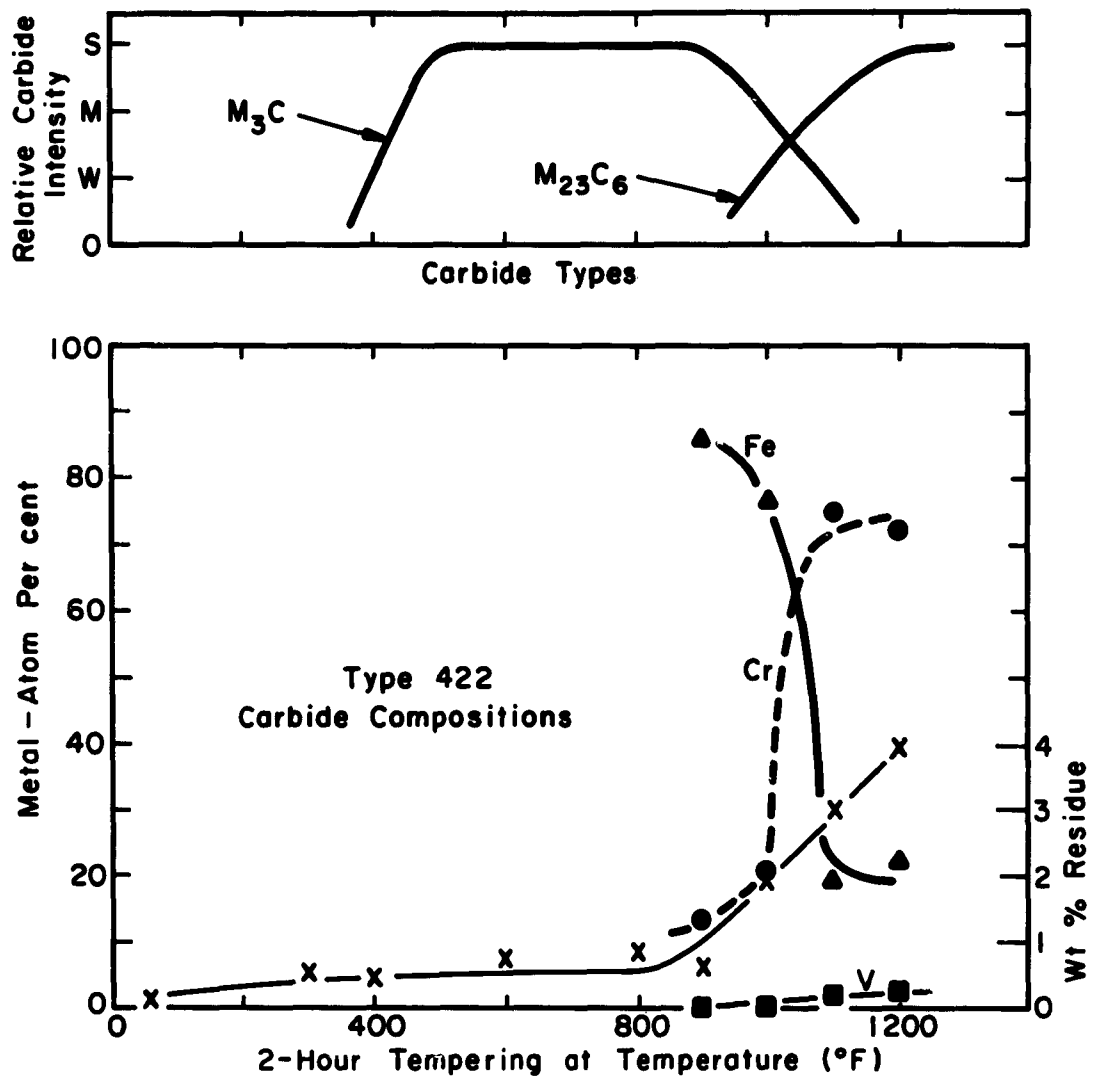
Figure 29

Carbide Analysis of Type 422 Stainless Steel
as a Function of Tempering Temperature
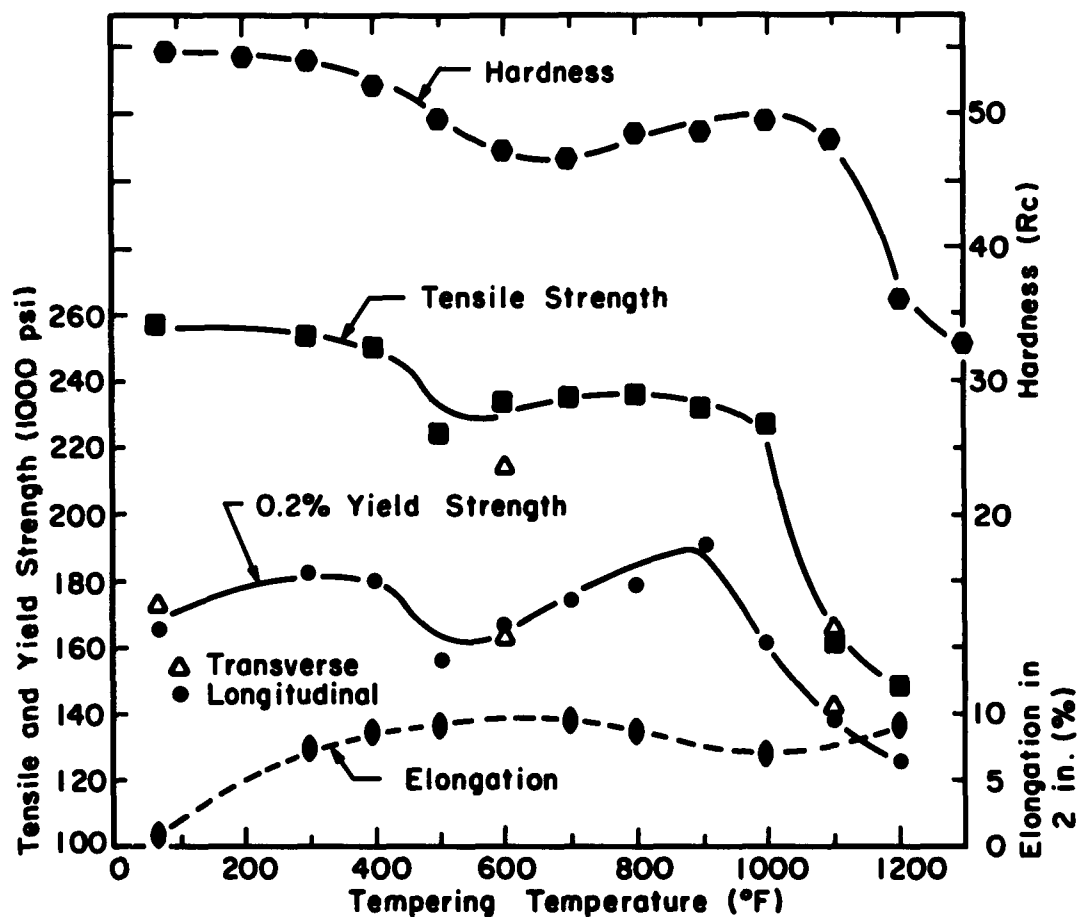
Figure 30

Hardness and Smooth Bar Tensile Properties of
Tempered Type 422 Stainless

(a) Surface Replica (15,000X)
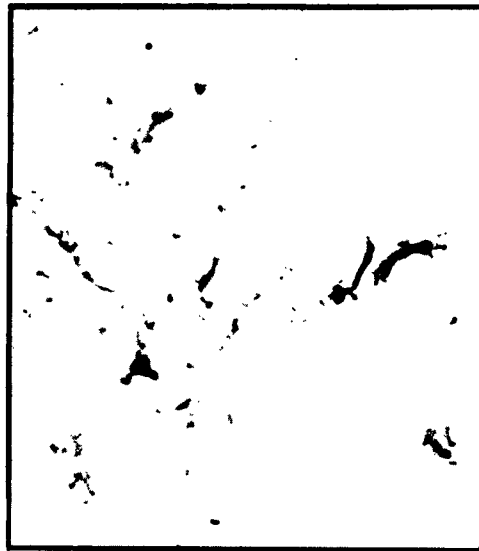
(b) Extraction Replica (25,000X)

(c) Thin Section (30,000X)

(d) Thin Section (60,000X)

Figure 31

Micrographs of Type 422 Stainless Steel Oil-Quenched
from 1900 F and Refrigerated at -320 F

Vilella's Reagent

(a) Surface Replica (15,000X)

(b) Extraction Replica (25,000X)

(c) Thin Section (30,000X)
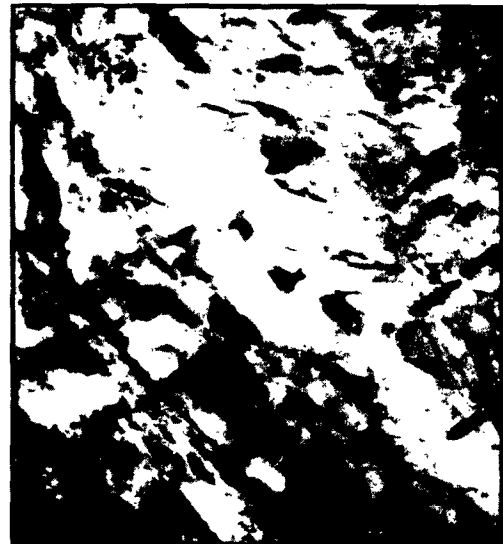
(d) Thin Section (60,000X)

Figure 32

Micrographs of Type 422 Stainless Steel
Tempered at 400 F for 2 Hours

Vilella's Reagent

(a) Surface Replica (15,000X)

(b) Extraction Replica (25,000X)

(c) Thin Section (30,000X)

(d) Thin Section (60,000X)

Figure 33

Micrographs of Type 422 Stainless Steel
Tempered at 500 F for 2 Hours

Vilella's Reagent

(a) Surface Replica (15,000X)   (b) Extraction Replica (25,000X)

(c) Thin Section (25,000X)   (b) Thin Section (60,000X)

Figure 34

Micrographs of Type 422 Stainless Steel
Tempered at 700 F for 2 Hours

Vilella's Reagent
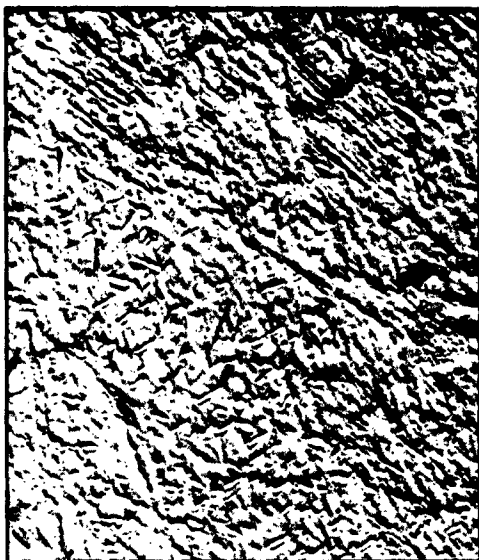
(a) Surface Replica (15,000X)

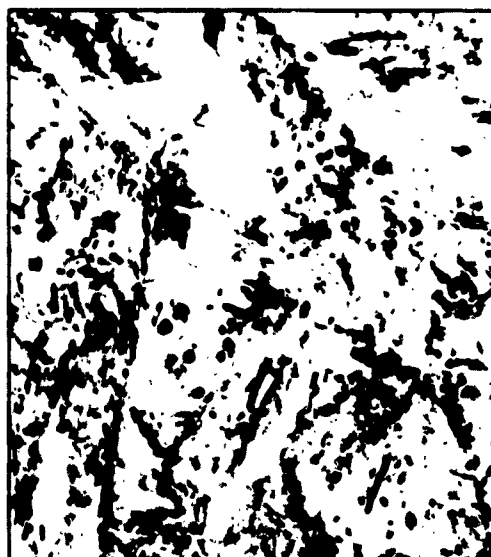(b) Extraction Replica (25,000X)
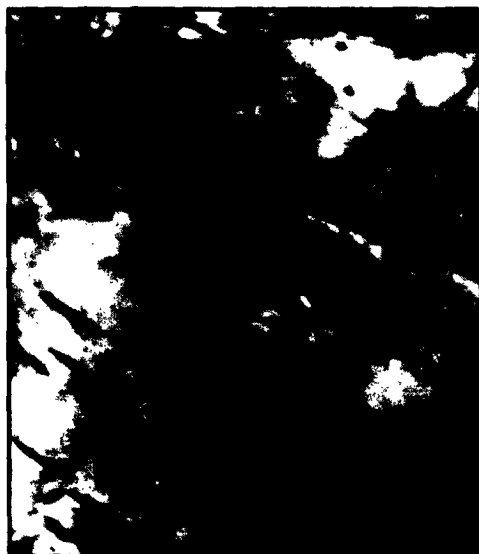
(c) Thin Section (30,000X)

(d) Thin Section (60,000X)

Figure 35

Micrographs of Type 422 Stainless Steel
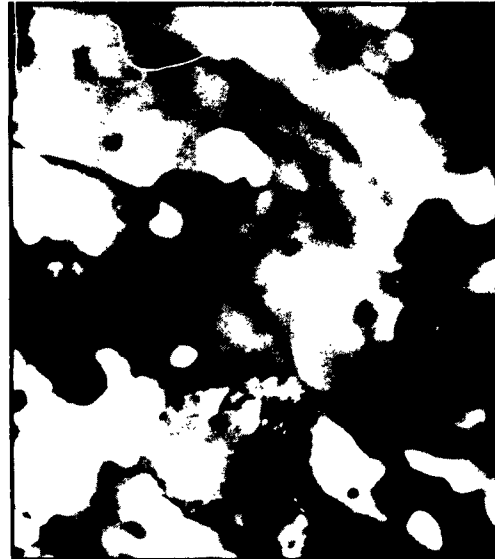Tempered at 800 F for 2 Hours

Vilella's Reagent

(a) Surface Replica (15,000X)

(b) Extraction Replica (25,000X)

(c) Thin Section (30,000X)

(d) Thin Section (60,000X)

Figure 36

Micrographs of Type 422 Stainless Steel
Tempered at 900 F for 2 Hours

Vilella's Reagent

103

(a) Surface Replica (15,000X)   (b) Extraction Replica (25,000X)

(c) Thin Section (30,000X)   (d) Thin Section (60,000X)

Figure 37

Micrographs of Type 422 Stainless Steel
Tempered at 1000 F for 2 Hours

Vilella's Reagent

(a) Surface Replica (15,000X)

(b) Extraction Replica (25,000X)

(c) Thin Section (30,000X)

(d) Thin Section (60,000X)

Figure 36

Micrographs of Type 422 Stainless Steel
Tempered at 900 F for 2 Hours
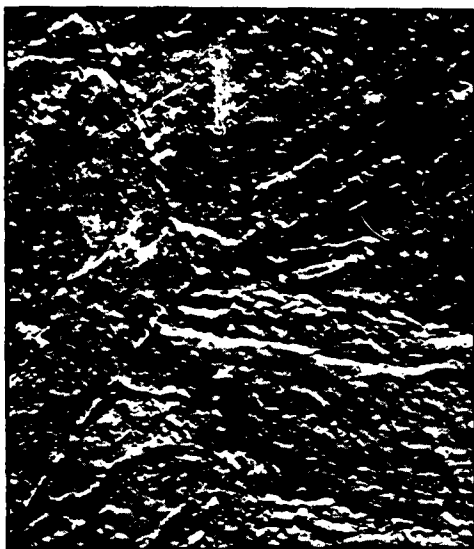
Vilella's Reagent

(a) Surface Replica (15,000X)

(b) Extraction Replica (25,000X)

(c) Thin Section (30,000X)

(d) Thin Section (60,000X)

Figure 38

Micrographs of Type 422 Stainless Steel
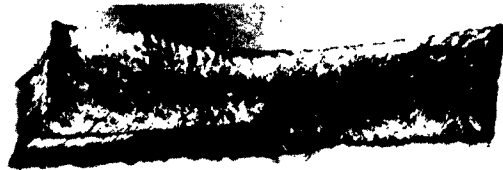Tempered at 1100 F for 2 Hours

Vilella's Reagent

(a) Surface Replica (15,000X)

(b) Extraction Replica (25,000X)

(c) Thin Section (30,000X)

(d) Thin Section (60,000X)

Figure 39

Micrographs of Type 422 Stainless Steel
Tempered at 1300 F for 2 Hours

Vilella's Reagent

106
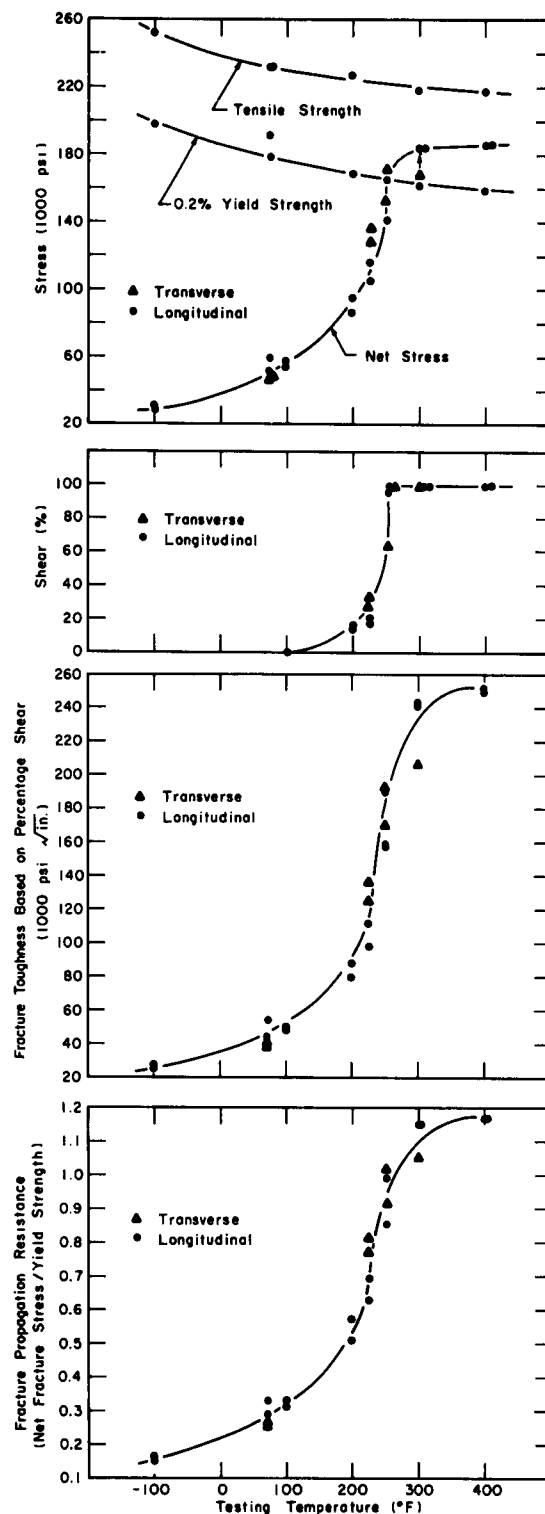
Figure 40

Properties of Type 422 Stainless Steel

0.067 - inch - thick specimens austenitized at 1900 F for I hr, oil quenched, refrigerated at -320 F, and tempered at 900 F for 2 hr.
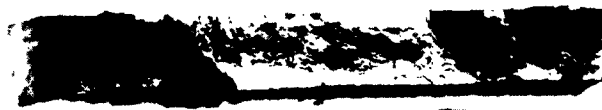
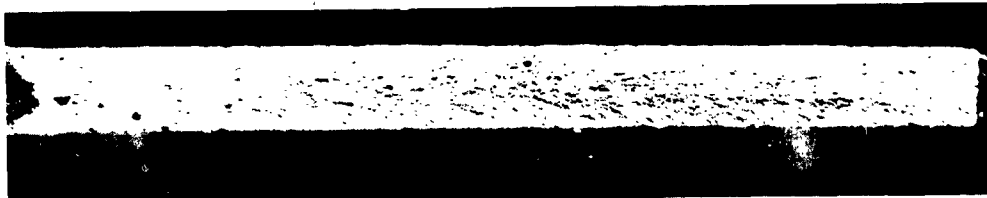Longitudinal Specimen Tested at 70 F
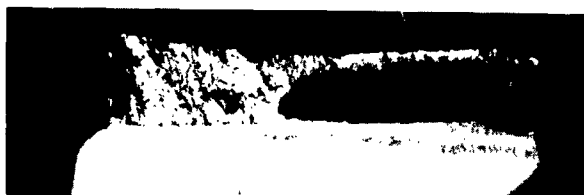
Longitudinal Specimen Tested at 300 F

Transverse Specimen Tested at 70 F
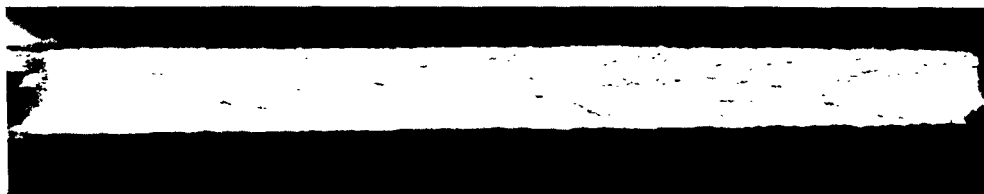

Transverse Specimen Tested at 300 F

Figure 41

Fracture Surfaces of Smooth-Bar Tensile Specimen of Type 422
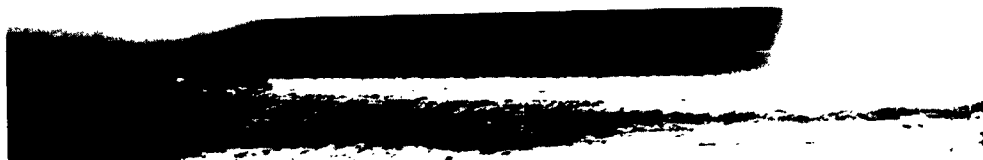Stainless Steel Quenched and Tempered at 900 F for 2 Hours

Longitudinal Specimen Tested at 70 F

Longitudinal Specimen Tested at 300 F

Transverse Specimen Tested at 70 F

Transverse Specimen Tested at 300 F

Figure 42

Fractured Surfaces of Centrally Notched Specimens of Type 422
Stainless Steel Quenched and Tempered at 900 F for 2 Hours

109
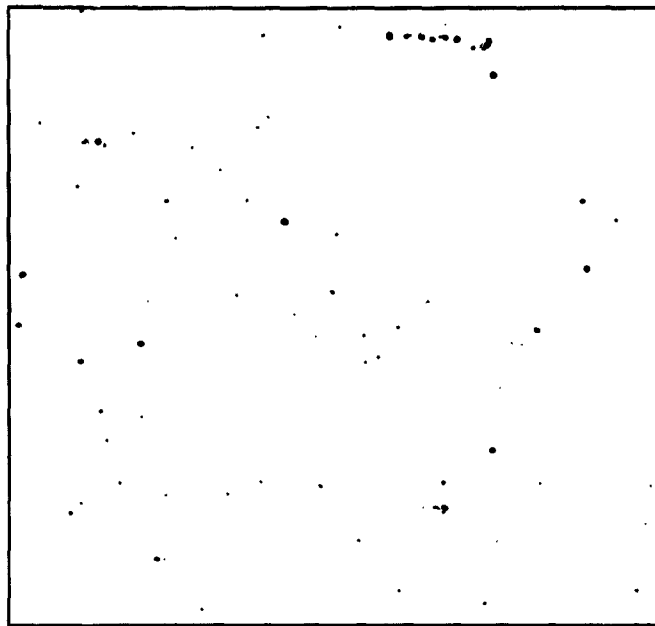
Figure 43

Typical Inclusion Content Observed in Crucible 218 (100X)
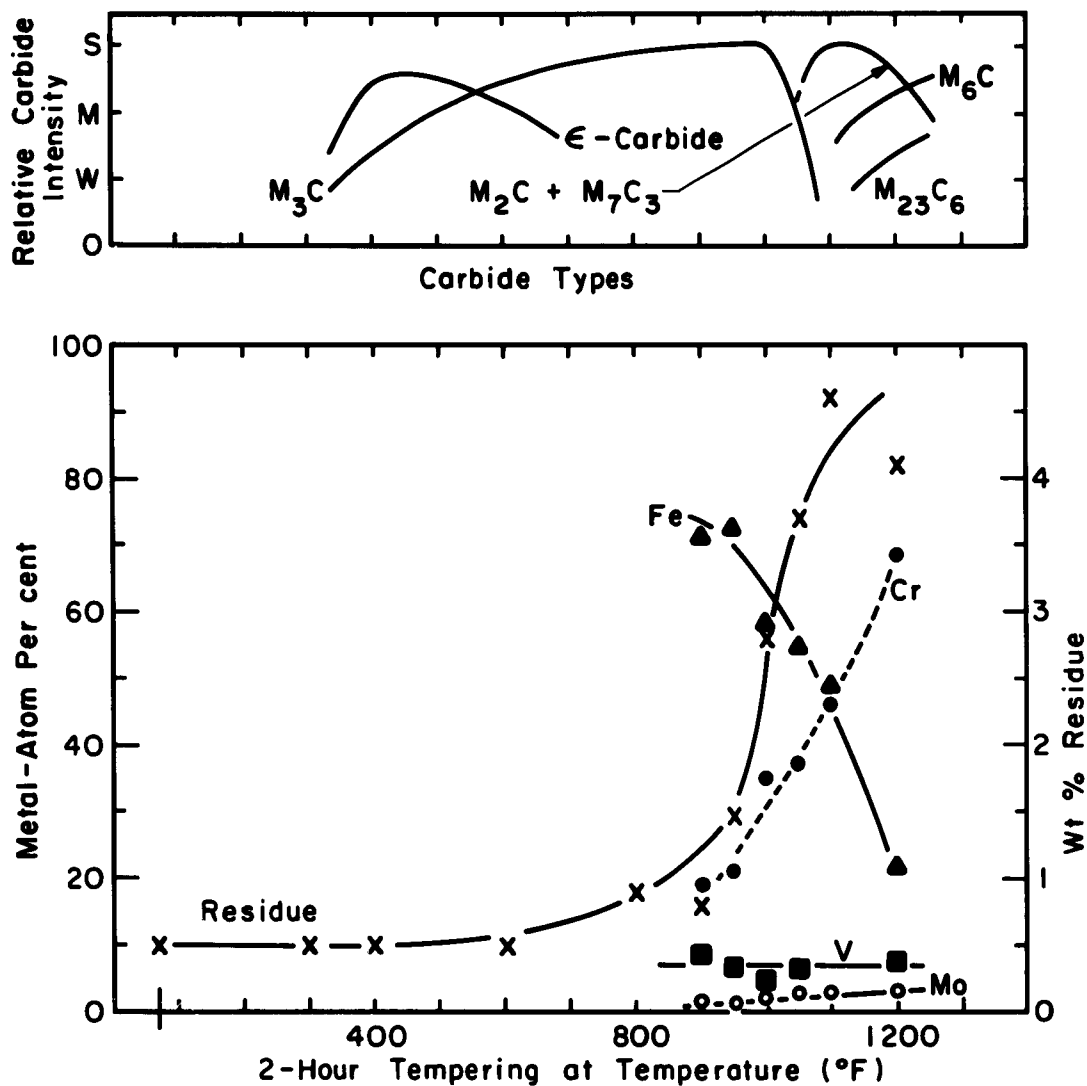
Figure 44

Carbide Analyses of Crucible 218 as a Function of Tempering
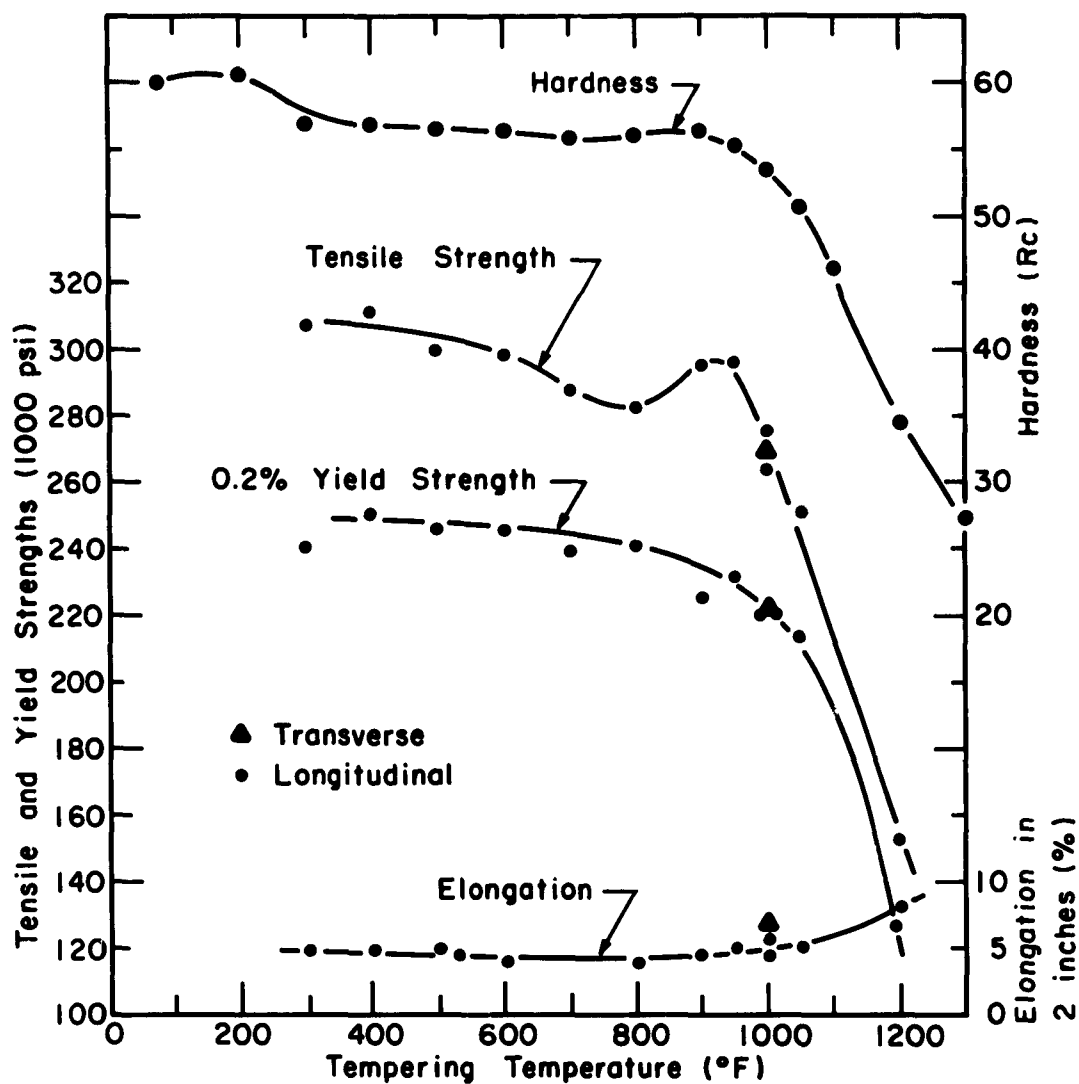
Figure 45

Effects of Tempering on Hardness and Tensile Properties of Crucible 218
Tempered at Indicated Temperature for 2 + 2 Hours

(a) Surface Replica (15,000X) (b) Extraction Replica (30,000X)
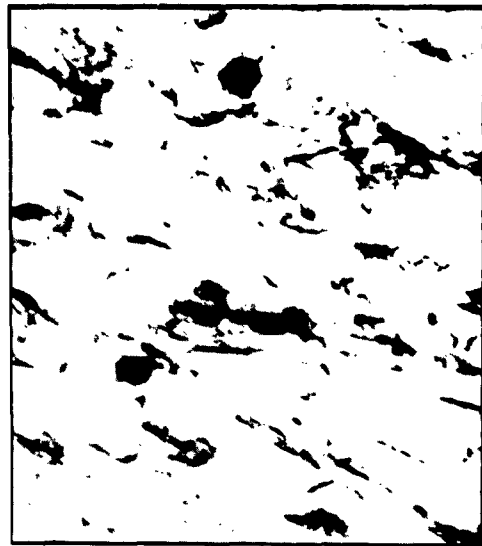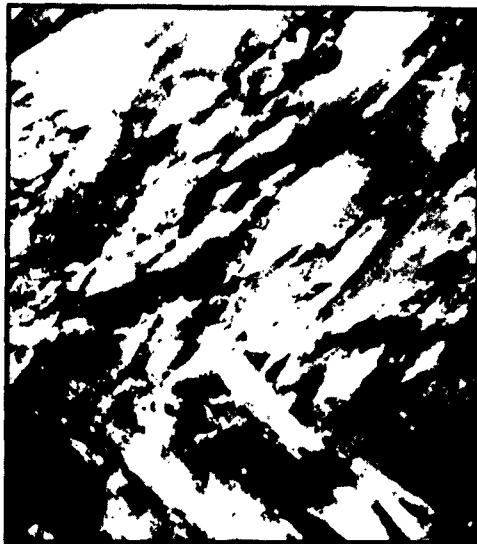
(c) Thin Section (30,000X) (d) Thin Section (60,000X)

Figure 46

Micrographs of Crucible 218 Oil-Quenched
from 1850 F and Refrigerated at -320 F
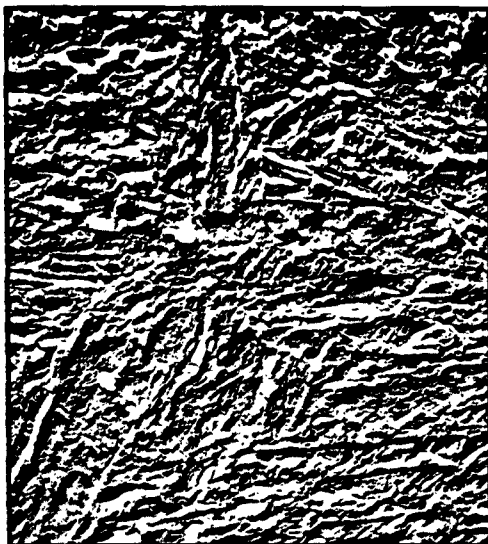
Vilella's Reagent

(a) Surface Replica (15,000X)   (b) Extraction Replica (30,000X)
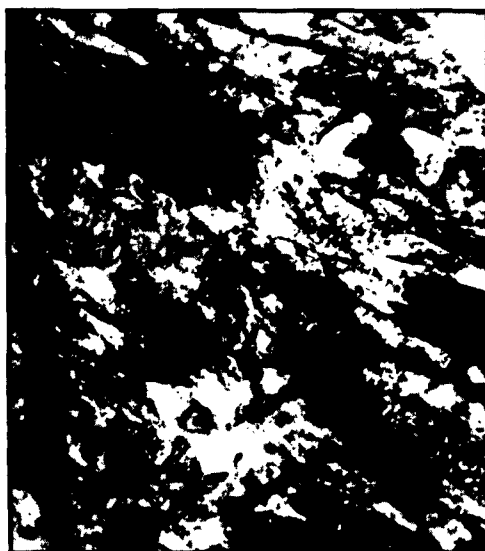
(c) Thin Section (30,000X)   (d) Thin Section (60,000X)

Figure 47

Micrographs of Crucible 218 Tempered at 400 F for 2 + 2 Hours

Vilella's Reagent

114

(a) Surface Replica (15,000X)   (b) Extraction Replica (30,000X)
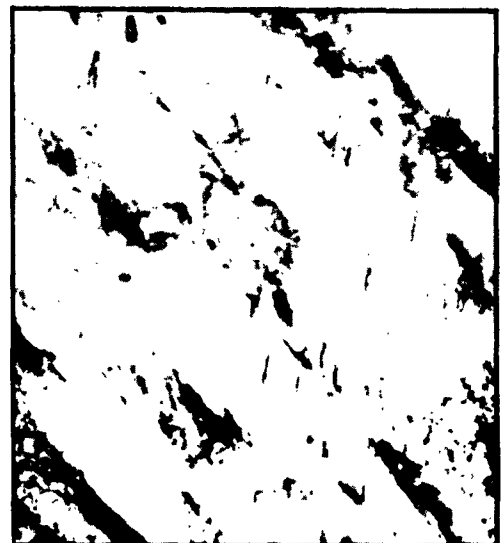
(c) Thin Section (30,000X)   (d) Thin Section (60,000X)

Figure 48

Micrographs of Crucible 218 Tempered at 500 F for 2 + 2 Hours

Vilella's Reagent
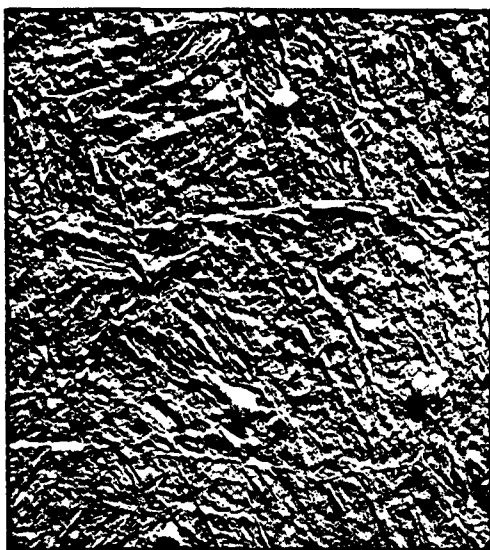
115

(a) Surface Replica (15,000X)   (b) Extraction Replica (30,000X)

(c) Thin Section (30,000X)   (d) Thin Section (60,000X)

Figure 49

Micrographs of Crucible 218 Tempered at 800 F for 2 + 2 Hours

Vilella's Reagent

116

(a) Surface Replica (15,000X)   (b) Extraction Replica (30,000X)

(c) Thin Section (30,000X)   (d) Thin Section (60,000X)

Figure 50

Micrographs of Crucible 218 Tempered at 900 F for 2 + 2 Hours

Vilella's Reagent
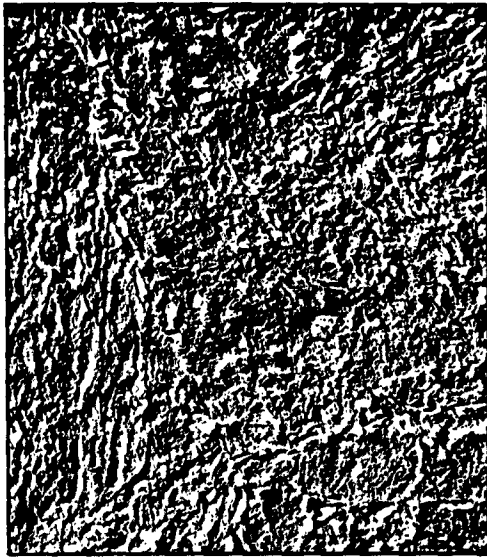
(a) Surface Replica (15,000X)   (b) Extraction Replica (30,000X)

(c) Thin Section (30,000X)   (d) Thin Section (60,000X)

Figure 51

Micrographs of Crucible 218 Tempered at 1000 F for 2 + 2 Hours

Vilella's Reagent

(a) Surface Replica (15,000X)   (b) Extraction Replica (30,000X)

(c) Thin Section (30,000X)   (d) Thin Section (60,000X)

Figure 52

Micrographs of Crucible 218 Tempered at 1100 F for 2 + 2 Hours

Vilella's Reagent

(a) Surface Replica (15,000X)   (b) Extraction Replica (30,000X)

(c) Thin Section (30,000X)   (d) Thin Section (60,000X)

Figure 53

Micrographs of Crucible 218 Tempered at 1200 F for 2 + 2 Hours

Vilella's Reagent
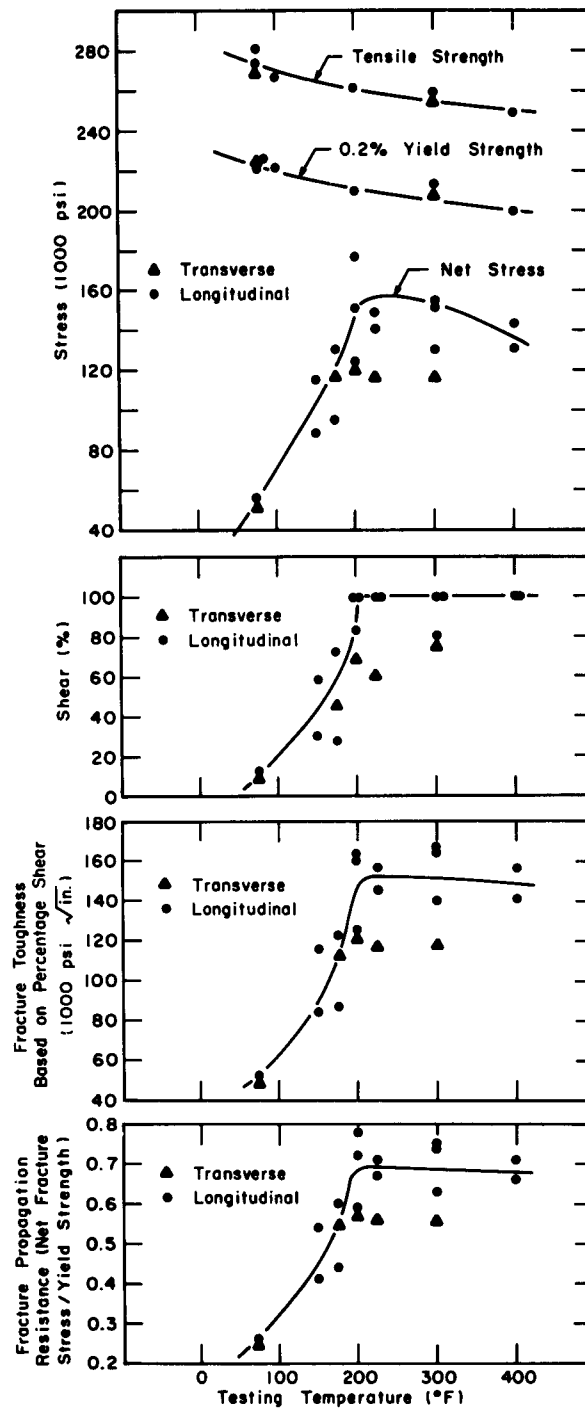
Figure 54

Properties of Air - Melted Crucible 218

0.067 - inch - thick specimens austenitized at 1850 F for 1/2 hr, oil quenched,
refrigerated at -320 F, and tempered at 1000 F for 2 + 2 hr.
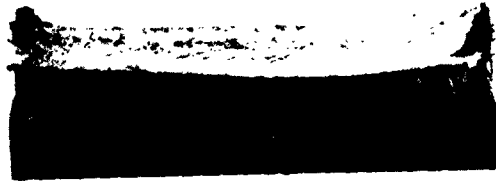
121

Longitudinal Specimen Tested at 70 F

Longitudinal Specimen Tested at 300 F

Transverse Specimen Tested at 70 F

Transverse Specimen Tested at 300 F

Figure 55

Fractured Surfaces of Smooth-Bar Tensile Specimens of Crucible 218
Quenched and Tempered at 1000 F for 2 + 2 Hours

Longitudinal Specimen Tested at 70 F

Longitudinal Specimen Tested at 300 F

Transverse Specimen Tested at 70 F

Transverse Specimen Tested at 300 F

Figure 56

Fractured Surfaces of Centrally Notched Samples of Crucible 218
Quenched and Tempered at 1000 F for 2 + 2 Hours

123
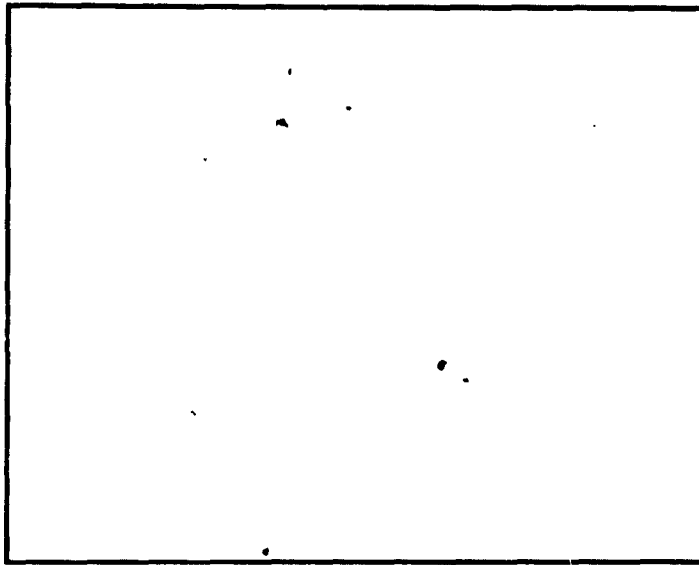
Figure 57

Typical Inclusion Content Observed in
Type 301 Stainless Steel (100X)

124
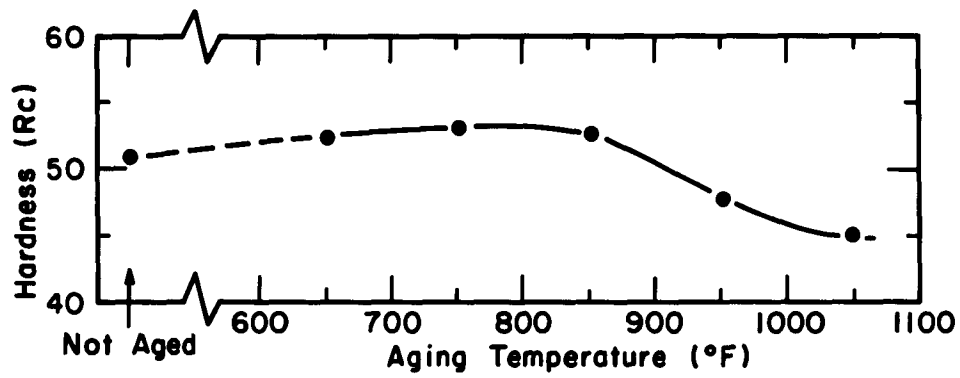
Figure 58

Hardness of Type 301 Stainless Steel Cold-Rolled 67% and
Aged at Indicated Temperature for 8 Hours

(a) Twin in Quenched Structure (25,000X)

(b) Slip Bands Crossing a Twin in Quenched Structure (25,000X)

(c) 93% Cold-Reduced (30,000X)

Figure 59

Transmission Electron Micrographs of Type 301 Stainless Steel

126
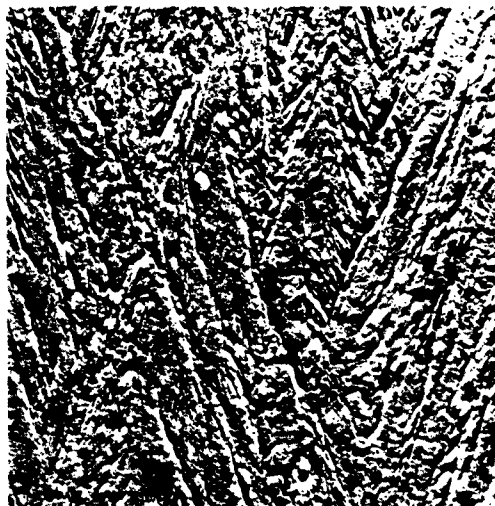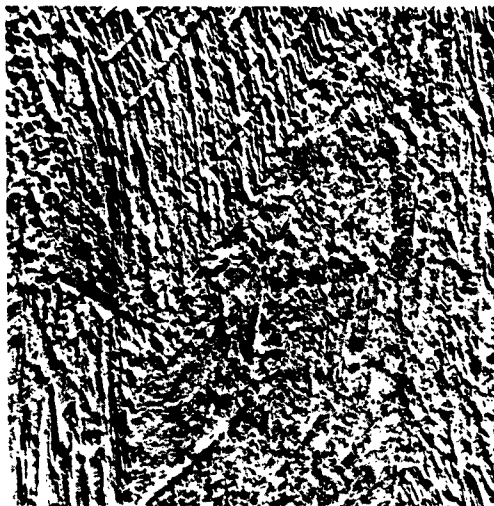
Transverse to Rolling Direction   Parallel to Rolling Direction
Surface Replica Micrographs (7,500X)

Transverse to Rolling Direction   Parallel to Rolling Direction
Light Micrographs (250X)

Figure 60

Edge View of Type 301 Stainless Steel Cold Rolled 67%
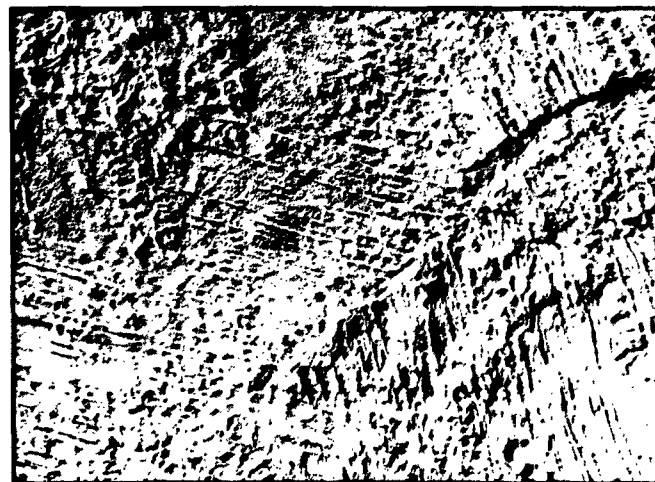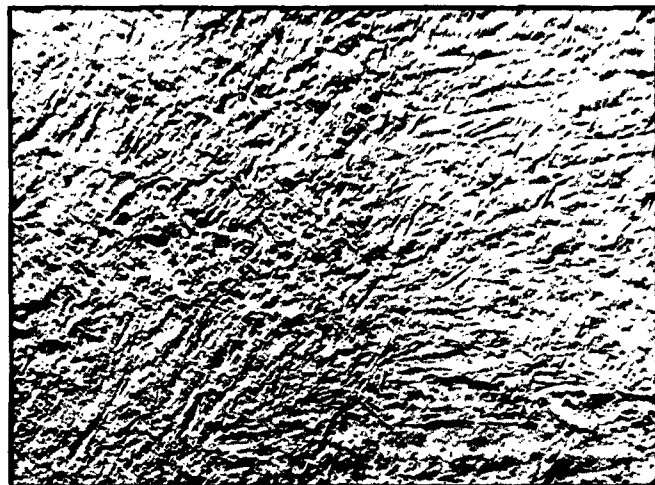
Cold Rolled Only　　　　　　Aged at 650 F　　　　　　Aged at 750 F

Figure 61

Surface Replica Micrographs of Type 301 Stainless Steel
Cold Rolled 67% and Aged at 650 and 750 F
for 8 Hours (7,500X)

128
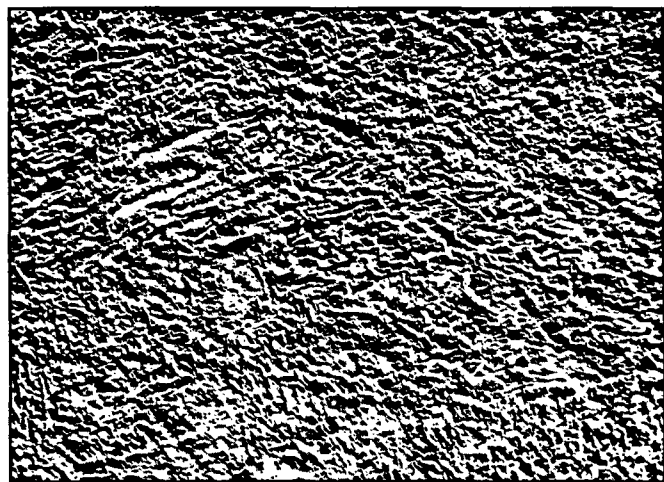
Aged at 850 F Aged at 950 F Aged at 1050 F

Figure 62

Surface Replica Micrographs of Type 301 Stainless Steel
Cold Rolled 67% and Aged at 850, 950 and
1050 F for 8 Hours (7,500X)

129
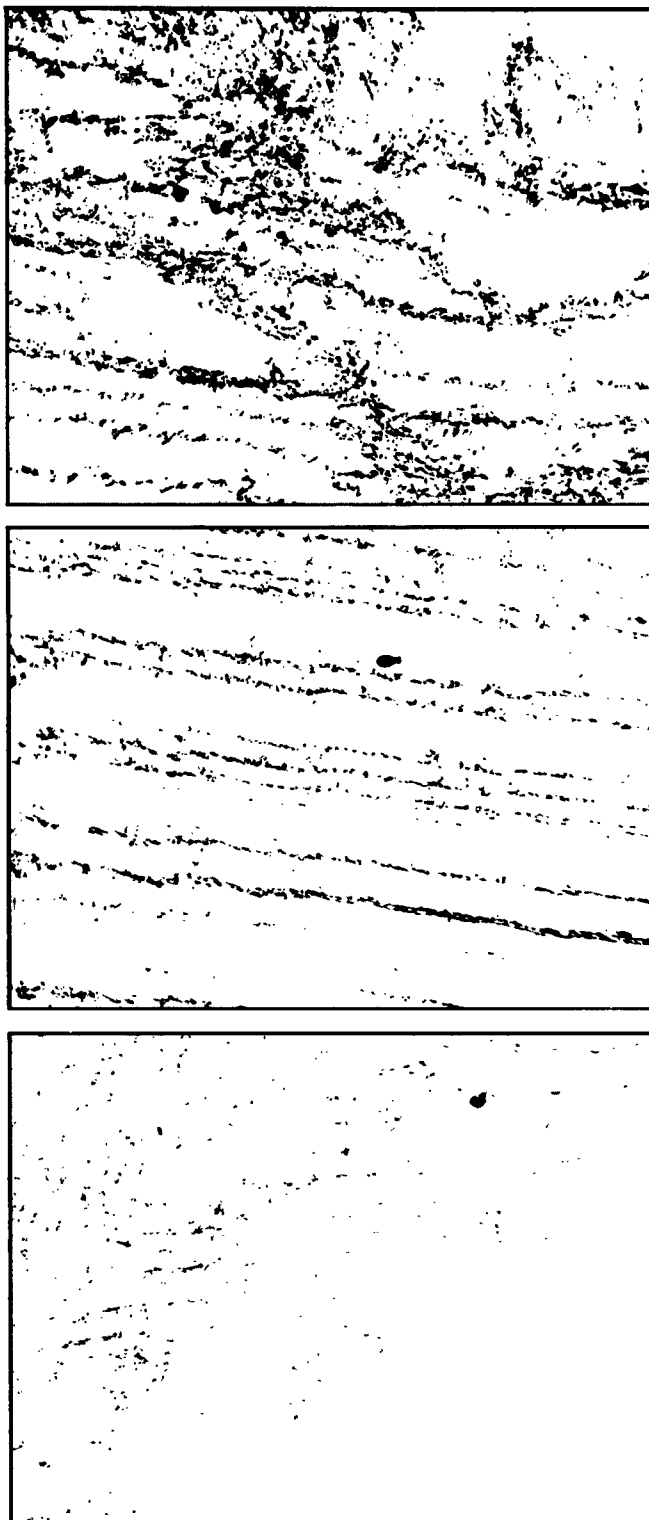
Aged at 850 F   Aged at 950 F   Aged at 1050 F

Figure 63

Extraction Replica Micrographs of Type 301 Stainless Steel
Cold Rolled 67% and Aged at 850,950 and
1050 F for 8 Hours (7,500X)
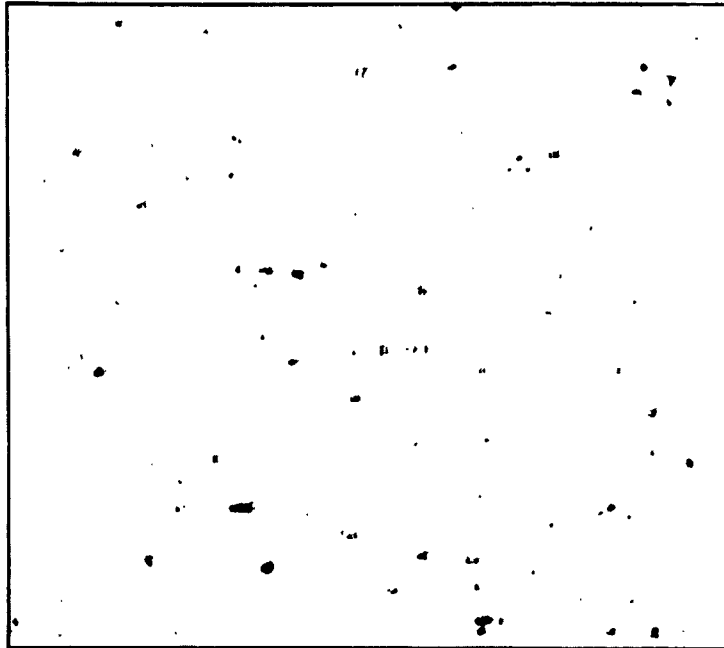
Figure 64

Polished Sample of PH15-7Mo Stainless Steel Showing
Many Titanium Carbonitrides (100X)
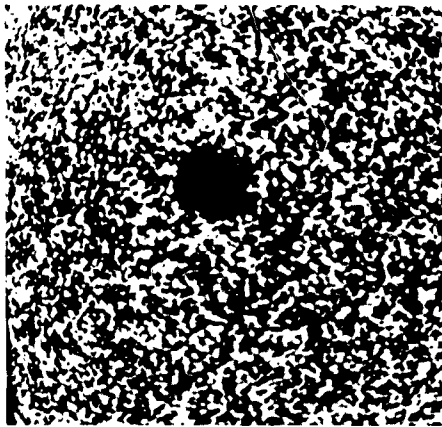
(a) 1000X
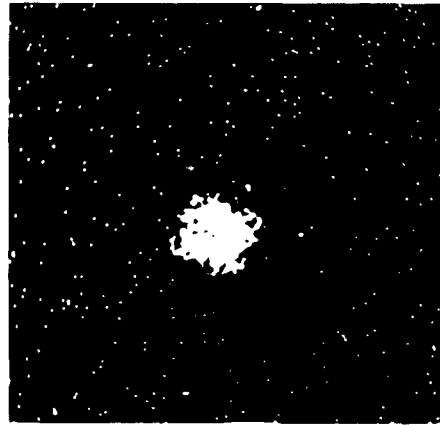
(c) 1000X
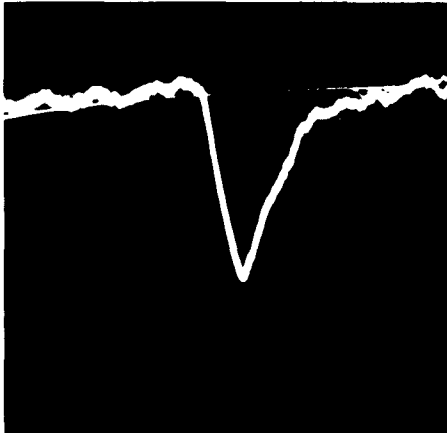
(b)
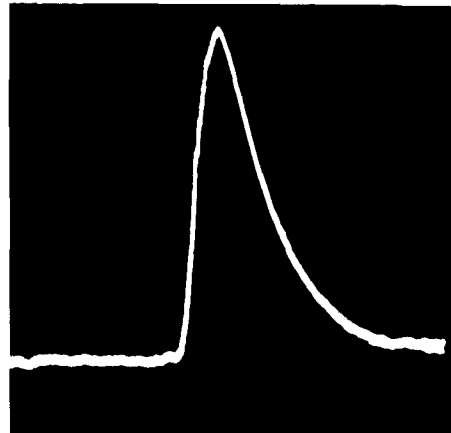
(d)

Figure 65

X-Ray Images (Top) and Recordings (Bottom) of X-Ray Intensity
Distribution across a Carbonitride in PH15-7Mo Stainless Steel

(a) and (b) show no iron
(c) and (d) show high titanium

100X

750X

Figure 66

Light Micrographs of PHI5-7Mo Stainless Steel

Sample austenitized , refrigerated, and aged
at 1150 F for 1 hr.

Ferrite is seen in the tempered structure ; a titanium
carbonitride particle is seen at the higher magnification.

133
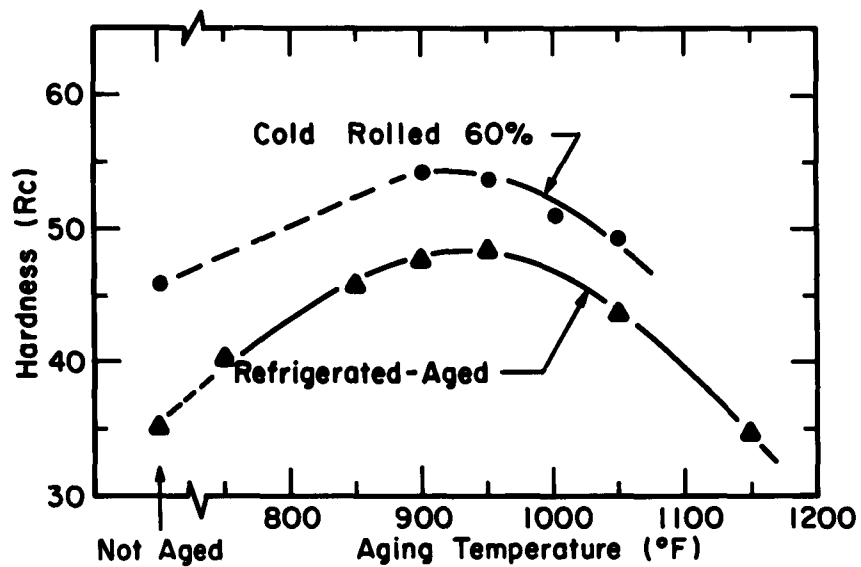
Figure 67

Hardness of PHI5-7Mo Stainless Steel after Aging at Indicated
Temperature for I Hour (Initially Given a 60% Reduction
or Refrigeration - Aging Treatment)

Thin Section (25,000X)

Extraction Replica (7,500X)
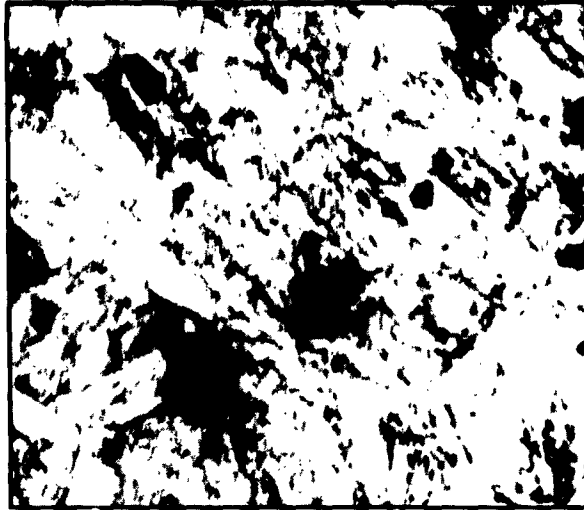
Surface Replica (7,500X)

Figure 68

Microstructures of PH15-7Mo Stainless Steel in the Refrigerated and Aged Condition

135

(a) Quenched (20,000X)

(b) Aged (20,000X)

(c) Aged (60,000X)

Figure 69

Transmission Electron Micrographs of B-120VCA Titanium Alloy
Quenched from 1400 F and Aged at 900 F for 72 Hours

136
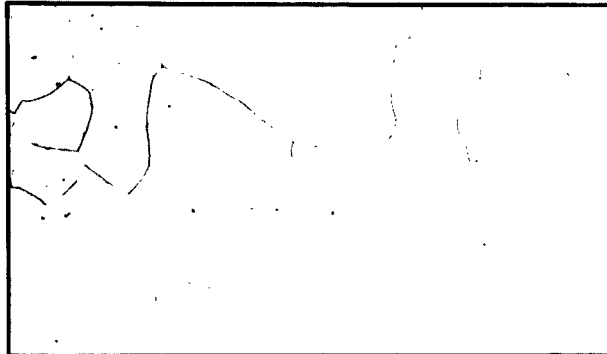
Figure 70

Ghost Boundaries in B-I2OVCA Titanium Alloy (250X)

These boundaries appear dotted and are much weaker than the grain boundaries.

Sample was quenched from 1300 F.

1. High-strength steels
2. Titanium
3. Crack propagation
I. AFSC Projects 7351, 7381; Tasks 735105, 738103
II. Contract AF 33(616)8156
III. Crucible Steel Co.of America Pittsburgh,Pa
IV. B.R.Banerjee J.J.Hauser

V. Aval fr OTS
VI. In ASTIA collection

Aeronautical Systems Division, Directorate of Materials and Processes, Metals and Ceramics Laboratory, Wright-Patterson Air Force Base, Ohio.
Report No. ASD-TDR-62-1034, Part I. RESEARCH AND APPLICATION ENGINEERING TO DETERMINE THE EFFECT OF PROCESSING VARIABLES ON CRACK PROPAGATION OF HIGH-STRENGTH STEELS AND TITANIUM. Interim report, April 1963. 137pp. incl. illus., tables 56 refs. Unclassified Report

(over)

This report describes in detail the fine-structural characterizing of several high-strength steels [AISI 4340, Type H-11 (Crucible 218), Type 422 stainless, work-hardened Type 301 stainless, PH15-7Mo semiaustenitic stainless, and B-120VCA beta titanium alloy] and gives the relationship of these structures to smooth and notch strength properties. The fine structures of these materials were characterized and correlated with strength and fracture properties to an extent never before achieved.